

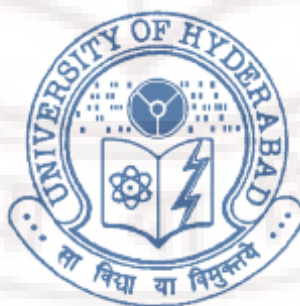
# **Ion Beam Modification of GaN based Semiconductor Heterostructures**

Thesis submitted for the degree of

**Doctor of Philosophy**

By

**N SATHISH**



**School of Physics  
University of Hyderabad  
Hyderabad – 500 046 India**

**June 2009**

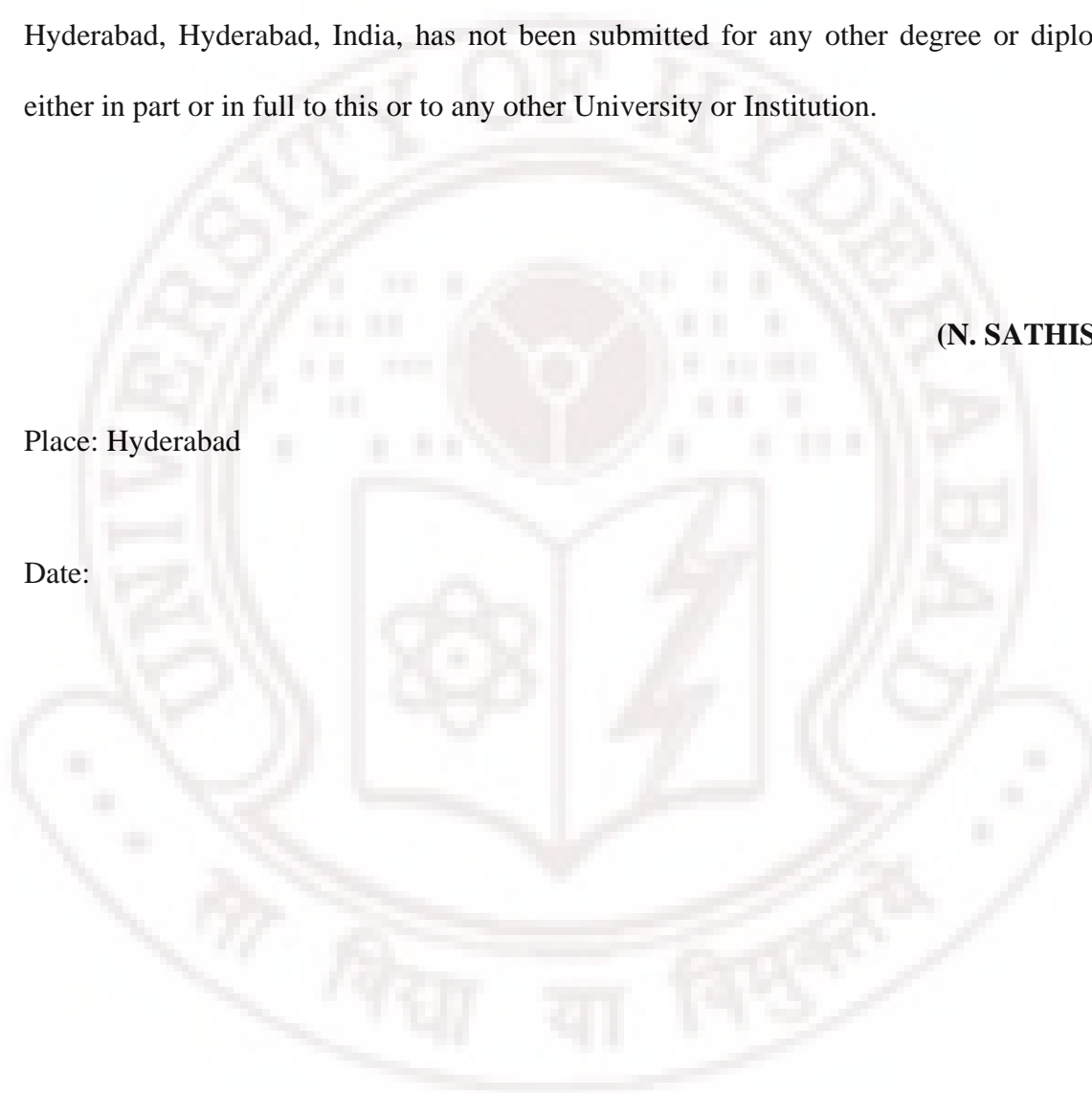
## DECLARATION

I hereby declare that the work embodied in this thesis entitled “**Ion beam modification of GaN based Semiconductor Heterostructures**” carried out by me, under the supervision of **Prof. Anand P Pathak**, School of Physics, University of Hyderabad, Hyderabad, India, has not been submitted for any other degree or diploma either in part or in full to this or to any other University or Institution.

(N. SATHISH)

Place: Hyderabad

Date:



# CERTIFICATE

This is to certify that the work described in this dissertation entitled “**Ton beam modification of GaN based Semiconductor Heterostructures**” has been carried out by **Mr. N. SATHISH** under my direct supervision for the full period prescribed under PhD. Ordinances of the University and the same has not been submitted for any other degree or diploma to this or any other University of Institution.

(Dean, School of Physics)

(Prof. Anand P Pathak)

(Thesis Supervisor)

Place: Hyderabad

Date:

## ACKNOWLEDGEMENTS

During this work I have collaborated with many people, for whom I have great regards. It has been great pleasure to get a chance to work with many renowned researchers and I sincerely thank all of them. I would like to thank all those who have, directly or indirectly, helped or encouraged or motivated me in successful completion of this thesis.

I am deeply indebted to Prof. Anand P Pathak, for his esteemed guidance though out my research. His wide knowledge and logical way of thinking have been of great value for me. His understanding, encouraging and personal guidance have provided a good basis for the present thesis. The way he inspired, advised and helped for both academic and personal life is unforgettable. He showed me different ways to approach a research problem and the need to be persistent to accomplish any goal. I feel I am very lucky for getting him as my PhD supervisor who had taught me several crucial concepts and trained me in getting expertise. Once again I thank him for establishing collaboration with several institutes and organizations in India and abroad and for providing all facilities and help in completing this work. Finally I thank his family members (madam and Kittu) for providing homely atmosphere during our meetings on several occasions. Moreover he is much more than just a supervisor to me. More appropriate word would be “Academic Father”.

I would like to thank Dr. Devesh K Avasthi, IUAC for help in learning the accelerator based techniques. He has helped in planning and executing several experiments at IUAC. His constant encouragement and experimental support has been vital in completing the work reported in this thesis. During my stay in IUAC, he made me to learn basics which developed my skills. I sincerely thank him for helping me in learning many experimental techniques. I am also thankful to Dr. Amit Roy, Director, Dr. S K Datta, Dr. D Kanjilal, Dr. A Tripathi, Dr. Ravikumar, Dr F Singh for their help and support during my visits to IUAC. I would like to express special thanks to Mr. S A Khan, whose support during all my experiments gave me confidence and success. I acknowledge AUC committee for providing beam time. I am also thankful to the pelletron group and other supporting labs in IUAC for providing necessary facilities during the experiments. I remember all IUAC

friends for providing lively environment during my stay there particularly, Yash, Manav, Pankaj, Sugam, Vikas, Hardev, Surendar, Arjunan and other friends.

I take this opportunity to thank Prof. Brij M Arora, TIFR and Dr R Muralidaran, SSPL. Who taught me both experiments and theory. During my visits to TIFR and SSPL, they have been very kind in spending their valuable time with me to discuss the experimental results. My discussions with them have really amplified my understanding of the subject. It has been great pleasure to work at IGCAR, Kalpakkam with Dr. K G M Nair, Dr P K Panigrahi & Dr. B Sundaravel. RBS/Channeling experiments and discussions carried out at IGCAR nourished my ideas. I wish to work in collaboration with them in future also. I also thank other colleagues at IGCAR, namely Dr. S Dhara, Mr. Magudapathy, Mr. David, Dr. Amirthapandian, Santhana Raman and Saravanan for their help during my visits to IGCAR.

I take this opportunity to express my gratitude to Prof. P Mazzoldi, Prof G Mattei, Dr E Trave and Dr M Bazan, at the University of Padova. I had a chance to work with them for about two weeks. Their sincerity and concern towards the work has been splendid. The stimulating discussions and arguments with them gave me a lively atmosphere to breath physics. Their collaboration on Er implantation has been very important, without which this part of work would not have been realized in this thesis. I am grateful to Dimitris Emfietzoglou, Greece for guidance and help on the stopping power calculations. I express my sincere thanks to Prof. D Ila and Dr. C Muntele, Alabama, USA, Prof V N Kulkarni, IIT Kanpur and Prof Mark Breese for some of the RBS/Channeling measurements. I thank, Prof. A Turos, Dr J Gaca and Dr M Wojcik for collaborations on III-Nitride works. During their visit to UH, discussions on channeling & HRXRD was very much useful in the analysis of my experimental data. It was great pleasure to work with Prof Lech Nowicki during his visit to Hyderabad. I thank him for collaborations and for providing the McChasy code to incorporate the dislocations in the code.

I express my sincere thanks to former Dean Prof. V S S Sastry, particularly for making me realize the way to work, think and approach research problems. His critical comments developed my abilities. I also thank present Dean, Prof. V Srivastava, for his support and providing the necessary facilities. I am also thankful to Dr. M G Krishna for his help and discussions on AFM & Optical measurements. Also I would like to thank doctoral

committee member Prof G Rajaram for his valuable suggestions on my work. I would like to thank Prof S R Shenoy, for his wonderful classes on Advanced Statistical Mechanics, where I learnt the basics of Statistical mechanics. After attending his classes, I also developed motivation to become good teacher like him. I would also like to thank other faculty members of school of physics.

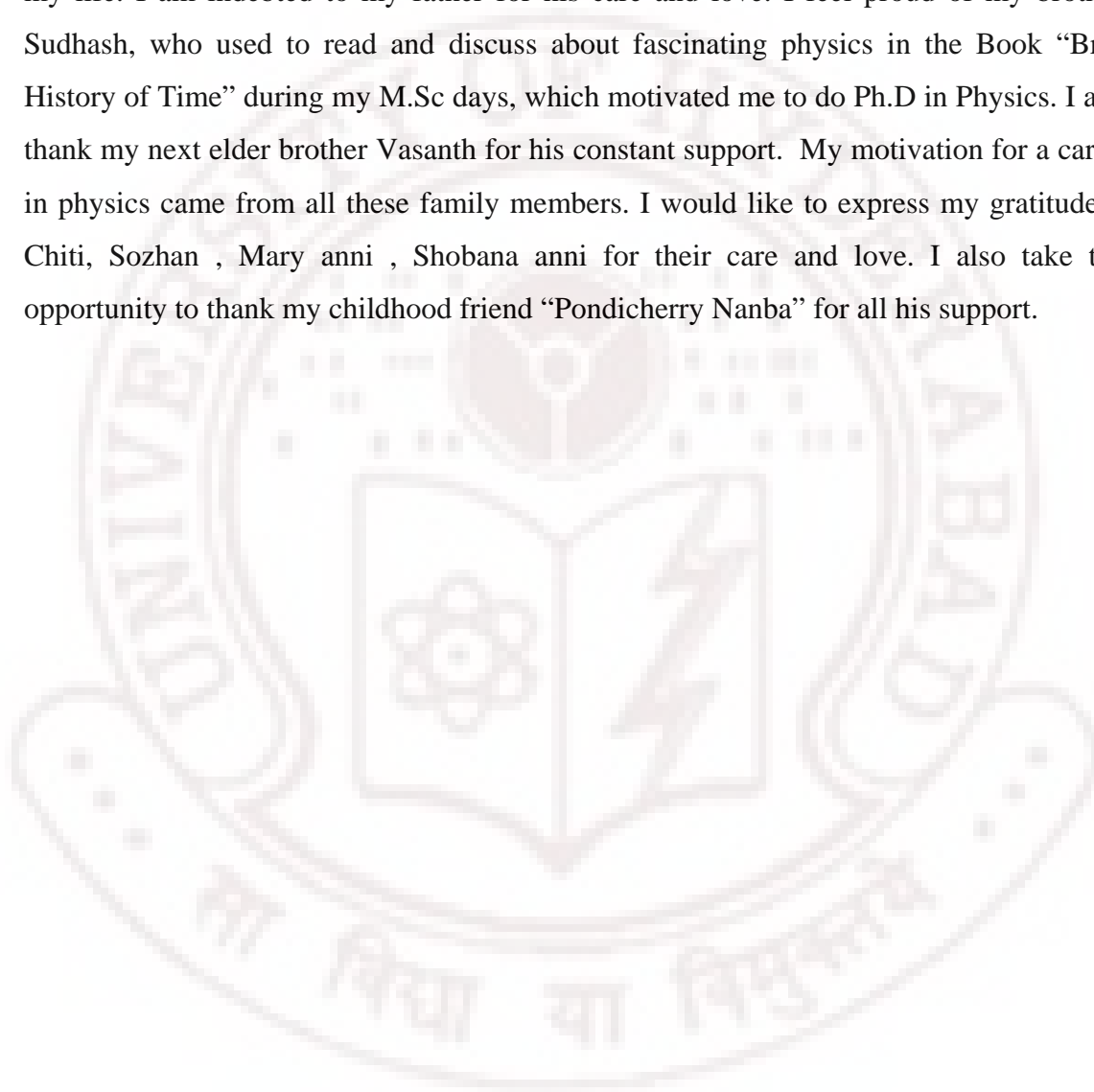
I am very much thankful to Dr G Saisaravanan, GAETEC, for helping in RTA experiments and spending his time with me on many occasions. I also acknowledge discussions on AFM with Mr Mahadev, which stimulated many ideas for my future works. I thank my senior Dr. A M Siddiqui, with whom I worked a lot in a lively atmosphere, during early stages of my research. I am thankful to my friend Damu (Dr S Dhamodaran) and his family members for their love since our B.Sc. days. I thank my colleagues Ms. Juby George, Mr. N Srinivasa Rao, Mr G Devaraju and Mr V Sai Kiran for their kind support and collaboration during visits to other institutes for experimental work.

Damu and Bharathi (Dr Bharati Mohan), the friends from B.Sc and M.Sc days to whom I owe a lot for their constant support and help, ever since I came to this university, have been source of inspiration. Saravanan, has been equally helpful, supportive and understanding all along my stay here and I do not have enough words to thank him. Many other friends like Harshan, Mani and Ajith have also made my stay here pleasant and provided friendly atmosphere of which I carry the memorable moments with Rizwan and Bari. I would also like to thank Brahma, Raji, Sai preethi, Jaysree, Gnanavel, Lakshmi Narayana, Vijayan, Abilash, Joji and Shinto for good friendly environment in the school. I thank all the scholars in the school of physics for helping me directly or indirectly. The organization of IBA2007 has been possible with help of all these friends and has also helped making many more friends. Their kind help and encouragement in critical situations was indispensable to manage such a big international event. This has been a great experience of academic life for me.

Also I would like to thank Grace, Lily, Daniel, Tiger, Theurei, RK and Vitso with whom I had nice time. Also I should thank the whole DSP and Uncle Kill Me Quick and Tamil group and O-wing mates for providing lively atmosphere during my stay in HCU.

I thank Mr. Abraham and other office staff members of the school for their timely help on every occasion. I would like to express my sincere thanks to DRDO, SSPL and UGC for providing financial support. The financial support from the International Centre for Theoretical Physics, Trieste, Italy for my visit is gratefully acknowledged.

My deepest gratitude goes to my family for their unflagging love and support throughout my life. I am indebted to my father for his care and love. I feel proud of my brother, Sudhash, who used to read and discuss about fascinating physics in the Book “Brief History of Time” during my M.Sc days, which motivated me to do Ph.D in Physics. I also thank my next elder brother Vasanth for his constant support. My motivation for a career in physics came from all these family members. I would like to express my gratitude to Chiti, Sozhan , Mary anni , Shobana anni for their care and love. I also take this opportunity to thank my childhood friend “Pondicherry Nanba” for all his support.





**To my Family & Memories of my Mother**



# TABLE OF CONTENTS

<b>Declaration</b>	i
<b>Certificate</b>	ii
<b>Acknowledgements</b>	iii

## Chapter I: Introduction

1.1	Ion Solid Interaction	2
1.1.1	Nuclear energy loss	3
1.1.1.1	Simulation of the lattice damage by low energy ions	5
1.1.2	Electronic energy loss	6
1.1.2.1	Bohr's stopping formula	7
1.1.2.2	Bethe's stopping formula	9
1.1.2.3	Bethe-Bolch stopping formula	12
1.1.2.4	Barkas Correction	17
1.1.2.5	Bloch correction	18
1.2	Materials of Interest	18
1.2.1	Works done on ion beam modification of III-Nitrides	24
1.3	Probing Techniques and Descriptions	27
1.3.1	Photoluminescence	28
1.3.2	Rutherford Backscattering Spectrometry /Channeling (RBS/C)	28
1.3.3	High Resolution X-Ray Diffraction (HRXRD)	29
1.3.4	Atomic Force Microscopy (AFM)	29

## Chapter II: Experimental Techniques

2.1	Samples Details	32
2.2	Irradiation and Implantation	33
2.2.1	IUAC accelerator facility	34
2.2.2	Er Implantation and annealing	36
2.3	Characterization techniques	37
2.3.1	RBS/Channeling	37

2.3.2 HRXRD	46
2.3.3 Optical characterization	48
2.3.4 AFM	50
 <b>Chapter III: Effects SHI on Bulk Epitaxial GaN layers</b>	
3.1. RBS/ Channelling studies	55
3.2. High Resolution X-Ray Diffraction	58
3.3. Atomic Force Microscopy	62
3.4. Optical Studies	64
3.5. Conclusions	66
 <b>Chapter IV: Effects of SHI on AlGaIn/GaN Heterostructures</b>	
4.1. RBS/Channelling	71
4.2. HRXRD	77
4.3. AFM	81
4.4. Conclusion	82
 <b>Chapter V: Er implantation into GaN layers</b>	
5.1 PL studies	
5.1.1 Optical properties of the as-implanted ErGaIn samples	89
5.1.2 Annealing effects on the ErGaIn PL properties	90
5.1.3 Mechanism for the excitation of the PL emission process	93
5.1.4 Dynamics of the PL emission process	95
5.1.5 Estimation of the effective Er excitation cross section	98
5.1.6 Optical activation of the Er ions	100
5.2 RBS/Channelling Lattice site location studies	
5.2.1 ErGaIn1	102
5.2.2 ErGaIn5	103
5.2.3 ErGaIn10	105
5.3 Conclusions	107

## **Chapter VI: Dielectric function theory of stopping power of GaAs: An optical data model calculation**

6.1 Dielectric theory of stopping power	111
6.2. The Method	113
6.3. Results and discussions	116
6.4. Summary and conclusions	122

## **Chapter VII: Conclusions and outlook**

7.1 Effects of SHI on GaN and AlGaIn/GaN heterostructures	124
7.2 Optical properties and Lattice site location of Er implanted GaN	126
7.3 Stopping power of GaAs	127
7.4 Future prospects	128

## **CV with List of Publications**

# CHAPTER – I

## Introduction

Ion beams have proven to be versatile tool for processing materials and synthesizing unique structures of interest for a wide variety of applications. Introduction of ion species into the solids can be used to alter and tailor electrical and optical properties of materials. Defect generation during ion-solid interactions adds a further dimension to this processing capability enabling kinetic mechanisms to synthesize metastable phases normally, which are not usually achievable under equilibrium thermodynamic conditions. Techniques employing ion beams span a large range of energy and dose and can be combined with various material preparation techniques permitting additional processing degrees of freedom for producing new materials.

One of the applications of ion beams is to modify the materials properties so as to enhance their electronic and optical performance and also to synthesize new structures and novel phases to engineer the material properties. Low energy ions are used for ion implantation and defect engineering in various semiconductors by nuclear energy loss. On the other hand, Swift Heavy Ion (SHI) beam induced modification of material properties is achieved via electronic energy loss. When energetic ion interacts with materials, it receives high energy density in very short times ( $\sim 10^{-17}$  to  $10^{-15}$  s) within a very tiny volume ( $\sim 10^{-17}$  to  $10^{-16}$  cm<sup>3</sup>). This energy density is same as exploding a hydrogen bomb. This energy deposition is commonly described as stopping power  $dE/dx$  of the target materials, which gives the energy transferred per unit length of the target. This stopping power has been split into two parts based on the mechanism of energy deposition. These are “nuclear” energy transfers, dominated by atomic collisions with target atoms and “electronic” energy transfer, dominated by excitation and ionization of target electrons. Total stopping power is sum of both these components. The nuclear energy loss results in knocking of the target atoms from the lattice sites, when the transferred energy exceeds the displacement (or binding) energy of the target atom. This leads to the formation of structural defects.

## 1.1 Ion solid interactions

When a swift charged particle enters a material, it interacts with the electrons and nuclei in the medium and begins to lose energy as it penetrates into the medium. The interaction can be generally thought of as collisions between the charged particle and either the individual atomic electrons or the atom as a whole. Depending on the initial energy of the incident ion, one or more of the following mechanisms can be operative:

- (i) Nuclear energy loss
- (ii) Electronic energy loss
- (iii) Photon emission and
- (iv) Nuclear reactions

Among these, electronic energy loss is the most prominent one in slowing down the high velocity charged particles. However, energy loss to nuclear collisions is most important at low velocities in particular for high mass ions (Fig.1.1 for comparison). While photon emission processes (bremsstrahlung, Cerenkov radiation) dominate at relativistic velocities, nuclear reactions take over when the incident energies cross the Coulomb barrier and strong nuclear interactions become operative. The interest of present thesis is limited to energies where only the nuclear and electronic energy losses of the incident ions are dominant.

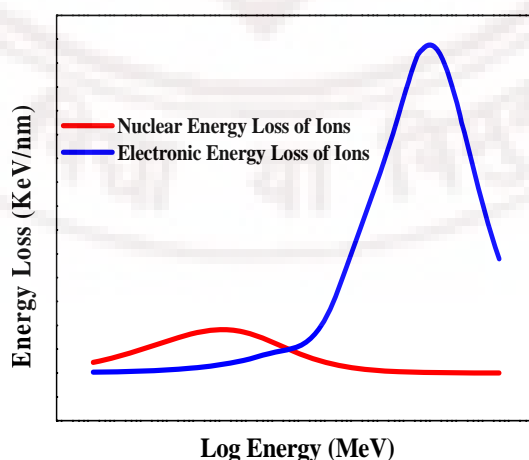


**Fig.1.1.** Comparison of typical nuclear and electronic energy loss

### 1.1.1 Nuclear energy loss

Nuclear energy loss is due to the elastic collisions between projectile and target nuclei. It increases with higher projectile mass, and it is dominant mechanism at low energies and successfully explained by the binary collision model. Fig 1.2 is a schematic representation of the binary collision model. In binary collision model, projectile with mass  $M_1$ , atomic number  $Z_1$ , energy  $E_0$  and momentum  $p_0$  interacts elastically with the target atom of mass  $M_2$  and atomic number  $Z_2$  at rest.

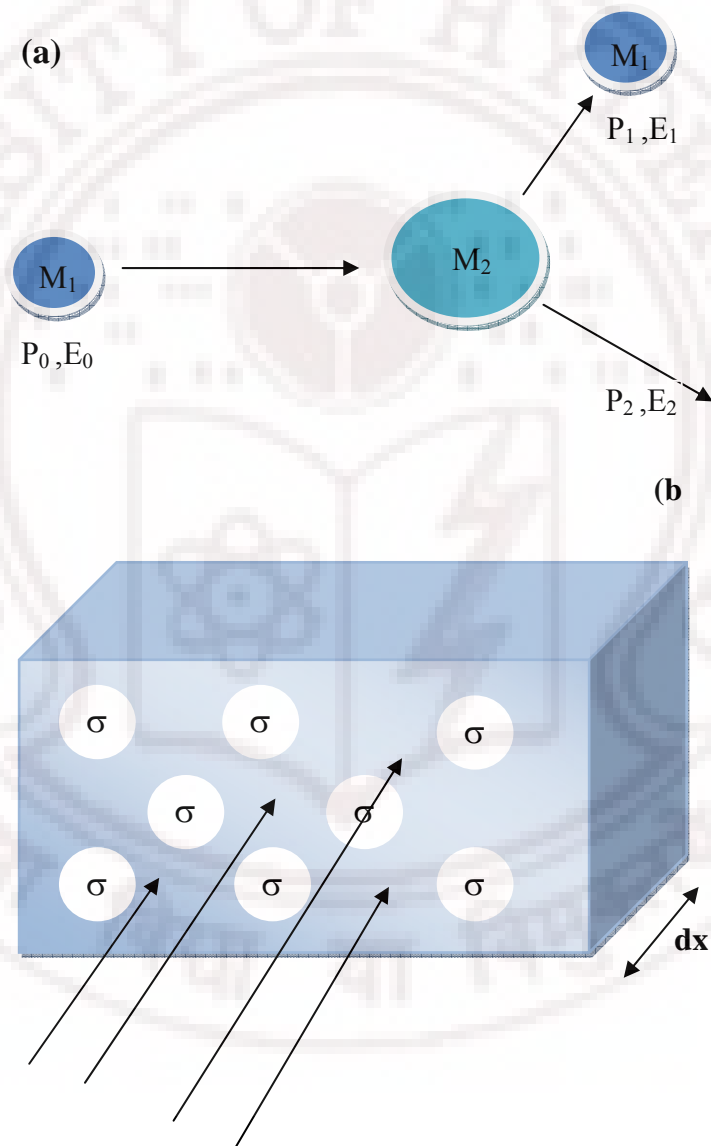


**Fig 1.2.**(a) Sketch of a binary collision picture (b) Interaction between incoming ions and the scattering centers  $\sigma$ .

The interaction potential between the projectile and target atom is given by the screened coulomb potential.

$$V(r) = \frac{Z_1 Z_2 e^2}{r} \chi(r) \quad (1.1)$$

where  $\chi(r)$  is a screening function and should satisfy the basic condition,

$$\chi(r) = \begin{cases} 0 & r \rightarrow \infty \\ 1 & r \rightarrow 0 \end{cases} \quad (1.2)$$

The energy transferred during the interaction is given as

$$T = 4 \frac{M_1 M_2}{(M_1 + M_2)^2} E_0 \sin^2 \frac{\theta}{2} = \zeta E_0 \sin^2 \frac{\theta}{2} \quad (1.3)$$

where  $\theta$  is the scattering angle. The nuclear stopping power is written as

$$S_n(E) = \int_{T_{min}}^{T_{max}} T \frac{d\sigma(E)}{dT} dT \quad (1.4)$$

$\sigma(E)$  is the cross section for nuclear interactions,  $T_{min}=E_d$  is the displacement energy and  $T_{max} = \zeta E$ . There are many approximations available to calculate the integral, but the most commonly used one is Zigler, Biersack and Littmark (ZBL) [1] model

$$\frac{d\sigma(E)}{dT} = C \frac{f(t^{1/2})}{t^{3/2}} \quad (1.5)$$

$$f\left(t^{\frac{1}{2}}\right) = \frac{\lambda t^{1/(2-m)}}{[1+(2 \lambda t^{1-m})^q]^{1/q}} \quad (1.6)$$

where  $t=KE^2T$ ,  $\lambda=5.012$ ,  $m=0.203$ ,  $q=0.413$  and  $K$  is parameter depending on the masses and atomic numbers of the colliding atoms.

Ion loses its energy by multiple collisions with the target atoms. A useful and important quantity in this process is range of the projectile i.e. how deep the projectile with energy  $E_0$  will penetrate into the target.

$$R = \int_{E_0}^0 \left(\frac{dE}{dx}\right)^{-1} dE \quad (1.7)$$

The statistical distribution of the implanted ions can be described by a Gaussian centered at the perpendicular projected range  $R_p$  and FWHM of  $\Delta R_p$  is called straggling. The range increases with decreasing projectile ion mass or increasing ion energy.

During the slowing down process ion undergoes multiple collisions and displaces lattice atoms. The first target atom displaced by ion is called Primary Knock-on Atom (PKA). This PKA initiates the collision cascade by successive collisions with subsequent target atoms and many more target atoms are displaced and form complex defects. The process of defects creations are governed by the different parameters like projectile atomic number  $Z_1$ , incoming energy  $E$ , energy of the projectile after collision  $E_1$ , and target atomic number  $Z_2$ , displacement energy  $E_d$ , binding energy  $E_b$ , the energy of the target atoms after collision  $E_2$ , [2].

- (i) If  $E_2 > E_d$ , then displacement occurs.
- (ii) A vacancy occurs if  $E_2 < E_d$ .
- (iii) If  $E_1 > E_d$  and  $E_2 < E_d$  the target atom will not have enough energy and comes back to original site by realizing thermal phonon results in heating if the target lattice.
- (iv) If  $E_1 < E_d$  and  $E_2 > E_d$  and  $Z_1 = Z_2$ , then the incoming atom will cause the replacement collision and releases the energy  $E_1$  as phonons.
- (v) If  $E_1 < E_d$  and  $E_2 > E_d$  and  $Z_1 \neq Z_2$ , then  $Z_1$  will be at interstitial.
- (vi) If  $E_1 < E_d$  and  $E_2 < E_d$ , then  $Z_1$  will be at interstitial and releases the energy  $E_1 + E_2$  as phonons.

#### 1.1.1.1 Simulation of the lattice damage by low energy ions

Stopping and Ranges of Ions in Matter (SRIM) [1,3] is the commonly used code for simulating the kinetics of the ion implantation. It uses the Monte Carlo calculations to calculate the trajectory of ions in the target and makes the detailed calculations of the energy transferred to each and every target atoms during its passage. The quantities like projected range, ion damage and target ionization are calculated by averaging over large number of projectile ions. The code also calculates, for compound structures and gives the final 3D distribution of the ions, target damage, sputtering, ionization and phonon production. Also the target atoms collision cascades are simulated in detail.



### 1.1.2 Electronic energy loss

Energy loss calculations for swift point charges were first carried out by Bohr [4] during the period 1913-15. He treated the projectile as fast moving classical particles. Bethe [5] used incident plane wave and quantum perturbation theory instead of classical treatment and Bloch [6] introduced the higher order corrections to it. But both the theories failed at the Bragg peak. In 1940's new developments took place and particle stopping was treated by introducing the polarization phenomena using Maxwell's equations [7]. Later, Lindhard [8] demonstrated that stopping power can be described in terms of wave number and frequency dependent dielectric function. In a recent monograph, P Sigmund has revisited the developments of the stopping theory of solids extensively [9]. On the other hand, the SRIM code developed by Ziegler has been used to estimate the stopping powers of compound materials like GaAs. He used the known experimental data to fit the unknown materials by extrapolation. He also used the Bethe-Bloch formula with higher order corrections where no experimental data is available. This program works well for single atomic targets. Recently Sigmund and Schinner [10] have used the non-perturbative methods based on binary collision theory with Barkas and Bloch corrections. Schiweitez and Grande developed the code CasP [11], which calculates the impact parameter dependent scattering cross sections. Using CasP code one can calculate the stopping power for many compound targets. It has been observed that in metallic and compound semiconductor targets, the collective excitations take place and this effect can be described very well with the dielectric function formalism i.e. many body treatment given by Lindhard and later modified by Ritchie [12]. Even though Bethe theory predicted the energy loss of light ions very well but it requires experimental input for heavy ion stopping. Also measuring this for all the compound materials is not possible. The optical data model of Ritchie and Howie [13] provides a good tool for calculating the stopping power more accurately within the dielectric function theory. Here one takes the optical data (zero momentum dielectric function) and derives the optical oscillator strength then extends it to the momentum space by using Drude's extension scheme. This is then used to calculate the stopping power. Using optical data, reasonable accuracy in predicting the Inelastic Mean Free Path (IMFP) and Stopping Powers (SP) has been achieved. Here we discuss the basic theories of stopping powers developed by Bohr and Bethe and the higher order correction schemes applied to these theories. The

dielectric function theory has been discussed in detail in the chapter 6 as it is the basis for the work carried out on calculations of stopping power of GaAs using the optical data model.

In all the stopping theories the central theme is perturbation theory. In classical and semiclassical treatment electronic energy loss is expressed as a function of momentum  $p$ , from which stopping cross section is calculated by integration (see Fig 1.3).

$$S = \int T(p) 2 \pi p dp \quad (1.8)$$

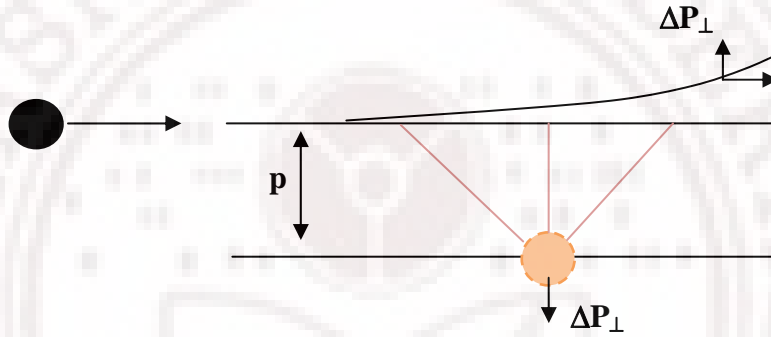


**Fig 1.3.** Momentum dependence of scattering: A soft scattering event with momentum transfer  $\Delta P_{\perp}$ .

#### 1.1.2.1 Bohr's stopping formula

Bohr treated the atomic electrons as harmonic oscillators bound to their atomic sites [4]. Each electron is characterized by a resonance frequency  $\omega_0$ . Equation of motion for classical electron bound to origin by a force  $-k\mathbf{r} = -m\omega_0^2\mathbf{r}$  is given by

$$\frac{d^2\mathbf{r}}{dt^2} + \omega_0^2\mathbf{r} = -\frac{e}{m}\mathbf{E}(\mathbf{r}, t) \quad (1.9)$$

where  $\mathbf{E}(\mathbf{r}, t)$  is the electric field generated by the projectile.

For simplicity, here we ignore the position dependence of electric field and solve the equation to get  $\mathbf{r}(t)$ . One can calculate the energy taken up from the field by the oscillators at its resonance frequency, to get

$$T = \frac{1}{2m} \left| \int_{-\infty}^{\infty} dt (-e\mathbf{E}(t)) e^{i\omega_0 t} \right|^2 \quad (1.10)$$

This equation still contains the unknown  $\mathbf{r}(t)$  term through  $\mathbf{E}(t) \equiv \mathbf{E}(\mathbf{r}, t)$ . Now we apply dipole approximation to the coulomb field and we now drop the  $\mathbf{r}(t)$  term in the electric field generated by the projectile. Now the Fourier transform of  $\mathbf{E}(\mathbf{r}, t)$  is given by

$$E(\omega) = -\frac{iZ_1 e}{2\pi^2} \int d^3 \mathbf{q} \frac{\mathbf{q}}{q^2} e^{-i\mathbf{q} \cdot \mathbf{p}} \delta(\omega - \mathbf{q} \cdot \mathbf{v}) \quad (1.11)$$

where  $\delta(\dots)$  is the Dirac delta function. Now the integration can be carried out in cylindrical coordinates according to Abramowitz and Stegun [14]. Now substituting the final  $E(\omega)$  substituting in Eq1.10 we get.

$$T = T(p) = \frac{2Z_1^2 e^4}{mv^2 p^2} f(p) \quad (1.12)$$

with

$$f(p) = f_{dist}(p) = \left[ \frac{\omega_0 p}{v} K_0\left(\frac{\omega_0 p}{v}\right) \right]^2 + \left[ \frac{\omega_0 p}{v} K_1\left(\frac{\omega_0 p}{v}\right) \right]^2 \quad (1.13)$$

Both the Bessel functions  $K_0$  and  $K_1$  decay exponentially at  $\omega_0 p/v \gg 1$ . And its relativistic extension is given by

$$f(p) = f_{dist}(p) = \frac{1}{\gamma^2} \left[ \frac{\omega_0 p}{\gamma v} K_0\left(\frac{\omega_0 p}{\gamma v}\right) \right]^2 + \left[ \frac{\omega_0 p}{\gamma v} K_1\left(\frac{\omega_0 p}{\gamma v}\right) \right]^2 \quad (1.14)$$

where  $\gamma = 1/\sqrt{1 - v^2/c^2}$

Before calculating the stopping cross section, we need to remove the logarithmic divergence at small  $p$  in the Eq 1.12. Bohr achieved this by adopting Rutherford's law of free coulomb scattering for close collisions.

$$f(p) = f_{close}(p) = \frac{1}{1 + (b/2p)^2} \quad (1.15)$$

where  $b = 2Z_1 e^2 / mv^2$ . With this, now we split up the integration into two parts “dist” and “close” and write the final stopping cross section as

$$S = S_{close} + S_{dist} \quad (1.16)$$

where

$$S_{close} = \frac{4 \pi Z_1^2 e^4}{m v^2} \ln \frac{2 p_0}{b} \quad (1.17)$$

$$S_{dist} = \frac{4 \pi Z_1^2 e^4}{m v^2} \ln \frac{2 v e^{-\gamma}}{\omega_0 p_0} \quad (1.18)$$

Which yield the Bohr's stopping power formula

$$S = \frac{4 \pi Z_1^2 e^4}{m v^2} \ln \frac{C m v^3}{|e_1 e| \omega_0} \text{ with } C=1.1229 \quad (1.19)$$

### 1.1.2.2 Bethe's stopping formula

In Bethe's formula [5] physic remains same as Bohr's model where motion of nuclei is treated by classical mechanics and that electrons are treated as quantum mechanically and can have quantum states in a target atom. Here we calculate excitation probability  $P_j(p)$  for each excitation level  $j$  of the target corresponding to resonance frequency  $\omega_{j0}$ . Which is related to the quantity  $T(p)$  of classical theory as

$$T(p) = \sum_j P_j(p) \hbar \omega_{j0} \quad (1.20)$$

The stopping cross section if given by

$$S = \sum_j \hbar \omega_{j0} \int 2 \pi p dp P_j(p) \quad (1.21)$$

Now we define excitation cross section to level  $j$  as

$$\sigma_j = \int 2 \pi p dp P_j(p) \quad (1.22)$$

The resonance frequency of an atom in its ground state is given by

$$\hbar \omega_{j0} = \epsilon_j - \epsilon_0 \quad (1.23)$$

where  $\epsilon_j$  and  $\epsilon_0$  are the  $j^{\text{th}}$  state and ground state energies of the target electrons, respectively.

The electron motions are governed by Schrodinger's equation

$$(H + V)\psi(\mathbf{r}, t) = i\hbar \frac{\partial \psi(\mathbf{r}, t)}{\partial t} \quad (1.24)$$

where  $H$  is the Hamiltonian of an isolated target atom and the potential of interaction with projectile is given by

$$V(\mathbf{r}, t) = \sum_{v=1}^{Z_2} \frac{-Z_1 e^2}{|\mathbf{r}_v - \mathbf{R}(t)|} \quad (1.25)$$

where  $\mathbf{r}_v$  is the position operator of the  $v^{\text{th}}$  electron and  $\mathbf{R}(t) = \mathbf{p} + \mathbf{v}$  is the projectile trajectory. The time dependent wave function  $\psi(\mathbf{r}, t)$  is expanded in terms of stationary states.

$$\psi(\mathbf{r}, t) = \sum_j c_j(t) e^{-i\epsilon_j t/\hbar} |j\rangle \quad (1.26)$$

By using first order perturbation theory the coefficients  $c_j(t)$  are expanded in powers of perturbing potential. The transition probabilities are calculated within the first order perturbation theory, which is given below

$$P_j(p) = |c_j^1(\infty)|^2 \quad (1.27)$$

Using the equations 1.22 and 1.27 we can calculate excitation cross section. Here one gets general expression for excitation cross section for uniform motion of a projectile with electrons in target atoms within the first Born approximation. Considering the target atoms as randomly oriented, we carry out the integration on angular part of the incident velocity to get following expression for the excitation cross section,

$$\sigma_j = \frac{2\pi Z_1^2 e^4}{mv^2} \int \frac{dQ}{Q^2} |F_{j0}(\mathbf{Q})|^2 \quad (1.28)$$

where  $Q = \hbar^2 q^2 / 2m$  with boundary condition  $2mv^2 Q > (\epsilon_j - \epsilon_0)^2$

Bethe used same classification “dist” and “close” as proposed by Bohr, but he used the classification based on momentum. A distant interaction corresponds to low momentum transfer and vice versa. For  $Q < Q_0$  dipole approximation can be used. Now the stopping integration for low  $Q$  is given by

$$S_{dist} = \sum_j f_{j0} \int_{(\epsilon_j - \epsilon_0)^2 / 2mv^2}^{Q_0} Q d\sigma_R(Q) \quad (1.29)$$

The upper limit corresponding to the maximum energy transfer in close collisions, to a free target electron at rest is  $Q_{max} = 2mv^2$  and we can write,

$$S_{close} = \int_{Q_0}^{2mv^2} Q d\sigma_R(Q) \sum_j f_{j0}(Q) \quad (1.30)$$

Applying the Bethe's sum rule  $\sum_j f_{j0}(Q) = 1$  and adding both the contributions, final stopping formula is given by

$$S = S_{dist} + S_{close} = \sum_j f_{j0} \int_{(\epsilon_j - \epsilon_0)^2 / 2mv^2}^{2mv^2} Q d\sigma_R(Q) \quad (1.31)$$

Applying the free coulomb scattering cross section  $d\sigma_R(T)$ , we arrive at the final Bethe's stopping formula

$$S = \frac{4\pi Z_1^2 e^4}{mv^2} Z_2 \ln \left( \frac{2mv^2}{I} \right) \quad (1.32)$$

with mean logarithmic excitation energy  $I$  defined by

$$\ln I = \sum_j f_{j0} \ln (\epsilon_j - \epsilon_0) \quad (1.33)$$

This Bethe's stopping formula is valid in the limit of higher projectile speed. Also the mass of the projectile should be larger than electrons. For both the theories, the validity and applicability at relativistic regime do not yield good agreement with experimental observations. Hence it is important to use higher order corrections at high projectile energies.

### 1.1.2.3. Bethe-Bolch stopping formula

Bethe's approach was necessary since quantum mechanics prohibits a particle with a well defined momentum having a spatially localized position. Hence Bohr's concept of an impact parameter (defined in 1913, before quantum mechanics was developed) could not be directly upgraded to wave mechanics. There was no quantized solution to close collisions if one attempted to use the Bohr impact parameter concepts. The classical Bohr approach considers a heavy charged particle of charge,  $Z_1e$ , moving at a velocity,  $v$ , passing near a light electron of charge  $e$ , and mass  $m$ , at an impact parameter  $b$ . The transverse momentum impulse  $\Delta p$ , to the light electron is [15, 16]:

$$\Delta p = \int_{-\infty}^{\infty} e\bar{E}(t) dt = \frac{2Z_1e^2}{bv} \quad (1.34)$$

where  $E$  is the transverse electrical field. The energy transferred is then:

$$\Delta E = \frac{(\Delta p)^2}{2m} = \frac{2Z_1^2e^4}{mv^2} \left( \frac{1}{b^2} \right) \quad (1.35)$$

This expression assumes that the electron does not move much relative to the impact parameter  $b$ . To obtain the stopping power  $S$ , this transferred energy must be integrated over all possible impact parameters  $b$ . Assuming the target atomic number as  $Z_2$ , the energy loss per target atom is :

$$S = 2\pi Z_2 \int \Delta E(b) \quad (1.36)$$

$$= 4\pi Z_2 \frac{Z_1^2e^4}{mv^2} \int_0^{\infty} \frac{1}{b^2} b db \quad (1.37)$$

The integral of this expression diverges as  $b \rightarrow 0$ , so it is necessary to argue a minimum impact parameter,  $b_{\min}$ . If the electron mass is assumed to be very much smaller than the mass of the incident particle, the electron will recoil strongly for very small impact parameters. Noting that the maximum energy transfer is for a head-on collision, we may

use Rutherford two-particle elastic scattering to estimate the closest distance of approach for a head-on collision. This gives a minimum distance of approach as,

$$b_{\min} = \frac{Z_1 e^2}{mv^2} \quad (1.38)$$

The integral also becomes undefined for  $b_{\max} \rightarrow \infty$ . This can be made tractable by noting that for distant collisions, if the interaction is long range compared to the orbiting frequency of an electron, the collision will become adiabatic and no energy will be transferred. This suggests a cutoff when the collision time becomes longer than the orbital frequency,  $b_{\max} \sim v/\omega$ , where  $\omega$  is the orbital frequency.

Inserting these values for  $b_{\min}$  and  $b_{\max}$ , the energy loss becomes:

$$\frac{dE}{dx} = 4\pi Z_2 \frac{Z_1^2 e^4}{mv^2} \ln \left( \frac{mv^3}{Z_1 e^2 \omega} \right) \quad (1.39)$$

The relativistic form of this equation is obtained by equating the particle's energy,  $E = \gamma M_1 c^2$ , where  $\gamma = 1/(1-\beta^2)^{1/2}$  and  $\beta = v/c$ . This implies  $b_{\max} \sim \gamma v/\omega$ , and  $b_{\min} \sim Z_1 e^2/\gamma m v^2$  and the integral becomes [14]

$$\frac{dE}{dx} = \frac{4\pi Z_2 e^4}{mv^2} Z_1^2 \ln \left( \frac{\gamma^2 m v^3}{Z_1 e^2 \omega} \right) \quad (1.40)$$

Bohr used this expression to form the basis of his evaluation of the energy loss of a heavy particle to a medium of harmonically bound electrons.

Let us estimate the energy loss ( $-dE/dx$ ) suffered by an incident charged particle when it interacts with a free and initially stationary electron. We refer to the collision cylinder of radius  $b$  as the impact parameter and its length to be the small distance traveled,  $dx$  as shown in Fig.1.4.



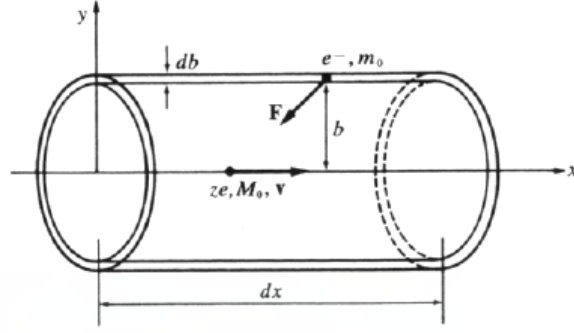


**Fig.1.4:** Interaction of heavy charged particle of mass  $M_0$  and a free electron of mass  $m_e$ . The impact parameter  $b$  is indicated

The net momentum transferred to the electrons as the particle moves from one end of the cylinder to the other end is essentially entirely directed in the perpendicular direction ( $F_x$  changes sign so the net momentum along the horizontal direction vanishes) along the negative y-axis. So, we can write

$$\int dt F_x(t) \approx 0 \quad (1.41)$$

$$\begin{aligned} p_e &= \int F_y(t) dt \\ &= \int \frac{Z_1 e^2}{x^2 + b^2} \frac{b}{(x^2 + b^2)^{1/2}} \frac{dx}{v} \\ &\equiv \int \frac{Z_1 e^2 b}{v} \int_{-\infty}^{\infty} \frac{dx}{(x^2 + b^2)^{3/2}} = \frac{2Z_1 e^2}{vb} \end{aligned}$$

The kinetic energy transferred to the electron is therefore

$$p_e^2 = \frac{2(Z_1 e^2)^2}{m_e b^2 v^2} \quad (1.42)$$

If we assume this is equal to the energy loss of the charged particle, then multiplying by  $nZ_2 (2\pi b dbdx)$ , the number of electrons in the collision cylinder, we obtain

$$-\frac{dE}{dx} = \int_{b_{\min}}^{b_{\max}} nZ_2 2\pi b db \frac{2}{m_e} \left( \frac{Z_1 e^2}{vb} \right)^2$$

$$= \frac{4\pi(Z_1 e^2)^2 n Z_2}{m_e v} \ln\left(\frac{b_{\max}}{b_{\min}}\right) \quad (1.43)$$

Where  $b_{\max}$  and  $b_{\min}$  are the maximum and minimum impact parameters and depend on the physical description of the problem.

In reality the atomic electrons are of course not free electrons, so the charged particle must transfer at least an amount of energy equal to the first excited state of the atom. If we consider a time interval of energy transfer to be  $\Delta t \approx b/v$ , then  $(\Delta t)_{\max} \sim I/v$ , where  $h\nu = \langle I \rangle$  is the mean ionization potential. Then,

$$b_{\max} = \frac{h\nu}{\langle I \rangle}$$

An empirical expression for  $I$  is  $I \approx kZ_2$ , with  $k \sim 19 \text{ eV}$  for H and  $\sim 10 \text{ eV}$  for Pb. We estimate  $b_{\min}$  by using the uncertainty principle to say that the electron position cannot be specified more precisely than the de Broglie wavelength in the center of mass coordinate system of the electron and the charged particle. Since electron momentum in this coordinate system is  $m_e v$ , we find,

$$b_{\min} = \frac{h}{m_e v} \quad (1.44)$$

Combining these two, we obtain

$$-\frac{dE}{dx} = \frac{4\pi Z_1^2 e^4 n Z_2}{m_e v} \ln\left(\frac{2m_e v^2}{\langle I \rangle}\right) \quad (1.45)$$

In the above eq. (1.45) a factor of 2 has been included in the argument of the logarithm. This is to make the formula agree with the result of quantum mechanical calculation which was first carried out by Bethe using the Born approximation. Physical argument here is that approximately, distant and close collisions contribute equally to the stopping process.

Eq.(1.45) describes the energy loss due to particle collisions in the nonrelativistic regime. One can include relativistic effects by replacing the logarithm by,

$$\ln\left(\frac{2m_e v^2}{\langle I \rangle}\right) - \ln\left(1 - \frac{v^2}{c^2}\right) - \frac{v^2}{c^2} \quad (1.46)$$

This equation is a relatively simple expression, yet one can gain much insight into the factors that govern the energy loss of a charged particle by collisions with the atomic electrons. We can see why one can usually neglect the contributions due to collisions with nuclei. In a collision with a nucleus the stopping power would increase by a factor  $Z_2$ , because of the charge of the target with which the incident charged particle is colliding, and decrease by a factor of  $m_e/M(Z)$ , where  $M(Z)$  is the mass of the atomic nucleus. The decrease is a result of the larger mass of the recoiling target. Since  $Z_2$  is always less than 102 whereas  $M(Z)$  is at least a factor of  $2 \times 10^3$  greater than  $m_e$ , the mass factor always dominates over the charge factor. Another useful observation is that Eq(1.45) is independent of the mass of the incident charged particle. This means that nonrelativistic electrons and protons of the same velocity would lose energy at the same rate.

The original Bethe-Bloch relativistic stopping formula,  $S$  may now be written as:

$$S = \frac{4\pi e^4 Z_2}{m_e v} Z_1^2 \left[ \ln\left(\frac{2m_e v^2}{\langle I \rangle}\right) - \ln(1 - \beta^2) - \beta^2 + \Psi(Z_1) \right] \quad (1.47)$$

Where  $\langle I \rangle$  is the mean ionization potential per electron. In an effort to improve further, Fano [17] described a relativistic version of Bethe-Bloch energy loss formula where two additional corrective terms are included; the shell correction term  $C/Z_2$  and the density effect correction term  $\delta/2$ . Thus he wrote stopping power formula as,

$$S = \frac{4\pi e^4 Z_2}{m_e v} Z_1^2 \left[ \ln\left(\frac{2m_e v^2}{\langle I \rangle}\right) - \ln(1 - \beta^2) - \beta^2 - \frac{C}{Z_2} - \frac{\delta}{2} \right] \quad (1.48)$$

which is simplified using the definitions,

$$r_o \equiv e^2 / mc \quad (\text{the Bohr electron radius})$$

$$f(\beta) \equiv \ln \left[ \frac{2mc^2 \beta^2}{1 - \beta^2} \right] - \beta^2 \quad (1.49)$$

$$S = \frac{4\pi r_o^2 m_e c^2 Z_2}{\beta^2} Z_1^2 \left[ f(\beta) - \ln \langle I \rangle - \frac{C}{Z_2} - \frac{\delta}{2} \right] \quad (1.50)$$

Thus, the final simplified form of the Bethe-Bloch stopping formula may be written as,

$$S = \frac{k Z_2}{\beta^2} Z_1^2 [L_0(\beta) + Z_1 L_1(\beta) + Z_2^2 L_2(\beta)] \quad (1.51)$$

where  $L_0$ , contains the empirical shell corrections proposed by Fano [17] and also the density effect corrections.

#### 1.1.2.4 Barkas Correction

The higher order corrections are mandatory as these theories did not explain some important experimental results

- (i) Experimental evidence that stopping power for positive and negative ions of same velocity and same atomic number differ.
- (ii) Charge state dependence of the stopping power.

The Barkas effect named after Walter Barkas, who discovered the difference in range of positive and negative pions. He showed that the ranges of negative ions are longer than those of positive ones. He explained it by correction to the first order Born approximation of the Bethe-Bloch equation [18]. Positive ions tend to pull the electrons toward its trajectory, but the negative particles tend to repel them. H H Anderson et.al [19] gave different understating for the higher order term by conducting series of experiments. They reported stopping power ratio exceeds the  $Z_1^2$  scaling factor given as.

$$Z_1 L_1(\text{Barkas term}) = L_0 \frac{Z_1}{Z_2^{1/2}} \left[ \frac{2.68}{V^2} (1 - 0.264 \ln V) \right] \quad (1.52)$$

$$V = (v/v_0 Z_2^{1/3})$$

#### 1.1.2.5 Bloch correction

Bloch considered the interaction to be of free particles as in Bohr's model. He has shown that higher order terms like  $Z_1^4$  are also necessary for the larger impact parameter [20]. Modern evaluations of Bloch term have been reviewed by Sigmund [21]. It has been observed that the contributions of these corrections are negligible in low velocity regime. Bichsel has proposed a simple parameterization of the Bloch correction, which fits a wide range of stopping power data [22].

$$Z_1^2 L_2 = -y^2 [1.202 - y^2 (1.042 - .0855y^2 + 0.343y^4)] \quad (1.53)$$

$$\text{where } y = \frac{Z_1 \alpha}{\beta} \quad (\alpha = \frac{1}{137})$$

This expression is derived in conjunction with Bichsel's calculations of the other stopping numbers  $L_0$  and  $L_1$  of Eq (1.51). Since this Bloch correction term is quite small in low velocity regions, his formula is used widely for high energy regions.

### 1.2 Materials of Interest

III- Nitride semiconductors are novel class of materials for optoelectronics, high power and high temperature device applications. A wide range of optical devices are possible such as Blue Light Emitting Diode (LED), violet Laser Diode (LD), UV photo detectors and High Electron Mobility Transistors (HEMTs). These devices were demonstrated for higher frequency operation, higher power handling and wide temperature range of operations. The recent developments in epitaxial growth by MBE and MOCVD have initiated new interest in this field. Recent development in the processing of such materials

and relevant device fabrication and possible future trends have been reviewed extensively in the literature (23-28).

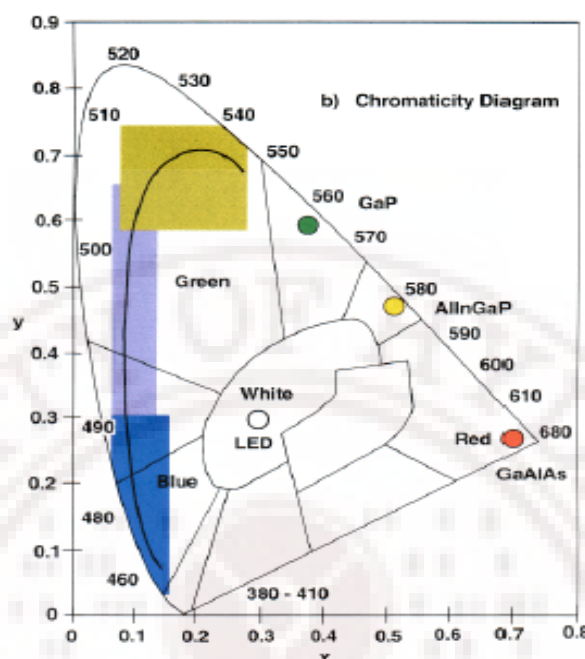


**Fig 1.5.** Positions of the GaP, AlInGaP and GaAs LEDs and regions which can be covered by InGaN LEDs.

As members of the III-Nitrides family, AlN, GaN, InN and their alloys are wide band gap materials and can crystallize in both wurtzite and zincblende polytypes. Wurtzite GaN, AlN and InN have direct band gap values of 3.4eV, 6.2eV and 0.7 eV, respectively seen clearly in Fig 1.6. In cubic form, GaN and InN are direct band-gaps while AlN is indirect bandgap. GaN alloyed with AlN and InN may span a continuous range of direct band-gap energies throughout much of the visible spectrum well into the UV wavelengths. This makes the nitride systems attractive for optoelectronic device applications. Nitride based Laser diode makes it possible to increase the storage capacity of DVDs upto 40 GB. As a reverse process, these materials can be used for Ultra violet photo detectors and solar blind detectors. These devices are used in monitoring combustion processes, visibility through fog and smoke and solar astronomy.

The addition of III-Nitride to the family of device-quality semiconductors is essential for developing full-color displays. Particularly, combination of GaN based blue and green LEDs with GaAs based red LEDs form the basis for large scale full displays and white light illumination. The solid-state white light sources generated by mixing the primary

colors in a light scrambling configuration would provide not only compactness and high lifetime, but also would reduce power consumption by 80-90% compared to incandescent or fluorescent light sources.

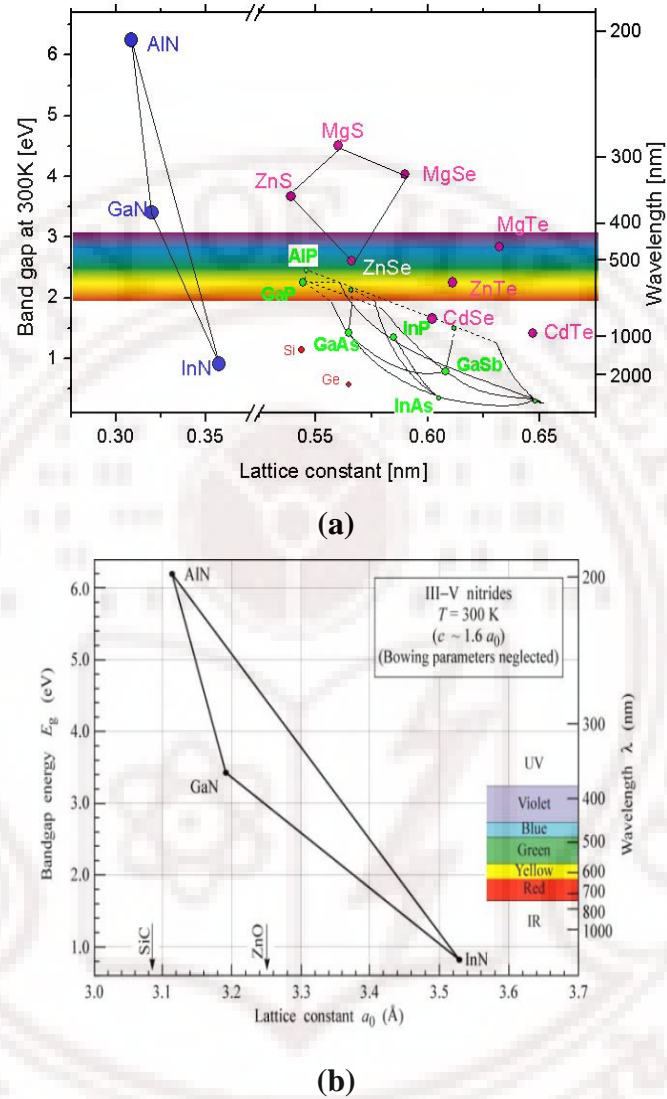


**Fig 1.6.** Band gap versus lattice constant of (a) III-Nitrides compared with different semiconductor materials (b) III-Nitrides

The strongest feature of the III-Nitrides compared to SiC, is that it can support the hetero-structure technology. Quantum Wells (QWs), modulation doped hetero-interface and hetero-junction structures can be made in these systems. This opens access to new spectral regions for optical devices and new operation regimes for electronic devices. However, there are some challenges in the III-Nitrides: (i) To develop the good quality substrates by reducing the dislocation density and reduction in residual stress. (ii)



Production of low resistive contact in p-type material and reduction of the migration of metal contacts. (iii) Achieving controlled p-type and n-type doping:  $\sim 1 \times 10^{17} \text{ cm}^{-3}$  (channel doping) and  $\sim 1 \times 10^{19} \text{ cm}^{-3}$  (contact doping). (iv) Smoothing interface in AlGaN/GaN and hence reduce the trap density. (v) Enhancement of the output efficiency. (vi) Polymer package degradation.

Another area gaining a lot of attention for III-Nitrides is high temperature and high power electronics. III-Nitrides are ideal materials for power applications possessing excellent transport and thermal properties, high breakdown voltage, chemical inertness, mechanical stability. It can be used to fabricate both unipolar and bipolar devices with low parasitic resistance.

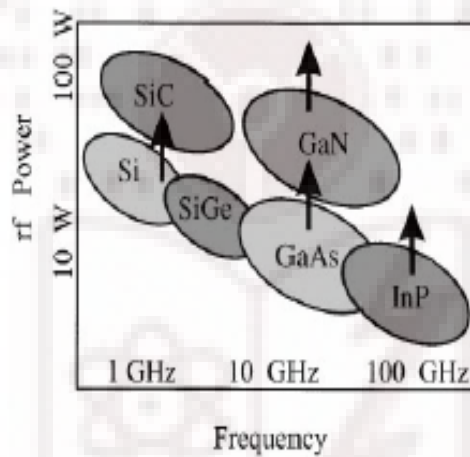


**Fig 1.7.** Figure showing RF power output of GaN with other semiconductors.

Most of the power devices today are made from Si or GaAs. However, wide band gap semiconductor materials have attracted much attention due to their potential applications in devices. A comparison of GaN material's frequency of operation with other semiconductor materials are given in Fig 1.7. GaN based power devices can operate with less cooling and fewer high cost processing steps associated with complicated structures designed to maximize heat extraction. Another attractive property of III-Nitrides is that they have high breakdown field. An estimated breakdown electric field in GaN is of the order of  $3 \text{ MVcm}^{-1}$ , as compared to  $0.3$  and  $0.4 \text{ MVcm}^{-1}$  for Si and GaAs respectively. Beyond this GaN also has an excellent electron transport property. The electron velocity in GaN is less sensitive to temperature than that in GaAs. Hence GaN devices are more tolerant to self-heating and clearly more suitable for high temperature operation. Hetero-



junctions of these materials have large carrier velocities and carrier concentration in 2D system. It has large band discontinuities tolerance for the high junction temperatures. These materials are the best candidates for the micro-wave electronics for base stations of cell phones. A list of various High Electron Mobility Transistor (HEMT) devices fabricated based on GaN materials and their performances are given below in Table 1. The challenges in fabrication of HEMT devices are (i) Making of high resistive material epilayers with low defect density for low leakage current in buffer. (ii) Growing the high quality material substrate and proper surface passivation to achieve very high breakdown voltage. (iii) Maximizing the Al mole fraction without strain relaxation in AlGaIn/GaN system to improve sheet charge density. (iv) Reducing of the scattering centers like dislocation, interface roughness and alloy disordering to increase the electron mobility.

**Table 1.** Electrical properties of different AlGaIn/GaN based transistors

Transistor	Heterostructure	Source drain Gate length Gate width ( $\mu\text{m}$ )	$f_t$ (GHz)	$f_{\text{max}}$ (GHz)	Gain (dB)	Power (W mm $^{-1}$ )	Breakdown voltage (V)
HFET [343]	Al <sub>0.3</sub> Ga <sub>0.7</sub> N/GaN	0.15–0.33	67	140	12.8	1.4	70
HFET [336]	Al <sub>0.25</sub> Ga <sub>0.75</sub> N/GaN	0.25–0.7	37.5	80		2.3–2.8	
DHC MODFET [337]	Al <sub>0.15</sub> Ga <sub>0.85</sub> N/GaN/ Al <sub>0.15</sub> Ga <sub>0.85</sub> N/GaN	1.5–1.75 40					80
MODFET [338]	Al <sub>0.15</sub> Ga <sub>0.85</sub> N/GaN	4 1.0–1.5 75	9.6	27.2	5.1	2	230–340
MODFET [303]	Al <sub>0.2</sub> Ga <sub>0.8</sub> N/GaN						
MODFET [339]	Al <sub>0.175</sub> Ga <sub>0.825</sub> N/GaN	0.4 0.25 100	50	92	6.2	1.7	80
Transistor	$n_e$ (cm $^{-3}$ )	Channel current (mA mm $^{-1}$ )	Trans- conductance (mS mm $^{-1}$ )	Mobility (300 K) (cm $^2$ V $^{-1}$ s $^{-1}$ )			
HFET [343]							
HFET [336]	$1.5 \times 10^{13}$	700	180				
DHC MODFET [337]	$3.7 \times 10^{13}$	1100	270	304			
MODFET [338]		300	130	1500			
MODFET [303]	$1.3 \times 10^{13}$			2019			
MODFET [339]	$8 \times 10^{12}$	800	240	1200			

Interestingly the properties of the group III-Nitrides enable the fabrication of LEDs, LDs, Detectors, Transistors and Surface Acoustics Wave (SAW) devices on single chip, which offers Monolithic structures (see Fig 1.9) combination of electrical, optical and piezo electric devices.

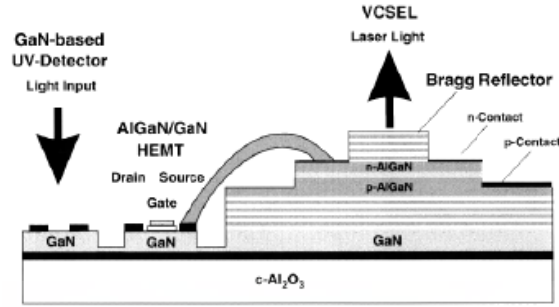


**Fig 1.9.** Schematic picture of Monolithic structure of GaN based UV-detector, HEMT and Laser diode.

### *III-Nitride based optical devices:*

The efficiency began to increase greatly soon after the successes in producing better quality crystals by using the LT-buffer layer method, which resulted in p-n junction LEDs. The blue, green, yellow Single Quantum Well (SQW) LEDs with different 'In' mole fraction of InGaN were fabricated. By changing the Indium composition in the InGaN well layers, one can achieve different LED output colors range from ultraviolet to red. Charge Asymmetric Resonance Tunneling (CART) structures were applied to nitride-based green LEDs to enhance their output efficiency. The output power and external quantum efficiency of the CART LED are about 4 mW and 6.25%, respectively. The output power and external quantum efficiency of the CART LED with Distributed Bragg Reflector (DBR) structures measured can reach 7.2 mW and 11.25%, respectively. The other method to increase the output intensity of green LEDs is to include a DBR structure in the backside of LED wafer.

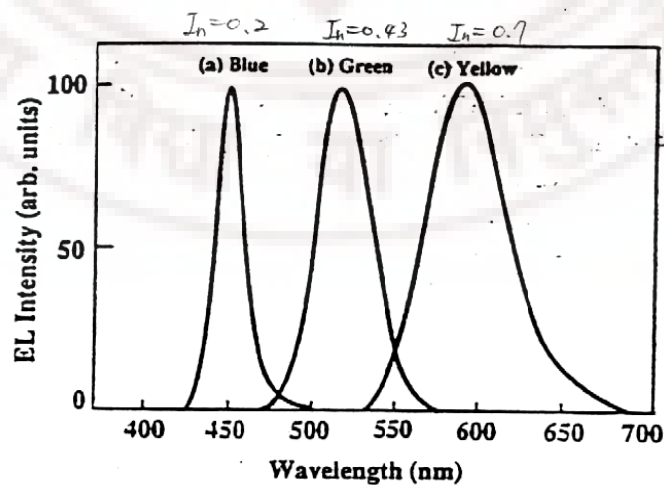


**Fig 1.10.** Electro-Luminescence of different In concentration InGaN based LEDs showing possibilities to make blue, green and red colour LEDs.

The InGaN multi-quantum well (MQW) Laser Diode structure was grown on the GaN structure with Effective Layer Over Growth (ELOG) by MOCVD. The threshold current density and voltage of these LDs with an emission wavelength of 460 nm were 3.3 KA/cm<sup>2</sup> and 4.6 V respectively. The estimated lifetime was approximately 3000 hours under 50 °C continuous-wave operations at an output power of 5 mW.



**Fig 1.11.** Different colour LED's like Blue, Green, Red and White fabricated and commercially available in the market.

### 1.2.1 Works done on ion beam modification of III-Nitrides

Extensive works are going on in ion beam induced modification of semiconductors. Particularly the III-Nitrides semiconductor attracted much interest because of their high technological importance. In a brief review, S.O.Kucheyev et al. [29] has discussed the effects of Al and In content on the defect processes in In<sub>x</sub>Ga<sub>1-x</sub>N and Al<sub>x</sub>Ga<sub>1-x</sub>N alloys. Under MeV ion bombardment strong dynamic annealing process has been reported. As a result of dynamic annealing process planar defects are created. Ion beam generates an equal number of lattice interstitials and vacancies. The interstitials agglomerate to form planar defects. While in the case of electronic energy loss process (i.e. SHI), intense ultrafast excitation of valence electrons occurs along the ion tracks. The effects of SHI irradiation produced by 200 MeV Au ions have been studied by S O Kucheyev et.al [30]. No external defects such as dislocations or stacking faults are visible in the vicinity of the tracks nor is there presence of any amorphous phase. For the fluences above 10<sup>13</sup> cm<sup>-2</sup>

delimitation of the GaN layer has been observed and attributed to ion- beam induced rearrangement and weakening of atomic bonds at the film/substrate interface and build up of stress in both sapphire and GaN film.

In recent years, the effects of ion irradiation produced defects in InGaN, AlGaN and AlN have been reported [31-35]. In  $\text{In}_x\text{Ga}_{1-x}\text{N}$  layers, an increase in 'In' content suppresses the dynamic annealing process and weakens the effect of damage saturation. But in  $\text{Al}_x\text{Ga}_{1-x}\text{N}$ , the level of dynamic annealing increases with Al content. This has been attributed to the larger (smaller) energy of the Al-N (In-N) bond as compared to the energy of the Ga-N bond. The efficiency of dynamic annealing depends also on the other parameters like chemical bond. By varying the other parameters one can change the damage build up behavior. A better understanding of the physical mechanism of dynamic annealing in III-Nitrides is needed.

Ion irradiation can make the material highly resistive under suitable conditions and hence, can be used for spatial electrical isolation. Electrical isolation of GaN by MeV light ion irradiation has been reported by several authors [36-40]. It has been shown that the sheet resistance is increased by more than 7 orders as a result of ion irradiation. Defect complexes and anti-site-related defects are responsible for the electrical isolation, for effective electrical isolation it is important to account for necessary conditions.

RBS/C has been used extensively for the compositional and structural characterization of InGaN and AlGaN [41-45]. RBS with channeling geometry gives information about both "In" and "Al" concentration and defects density in InGaN and AlGaN samples. The influence of the "In" content on the accumulation of the structural damage in  $\text{In}_x\text{Ga}_{1-x}\text{N}$  films under ion bombardment has been studied using RBS/C [42]. Elastic strain in the  $\text{In}_{0.18}\text{Ga}_{0.82}\text{N}$  on the GaN substrate has been measured by this technique and indicates that the layer is much stiffer along the c-axis compared to the a-axis direction [43]. Similar work has been done by other groups to measure the elastic strain in the  $\text{In}_{0.18}\text{Ga}_{0.82}\text{N}$  and  $\text{Al}_{0.28}\text{Ga}_{0.72}\text{N}$  [44]. RBS/C has been used to gain insight into compositional depth profile of 75nm thick InGaN in the growth direction [45]. Recently RBS/C has been used to study the evolution of the structural defects in  $\text{Al}_x\text{Ga}_{1-x}\text{N}$  films irradiated with KeV heavy ions [41].

First report on swift heavy ion beam induced mixing [46] was published in 1993. The study of SHI is also very useful for the understanding of basic interaction of swift heavy ions with materials in general. It was shown that incident ions produce mixing at the interface and the recoils generated by the incident ions may provide information about the changes at the interface [47, 48]. A thin Fe film deposited on Si substrate has been utilized to show mixing of Fe with Si at the interface with 230 MeV Au ions, which was also monitored online [49]. Online ERD with large area and position sensitive detectors incorporating kinematical correction provides a unique way of studying such interface processes.

Ion beam modification is not yet understood fully in III-V semiconductors in general and III- Nitride materials in particular. Through some detailed experiments with back up of theoretical calculations, the basic mechanism of modification can be understood. Developing technology for III-V material modification after growth is advantageous from device point view. Post growth modification of the materials by ion beams are promising application like for example, ion implantation. Controlled modification and optimization of the parameters are important to develop the technology. Establishing ion channeling for III-Nitride heterostructures and MQWs as reliable characterization technique is an important step in this direction. Defect characterization through ion channeling will give both quantitative and qualitative information using simulation. We have tried to make progress in some of these areas as discussed below.

The third chapter describes the results of high energy irradiation effects on bulk epitaxial GaN layers. Effects of irradiation on the previously existing defects and hence optical properties are also studied. RBS/C energy dependence analysis, HRXRD, AFM and optical studies have been carried out on all the samples. We observed that after irradiation, the bandgap decreases, residual strain increases and also dislocation density increases due to irradiation. These observations have been attributed to the fact that the irradiation induced reconstruction of the Low Temperature (LT) GaN buffer layers results in induced dislocations.

In the fourth chapter, the effects of swift heavy ion irradiation on AlGaIn/GaN heterostructures are described. These layers are initially partially relaxed and the effects of SHI are studied before and after irradiation. HRXRD and RBS/Channeling studies



show that strain is induced in the AlGaIn layers and the residual strain of the GaN layer also increases after irradiation. However, increase in defect density after irradiation has been attributed to the strain released at the GaN buffer layer.

The fifth chapter describes the systematic studies of the Er implanted GaNs with different doses and annealing temperatures. Time-resolved Photo Luminescence and RBS/Channeling lattice location studies have been carried out. PL studies combined with RBS/Channeling give an insight into the mechanism of Er luminescence activation in GaN matrix. Also Er site dependence on the annealing temperature and implantation dose has been studied in detail. An optimal condition of annealing and implantation dose for good quantum efficiency has been achieved.

In the sixth chapter we have carried out the theoretical calculations for stopping power of GaAs using dielectric function theory and optical data model. A new parameterization of the energy-loss function (ELF) of GaAs is presented in the spirit of the Ritchie-Howie formalism. A linear superposition of Drude-type functions is used to analytically represent the experimental optical data. The internal consistency of our parameterization was ensured by a near-exact fulfillment of both the  $f$ - and KK-sum-rules. To account for shell-corrections to all orders in the projectile velocity, in an approximate yet self-consistent manner, a simple quadratic dispersion relation is used to extend the ELF to finite momentum transfers. Stopping power (SP) calculations for swift protons in GaAs are found to be in very good agreement with the experimental data

The final chapter gives the overall conclusion of the thesis and the outlook for the possibilities of future works to be carried out along the same direction.

### **1.3 Probing Techniques and Descriptions**

Our main aim is to study the changes in the optical and electronic properties by SHI irradiation. Photo Luminescence and other Optical studies namely transmission /reflectance would help in understanding the mechanism of radiative recombination. RBS/C will give compositional depth profiling, and it is a powerful technique to measure the defect density and crystalline quality of the samples. HRXRD would help in measuring the modifications in the elastic properties of the SHI irradiated QW's. HRXRD

and RBS/C in combination will give us quantitative information about the structural and compositional in-homogeneity and strain.

### **1.3.1 Photoluminescence**

Photoluminescence is a powerful technique for investigating the electronic structure of both, semi-insulating as well as intrinsic and extrinsic semi conducting materials. In low dimensional systems, electrons and holes are spatially confined, causing quantum confinement effects. As a result their energy level structures and hence the optical properties become essentially different from those in 3-D systems. In 2-D systems (QW's) both the electrons and holes are quantum-confined. Therefore, the absorption corresponding to the band-to-band transition shifts to higher energies with decreasing well thickness. Also in 1-D and 0-D systems, the absorption shows blue shifts as the characteristic size of the system representing the low dimensionality like well thickness, decreases. So the PL studies would help us in understanding the radiative transitions in the QW's. The shift in the peak energy of the spectra of the QW's can be used to monitor the degree of compositional disordering in the samples. This will be used to correlate the spatial composition variations. Which can be used to correlate the spatial composition variations, the radiative recombination mechanisms in comparison to the SHI irradiated and unirradiated samples.

### **1.3.2 Rutherford Backscattering Spectrometry /Channeling (RBS/C)**

RBS is a widely used technique to determine the composition. In combination with a suitable channeling geometry, it can be used for the defect characterizations, Strain measurements and to find out crystalline quality. Strain measurements are based on the information on the angular shift for lattice directions inclined to the surface normal with respect to the angle of the corresponding direction in the unstrained lattice. In principle can be determined as the angular difference between the channeling dip minimum of the epilayer relative to (undistorted) substrate minimum. We have been studying the dependence of elastic properties on thickness and In composition by RBS/C and HRXRD techniques on the InGaAs/GaAs heterostructures. The basic advantage of this study is the precise determination of layer thickness, composition and defects in GaN based MWQs.

RBS/C combined with HRXRD gives precise and quantitative information about these parameters. Thus it plays a vital role in the device performance.

### **1.3.3 High Resolution X-Ray Diffraction (HRXRD)**

HRXRD has become an essential and versatile tool to characterize heteroepitaxial structures. It is very sensitive to the lattice strain. Point defects are too small to be observed by conventional imaging techniques but they do have appreciable effects on the X-ray intensity profile. With the advent of increasingly perfect single crystal and crystalline layers, a need for refined characterization emerged and HRXRD stands one among the most powerful and non-destructive techniques. Under the optimum conditions, HRXRD is capable of detecting strains with a sensitivity of about  $10^{-5}$ . It also provides information on the interface structure with monolayer precision.

### **1.3.4 Atomic Force Microscopy (AFM)**

AFM is a method for measuring the surface topography of the samples to deep of few angstroms. Here one uses a sharp tip to sense the Van-der Waals force between the tip and the sample surface. The deflection on the tip is measured through optically reflecting arrangements and detectors. This tip is scanned over the sample to measure the variations on the sample giving information about the surface topography. Applications of AFM and other types of scanning probe microscopy continue to grow rapidly in number and include biological materials (e.g., studying DNA structure), polymeric materials (e.g., studying morphology, mechanical response, and thermal transitions), and semiconducting nanomaterials (e.g., detecting defects). In particular, AFM can be utilized to evaluate the surface quality of products such as contact lenses, optical components (mirrors, beamsplitters, etc.), and semiconductor wafers after various cleaning, etching, or other manufacturing processes.

## **References**

1. J F Ziegler, J P Biersack and U Littmark. (Progamon, New York) 1985.
2. P Mazzoldi and G Mattei, Rivista Del NuovoCimento, 28 (2005) 1.  
(DOI 10.1393/ncr/i2006-10005-5)



3. [www.srim.org](http://www.srim.org)
4. N Bohr, Philos. Mag, 25 (1913) 10 & Philos. Mag, 30 (1915) 581.
5. H Bethe, Ann Physik, 5 (1930) 324
6. F Bloch, Ann Physik, 16 (1933) 285.
7. E Fermi, Phys. Rev, 57 (1940) 485.
8. J Lindhard, Mat. Fys Medd Dan Vid Selsk , 28 (1954 ) 1
9. P Sigmund, Particle penetration and radiation effects. Springer series in Solid State Physics, Springer 2005.
10. P Sigmund and A Schinner, Phys Rev Lett, 86 (2001) 1486.
11. Azevedo M de G, P L Grande and G Schiwietz, Nucl. Inst. Meth. B, 164 (2000) 203
12. R H Ritchie, Phys Rev. 114 (1959) 644
13. R H Ritchie and A Howie, Phil. Magz. 36 (1977) 463.
14. M Abramowitz and I A Stegun, (1964) , Handbook of Mathematical functions, Dover, New York.
15. P Sigmund, *Radiation Damage Processes in Materials*, C. DuPuy, ed., Noordhoff, Leiden, 3 (1975).
16. M Inokuti, Rev. Mod. Phys. 43 (1971) 297.
17. U Fano, Ann. Rev. Nucl. Sci. 13 (1963) 67.
18. W H Barkas, N J Dyer and H H Heckmann, Phys. Rev. Lett., 11, 26 (1963).
19. H H Andersen, J F Bak, H Knudsen, P Moller-Petersen and B R Nielsen, "Physics of Ionized Gases", Navinsek (ed.), J. Stefan Institute, Ljubljana, 221 (1976) & H H Andersen, J F Bak, H Knudsen, and B R Nielsen, Phys. Rev., A16, 1929 (1977) & H H Andersen, Physica Scripta, 28, 268 (1983).
20. F Bloch, Ann. Phys., 16, 285 (1933).
21. P Sigmund, Nucl. Inst. Meth. B 85, 541 (1994).
22. H Bichsel, Phys. Rev., A41, 3642 (1990).
23. S C Jain et. al, Jour. Appl. Phys. 87, (2000) 965
24. B Monemar et. al, Progress in quantum electronics. 24, (2000) 239
25. B Monemar et. al, Mat. Sci. Eng. B. 93, (2002) 112
26. S J Pearton et. al, Materials today. June 2002.
27. O Ambacher, J. Phys. D: Appl. Phys. 31 (1998) 2653
28. Shuj Nakamura , JSAP international.1 ( 2000) 5
29. S O Kucheyev et. al, Vacuum 73 (2004) 93

30. S O Kucheyev et. al, Jour. Appl.Phys. 95 (2004) 5360
31. J C Zolper et. al, Appl. Phys. Lett. 66 (1995) 3042
32. C B Vartuli et. al, J. Vac. Sci. Technol. B. 13 (1995) 2293
33. A Y Polyakov et. al, Solid. State. Electronics 41 (1997) 703
34. S O Kucheyev et. al, Appl. Phys. Lett. 80 (2002) 787
35. S O Kucheyev et. al, Jour. Appl. Phys. 92 (2002) 3554
36. H Boundinov et. al, Appl. Phys. Lett. 78 (2001) 943
37. S O Kucheyev et. al, Jour. Appl. Phys. 91 (2002) 4117
38. S O Kucheyev et. al, Jour. Appl. Phys. 91 (2002) 3940
39. A I Titov et. al, Jour. Appl. Phys. 92 (2002) 5740
40. S O Kucheyev et. al, Appl. Phys. Lett. 81 (2002) 3350
41. S O Kucheyev et. al, Jour. Appl. Phys. 95 (2004) 3048
42. S O Kucheyev et. al, Appl. Phys. Lett. 79 (2001) 602
43. M F Wu et. al, Appl. Phys. Lett. 74 (1999) 365
44. M F Wu et. al, Matt. Sci. Eng. B 75 (2000) 232
45. S Pereira et. al, Phys. Rev. B 64 (2001) 205311
46. C Dufour et. al, Euro. Phys. Lett. 1 (1993) 671
47. D K Avasti et. al, Nucl. Instr. Meth. B 156 (1999) 143
48. D K Avasti et. al, Nucl. Instr. Meth. B 166 (2000) 345
49. D K Avasti, et. al, Nucl. Instr. Meth. B 156 (1999) 143

# CHAPTER II

## Experimental details

This chapter gives details of different experimental facilities that have been used in this thesis work. Experimental details regarding the sample growth, irradiation, implantation and characterization are described. Sample identifications (IDs) and other nomenclature have also been defined here. This information will be used throughout the thesis. The details of experimental conditions and analysis that have been used in this thesis work are discussed in detail.

### 2.1 Samples Details

#### (i) GaN

GaN samples studied in the next (third) chapter are thick layers grown on c-plane sapphire substrates by MOCVD in a rotating disk reactor at Ladex Corporation (Taiwan). The typical growth condition involves a low temperature GaN buffer followed by the growth of GaN film at  $\sim 1100 - 1150^\circ \text{C}$ . The thicknesses of the films were  $\sim 2 \mu\text{m}$  as measured from RBS spectra. These layers are unintentionally doped epilayers. A6 sample is  $2 \mu\text{m}$  thick GaN grown on sapphire substrate. A4 sample is also  $2 \mu\text{m}$  thick GaN on sapphire substrate, but **the initial** defect densities vary on this sample with respect to A6 sample. RE48 is AlN (50nm) /GaN ( $2\mu\text{m}$ ) grown on Sapphire. All these samples were grown in typical growth conditions with GaN buffer layers. But in the sample RE48, thin layer of AlN grown to check the nitrogen out gassing on irradiation.

GaN samples used in the Er implantation works (chapter 5) are commercial GaN wafer bought from the TDI Corporation, USA. Typical thickness of the GaN layers is  $\sim 5 \mu\text{m}$ . Small pieces of size  $10 \text{ mm} \times 10 \text{ mm}$  are cut from the wafers and implantation has been carried out.

## (ii) AlGaN

The HEMT structure consisted of a 0.1  $\mu\text{m}$  thick AlN buffer layer and 1  $\mu\text{m}$  thick undoped GaN buffer/channel layer then an undoped 50 nm thick  $\text{Al}_{0.2}\text{Ga}_{0.8}\text{N}$  barrier layer. It was grown in a Vacuum Generator V80H (Mark I) MBE system that was originally used for arsenide materials. Conventional effusion cells were used for Ga and Al deposition, and an Applied Epi Uni Bulb RF-plasma source was used for the active N. During the nitride film growth, the chamber was pumped exclusively by a CTI CT-8 cryopump. The base pressure of the system was always kept below  $5 \times 10^{-11}$  Torr. The substrate temperature was monitored by the substrate heater thermocouple that was calibrated to the SiC wafer surface by observing the melting point of aluminum dots on a SiC test sample. The substrate temperature was kept to  $835^\circ\text{C}$  for 0.1  $\mu\text{m}$  AlN with a growth rate of 0.2  $\mu\text{m}/\text{h}$ . RHEED patterns shows that the growth was slightly Al rich. Now the substrate temperature was reduced to  $735^\circ\text{C}$  for growth of GaN and AlGaN layers. Growth rate of GaN is maintained at 0.37  $\mu\text{m}/\text{h}$ . The growth of AlGaN layer was continued under the same conditions by introducing the Al BEP as Al source. The growth process was completed by shutting the Ga and Al sources and turning off the RF plasma. Finally, the substrate temperature was brought down to room temperature. The final structure of the sample (2024) studied in chapter 4 is given by (50nm)  $\text{Al}_{0.2}\text{Ga}_{0.8}\text{N}$  / (1  $\mu\text{m}$ ) GaN / (0.1  $\mu\text{m}$ ) AlN on SI 4H-SiC. The sample was grown on a quarter of a 2" wafer.

## 2.2 Irradiation and Implantation

All the high energy irradiations were carried out at Inter University Accelerator Center (IUAC), New Delhi high energy accelerator facility (chapters 3 & 4) with 150 MeV Ag ions at fluence of  $5 \times 10^{12}$  ion/ $\text{cm}^2$ . These Ag ions will go to depth of approximately 11.03  $\mu\text{m}$  and 11.13  $\mu\text{m}$  in GaN and substrates respectively, and lose energy at the rate of 24.79 keV/nm in GaN and 22 keV/nm in substrates through electronic interactions For GaN, nuclear energy loss of 150 MeV Ag ions is  $9 \times 10^{-2}$  keV/nm with  $\text{Sn} / \text{S}_e$  ratio as  $3.6 \times 10^{-3}$ . Therefore 150 MeV Ag ions are used to avoid high Sn/Se ratio and possible formation of point defects. We have used these Ag ions based on our previous results on AlGaAs/GaAs samples. To avoid heating of samples a low beam current (0.5 – 2 pA) was maintained. The samples were oriented at an angle of  $5 - 7^\circ$

with respect to the beam axis to minimize channeling. The high vacuum ( $\sim 1 \times 10^{-6}$  mbar) irradiation chamber is shown in Fig.2.1.



Fig 2.1. Irradiation chamber in material science beam line at IUAC, New Delhi

### 2.2.1 IUAC accelerator facility

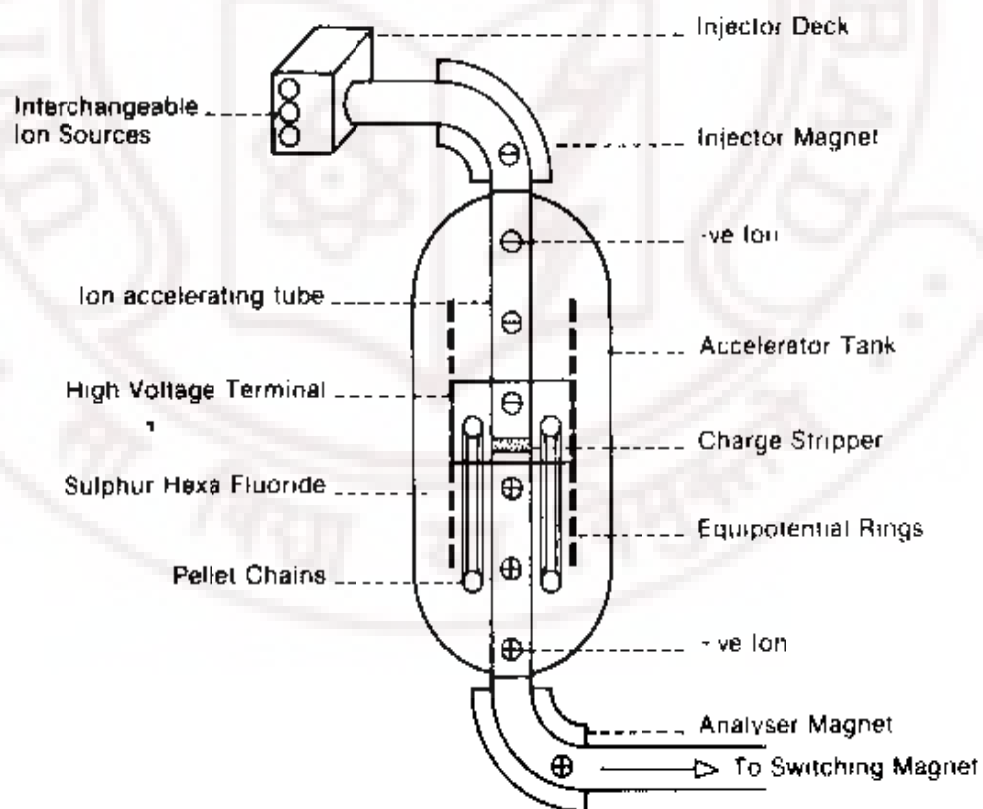


Fig 2.2 schematic of the IUAC 15 MV pelletron accelerator

IUAC is the main accelerator facility for the university community in India. It has many facilities, mainly high energy pelletron accelerator and supporting facilities for accelerator based research in many fields like Material science, Nuclear Physics, Accelerator Mass Spectrometry (AMS) etc. Fig. 2.2 shows the schematic diagram of the pelletron accelerator. It uses the Sources of Negative Ions by Cesium Sputtering (SNICS) to produce the negative ions and these negative ions are pre accelerated to 400 keV and injected into the main accelerator. Here, it uses the SF<sub>6</sub> gas to insulate the high terminal potential from discharging. This accelerator is basically a Van-de Graff accelerator, where the terminal is kept at centre of the accelerating tube. This high voltage terminal (max 15 MV) is charged by using the metal pellet chain, hence it is called pelletron. The negative ions generated from the source are accelerated to the positive terminal, and these get stripped and become positive ions. As a result of repulsive force between terminal positive ions these ions are again accelerated to high energy. These high energy ions are bent through analyzing magnet where the particular ion species, their charge state and beam energy are selected. Then the switching magnet changes the beams into various beam lines in the beam hall for different experimental facilities. The whole pelletron and beam hall safety is fully computer controlled with all the safety mechanisms.

The acceleration process involves two intermediate steps as described above. In the first step a singly charged negative ion will be accelerated in the field of terminal voltage ( $V$ ) and will attain an energy  $V$  ( $=\text{charge state} \times V$ ). Then if the particle attains a charge state  $q$  after passing through the stripper foil, it will be accelerated once again to energy  $qV$  under the same terminal potential. Hence in total the particle attains an energy of  $(1+q)V$ . Hence terminal potential is setup based on the required beam energy and available charge states. In general most probable (and most abundant) charge state is chosen so as to have stable beam. Beam current depends on the nature of the ion species charge state, energy, stripper foil and other beam tuning parameters. Gas stripper will provide a stable current. Required current can be obtained through proper beam tuning process.

Material science beam line is used for carrying out Swift Heavy Ion (SHI) based materials research. Several users from different universities work in the area of materials characterization and engineering with SHI at this facility. Fig. 2.3 shows a schematic diagram of the beam line and associated facilities. There are three experimental chambers on this beam line namely High Vacuum (HV) chamber, Ultra High Vacuum (UHV)



chamber and Goniometer (GM) Chamber. All the irradiation reported in this work is carried out in the HV chamber.

Fig 2.3 Schematic diagram of the material science beam line

### 2.2.2 Er Implantation and annealing

A series of samples consisting of GaN films on Al<sub>2</sub>O<sub>3</sub> substrate have been doped with Er ions through the ion implantation technique, followed by post-implantation annealing. Implantation was carried out at INFN-INFM ion implantation laboratory of INFN-Legnaro National Laboratories, Italy and annealing has been carried out at Department of Physics, University of Padova, Padova, Italy. Er implantations dose and annealing temperature were varied systematically in these experiments. We have prepared three different sets of ErGaN samples containing different doses of Er ions and annealing temperature as follows.

- (i) *ErGaN1*: implantation with  $1 \times 10^{14} \text{Er}^+/\text{cm}^2$  at 190 KeV; 1h annealing in  $\text{N}_2$  atmosphere at 800°C, 950°C and 1100°C;
- (ii) *ErGaN5*: implantation with  $5 \times 10^{14} \text{Er}^+/\text{cm}^2$  at 190 KeV; 1h annealing in  $\text{N}_2$  atmosphere at 800°C, 950°C and 1100°C;
- (iii) *ErGaN10*: implantation with  $1 \times 10^{15} \text{Er}^+/\text{cm}^2$  at 190 KeV; 1h annealing in  $\text{N}_2$  atmosphere at 800°C and 1100°C.

## 2.3 Characterization techniques

RBS/Channeling measurements on GaN in the third chapter are carried out at the Centre for Irradiation of Materials (CIM), Alabama A&M University, Alabama, USA. The energy dependent RBS/C studies used He ions from 2 MeV to 5 MeV in steps of 0.5 MeV. HRXRD measurements have been recorded at Solid State Physics Laboratory, New Delhi using Philips Xpert MRD system with a  $\text{Cu K}\alpha$  radiation set in point focus mode. This system has a channel cut, four crystal Ge (022) (Bartels-type) monochromator for  $\text{Cu K}\alpha_1$  X-ray beam. AFM (SPA400 of SII Inc, Japan) and optical transmission (JASCO V570 UV-VIS-NIR spectrophotometer) studies were carried out in house. In the chapter 4, RBS/C measurements carried out at IGCAR, Kalpakkam, have been reported. We have carried out channeling angular scans and energy dependence of dechannelling on  $\langle 1-213 \rangle$  (off normal axis) axis. Energy dependence has been carried out in the range 2.3 to 3.8 MeV by varying in step size of 0.3 MeV. Reciprocal space map on  $\langle 0002 \rangle$  was measured at Padova using Philips Xpert MRD in triple axis configuration. In this work we have used the in house facility of SPA400 of SII Inc AFM. Photo Luminescence studies in Chapter 5 has been carried out at Department of Physics, University of Padova and the RBS/Channeling lattice site location studies has been carried out at IIT, Kanpur, India. Channeling angular scans are measured on the  $\langle 0001 \rangle$  and  $\langle 10-11 \rangle$  axis. Details of the analysis carried out using different experiments are discussed following sections.

### 2.3.1 RBS/Channeling

RBS is a quantitative and nondestructive method for depth profiling and compositional analysis of materials. It is based on scattering of charged particles (normally He ions) in the central force field of target atoms. A collimated beam of mono energetic ions are



accelerated and bombarded on the sample, which is mounted on a 3 axis goniometer. General schematic diagram of the RBS/C set up is shown in the Fig 2.4. A fraction of ions will backscatter from the samples. The energy spectrum of these backscattered ions is analyzed by using a solid state barrier detector and data acquisition setup. When energetic ions are directed at a small angle  $\Psi$  to atomic axis or planes of crystal, these are steered by series of gentle collisions and are channeled into the regions between rows or planes of target atoms. Under the channeling conditions, the bombarding He ions will be backscattered from the first one or two surface monolayers of the material at the same rate as a non-aligned sample, but backscattering from the remaining atoms in the lattice will be drastically reduced since these atoms are shielded from the incident He ions by the atoms on the surface layers. The backscattering yield from a single crystal GaN sample which is aligned along the  $\langle 0001 \rangle$  axis, will be approximately 1.5% of the backscattering yield from a non-aligned spectrum. Fig 2.4 shows the typical RBS spectrum in aligned and random directions. By measuring the reduction in backscattering yield under channeling conditions, it is possible to quantitatively measure the crystal perfection of a sample [1].

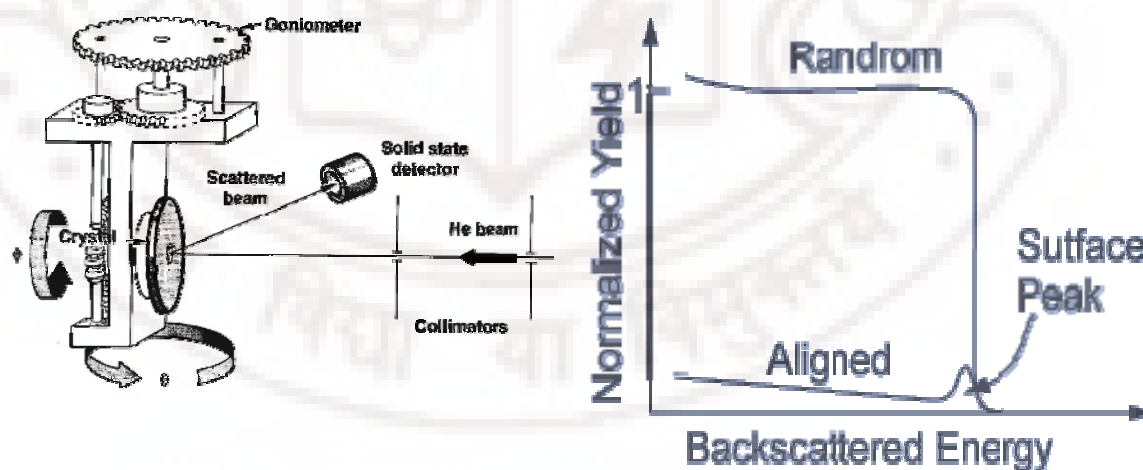


Fig 2.4 Schematic diagram of RBS/Channeling experimental setup and RBS/Channeling spectra

(i) Strain measurements on III Nitrides heterostructures

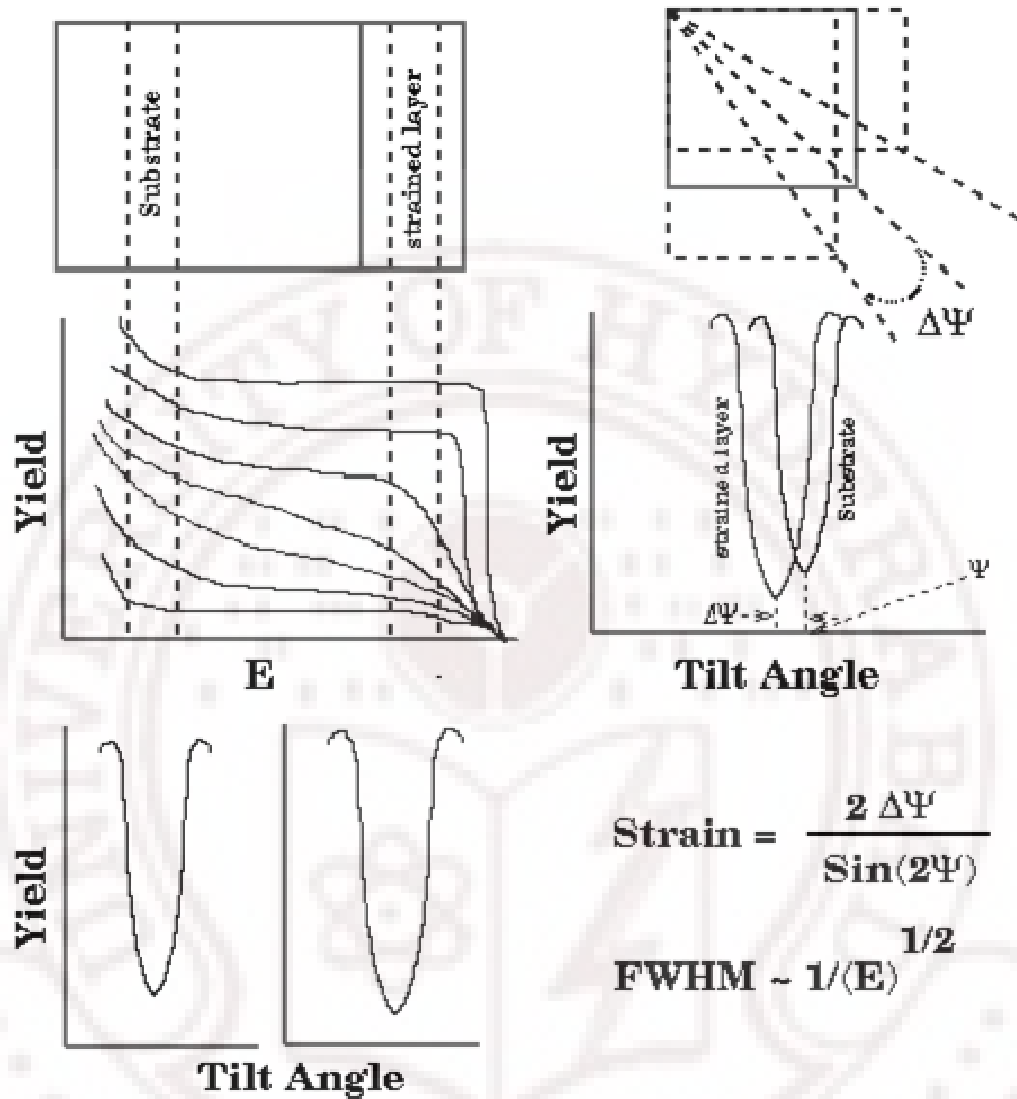


Fig 2.5 RBS/Channeling angular scans and strain measurement

The quality of epitaxial layers and the strain in such layers or in multilayers can be determined by channeling measurements. Generally these strains are estimated by measuring the channeling angular scans. The sample crystallographic axis or plane is aligned along the beam direction and the angular scans are measured by tilting the sample by  $2 \sim 3^\circ$  step by step, in small angular intervals of  $\theta \sim 0.1^\circ$ . The integrated yield of particular regions of interest, like epilayer and substrates are plotted as yield vs  $\theta$ . Typical angular scans are shown in the Fig 2.5.

RBS/C has been used extensively for the compositional and structural characterization of InGaN and AlGaIn [2-9]. RBS with channeling geometry gives information about both "In" and "Al" concentration and defects density in InGaN and AlGaIn samples. The influence of the "In" content on the accumulation of the structural damage in  $\text{In}_x\text{Ga}_{1-x}\text{N}$  films under ion bombardment has been studied using RBS/C [4]. Elastic strain in the  $\text{In}_{0.18}\text{Ga}_{0.82}\text{N}$  on the GaN substrate has been measured by this technique and indicates that the layer is much stiffer along the c-axis direction than in the a-axis direction [7]. Similar work has been done by other groups to measure the elastic strain in the  $\text{In}_{0.18}\text{Ga}_{0.82}\text{N}$  and  $\text{Al}_{0.28}\text{Ga}_{0.72}\text{N}$  [8]. RBS/C has been used to gain insight into compositional depth profile of 75 nm thick InGaIn in the growth direction [9]. RBS/C has also been used to study the evolution of the structural defects in  $\text{Al}_x\text{Ga}_{1-x}\text{N}$  films irradiated with KeV heavy ions [2].

## (ii) Defect characterization in III Nitrides

The dechannelling analysis is carried out by varying the incident energies and measures the aligned spectrum. The dechannelling parameter is calculated from the normalized back scattering yield of random and aligned spectrum using the formula [15],

$$DP = -\log \left\{ \frac{1 - \chi_D}{1 - \chi_V} \right\} \quad (2.1)$$

where  $DP = N_D \sigma_D$ ,  $N_D$  is the defect density and  $\sigma_D$  is the dechannelling cross section,  $\chi_D$  is the minimum yield in the defected crystal and  $\chi_V$  is the minimum yield of the defect free crystal at the same depth. This gives appropriate energy dependence for defect analysis.

The DP shows different energy dependences based on the kinds of defects present. The energy dependence of dechannelling cross section on the incident ion energy (i) for point defects it is  $E^{-1/2}$  (ii) for dislocation and dislocation loops, it is  $E^{1/2}$  as shown in fig 2.6 and (iii) for stacking faults it is  $E^0$  i.e. independent of energy.

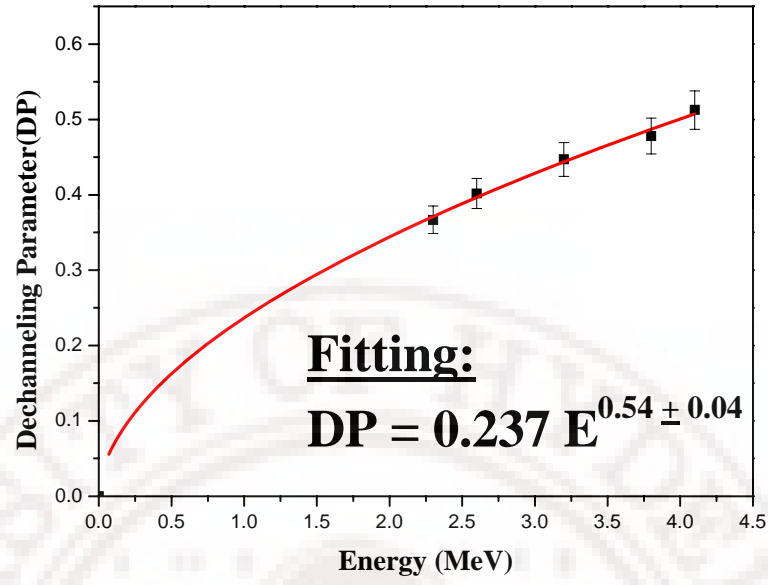


Fig 2.6 Energy dependence of dechannelling parameter (DP) for dislocations

For point defects,

$$\sigma_D = \frac{\pi Z_1^2 Z_2^2 e^4}{E \psi_c} \propto \frac{1}{\sqrt{E}} \quad (2.2)$$

For dislocations,

$$\sigma_D = K \sqrt{\frac{a b d E}{\alpha Z_1 Z_2 e^2}} \propto \sqrt{E} \quad (2.3)$$

$\alpha = \text{const depends on axial or planar and defect type}$   
 $a = \text{THOMAS – FERMI Screening Radius}$

For dislocation loops,

$$\sigma_D \propto \sqrt{E} \quad \text{for } R > \sigma_D$$

$$\sigma_D \text{ independent of } E \text{ for } R < \sigma_D \quad (2.4)$$

Where  $R$  is loop radius

For stacking faults,

$$\sigma_D \propto \chi_{\min} \quad (2.5)$$

$\chi_{\min} = \text{Minimum yield}$

Based on the model of Quere and Pathak et.al calculations [10,11], the effects of dislocations are modeled as the distortions in the axis or plane. The dechannelling of ions occurs when the channel distortion increases beyond a critical value. The parameter relating the channel distortion to the dislocation parameters is basically the radius of curvature R and is given by,

$$R = \frac{2 \pi^2 d_0}{b \cos \theta} \quad (2.6)$$

where,  $d_0$  is the distance of affected channel from the dislocation core, b is the burgers vector and  $\theta$  is the angle between channel axis and plane perpendicular to the dislocation line. In GaN's the common type of dislocations observed are: (i) Edge type with  $b = 1/3 \langle 11-20 \rangle$  (ii) Screw type with  $b = \langle 0001 \rangle$  (iii) Mixed type with  $b = 1/3 \langle 11-23 \rangle$ , with Dislocation line  $\langle 0001 \rangle$  & Slip Plane  $[0001]$  [12].

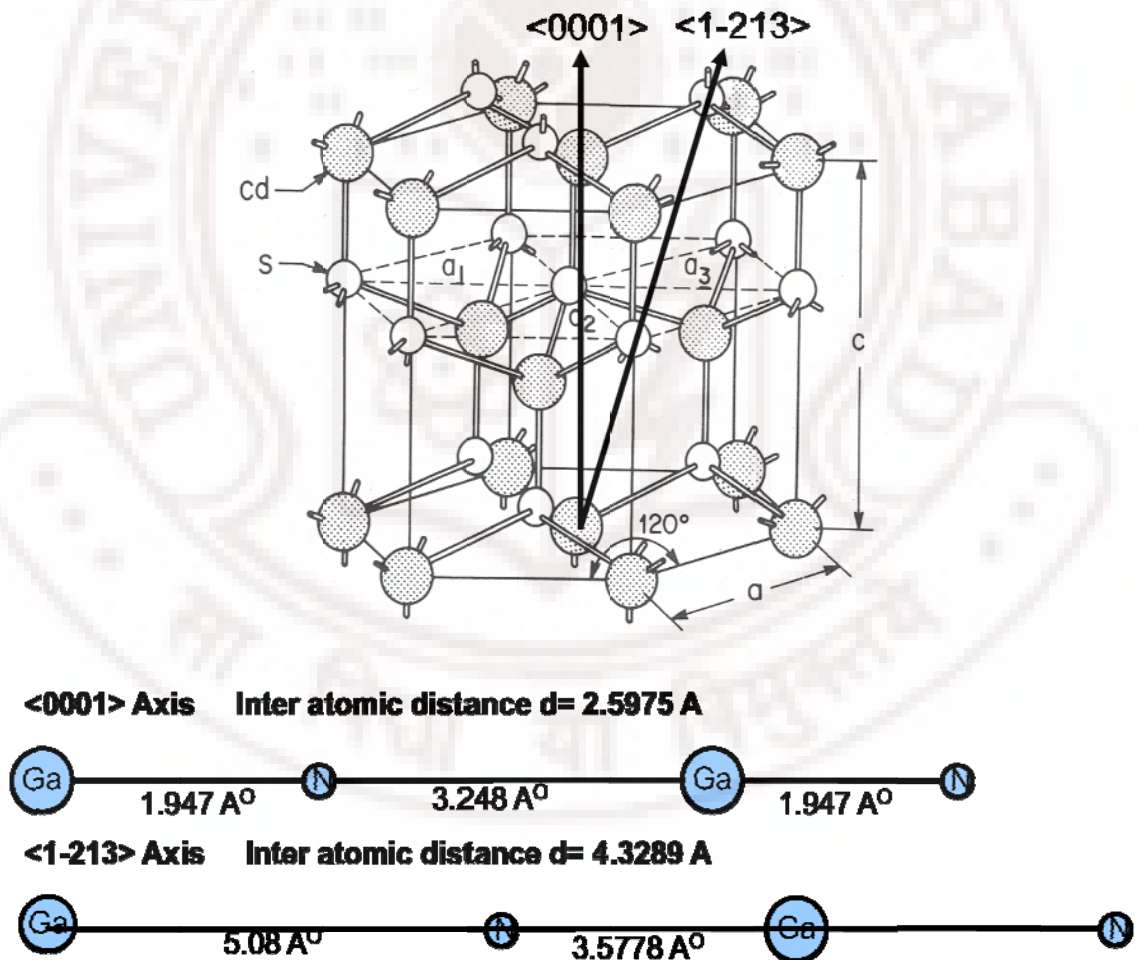


Fig 2.7. Normal  $\langle 0001 \rangle$  and off normal  $\langle 1-213 \rangle$  axis of GaNs and the inter atomic distance in respective axis

Fig 2.7 shows inter-atomic distance of Normal and off normal axes in GaN. Our calculation shows that, (i) Normal axis  $\langle 0001 \rangle$  is not affected by either Edge or Screw Dislocations but it is affected by Mixed dislocations. (ii) Off normal axis  $\langle 1213 \rangle$  is affected by all the kinds of dislocation i.e. Edge, Screw and Mixed.

To the best of our knowledge, only one dechannelling study of defects has been carried out by [13] on GaNs. On GaN samples,  $\chi_D$  was obtained from the experimental RBS spectra from the GaN layers (i.e. below the surface). In AlGaN heterostructures,  $\chi_D$  AlGaN layers are calculated by integrating the counts on the whole layer and GaN  $\chi_D$  is calculated from 100 nm just below the AlGaN layers.  $\chi_v$  was theoretically calculated to be  $\sim 3\%$ . DP Versus  $E^{0.5}$  plot with linear fit and its slope was used for the calculation of dislocation density,

$$N_D = \frac{\text{Slope} \times \sqrt{E}}{\sigma_D} \quad (2.7)$$

where  $\sigma_D$  is given by [1, 10],

$$\sigma_D = \left( \frac{bdaE}{\alpha Z_1 Z_2 e^2} \right)^{1/2} \quad (2.8)$$

$\alpha = 12.5, 4.5, 7.5$  for screw, edge, mixed dislocation respectively, the Thomas Fermi screening radius  $a = 0.1587 \text{ \AA}$ ,  $d$  is inter planar spacing.

### (iii) Lattice site location on III Nitrides

The commonly used application of channeling is to determine the lattice sites of impurity atoms in crystals. The impurity atoms present in the axial or planar channels are seen by the ion beams. As a result there will be an increase in the  $\chi_{\min}$  of the aligned spectra. By comparing the angular scans of different channels, the exact position of the atoms can be deduced. RBS/C method is direct way of determining the atomic position unlike the other techniques. Mossbauer and electron spin resonance, where the electronic information is analyzed to get the atomic positions. In GaN the lattice site studies are made by measuring the angular scans for two directions. The projections of the tetrahedral site projected on these two axial channels are shown in Fig 2.8.

Channeling angular scans show characteristic profiles when solute atoms settle at various positions into the channels [1]. Fig 2.9 shows angular scan of foreign atoms in crystal for different possible sites.

- (i) When the solute atoms are in substitutional sites, angular scans dip of solute and host atoms has same width.
- (ii) When the solute atom is slightly project into the channel from substitutional site, then angular scan of solute atom has smaller width than host atoms.
- (iii) When the solute atom is moved large into the channel from substitutional site, then angular scan of solute atom has double dip.
- (iv) When the solute atom is at center of the channel, then angular scan of solute atom has sharp peak.
- (v) For randomly located solute atom, a flat angular scan is observed.

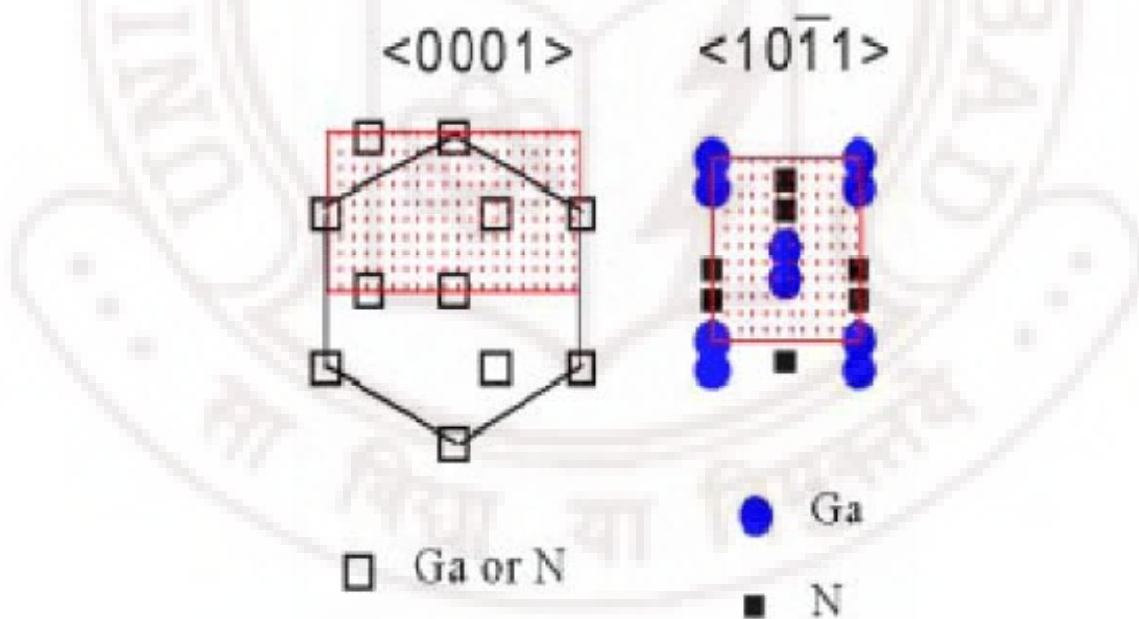


Fig 2.8 projection of Ga and N atoms as seen along  $\langle 0001 \rangle$  and  $\langle 10\bar{1}1 \rangle$  axis from the ref [14]



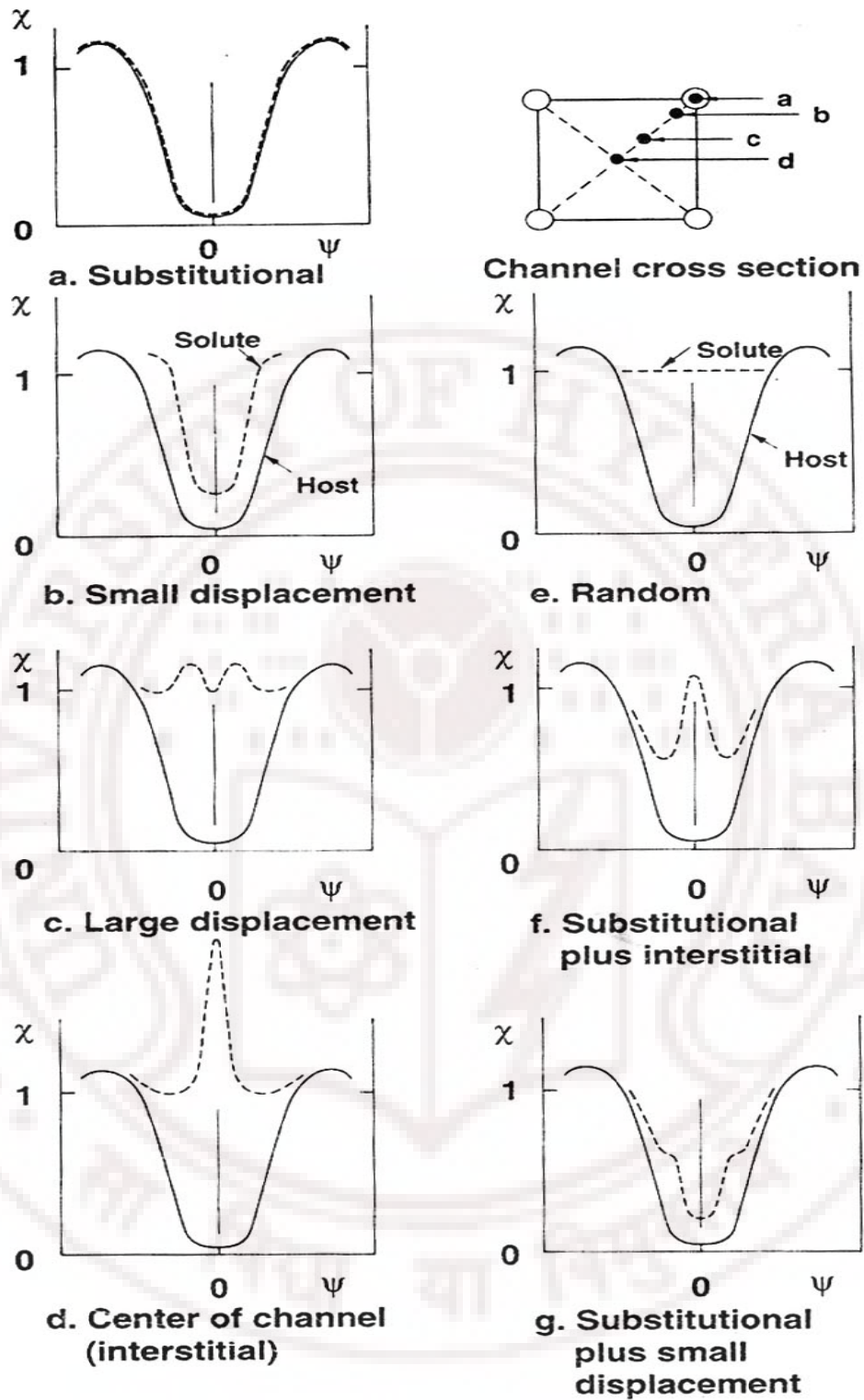


Fig 2.9 Channeling angular scans of foreign atom compared with host material with possible lattice sites



### 2.3.2 HRXRD

The High Resolution X-Ray Diffraction has become a powerful tool for nondestructive investigation of epitaxial layers. One gets information about the uniformity, thickness, strain, strain relaxation and defects present in the layer. Kinematic and dynamical diffraction theories are used to analyze the diffraction patterns from epilayers and heterostructures. The instrumentation has been developed with double and triple axis spectrometers equipped with multi crystal or channel cut monochromators. Fig 2.10 shows the schematic of the triple crystal diffractometer. Radial scans ( $\omega$ - $2\theta$  scan) and rocking curves ( $\omega$  scan) are commonly used in materials analysis. In radial scans, during the  $\theta$  scan (detector scan) the angle  $\omega$  between incident beam and the sample surface changes. Hence the scan runs radial from origin of the reciprocal space. In rocking curves, the detector is fixed and the sample is rotated i.e.  $\omega$  changes. The accuracy of the diffractometer is achieved through the high precision goniometer and the channel cut monochromators [15].

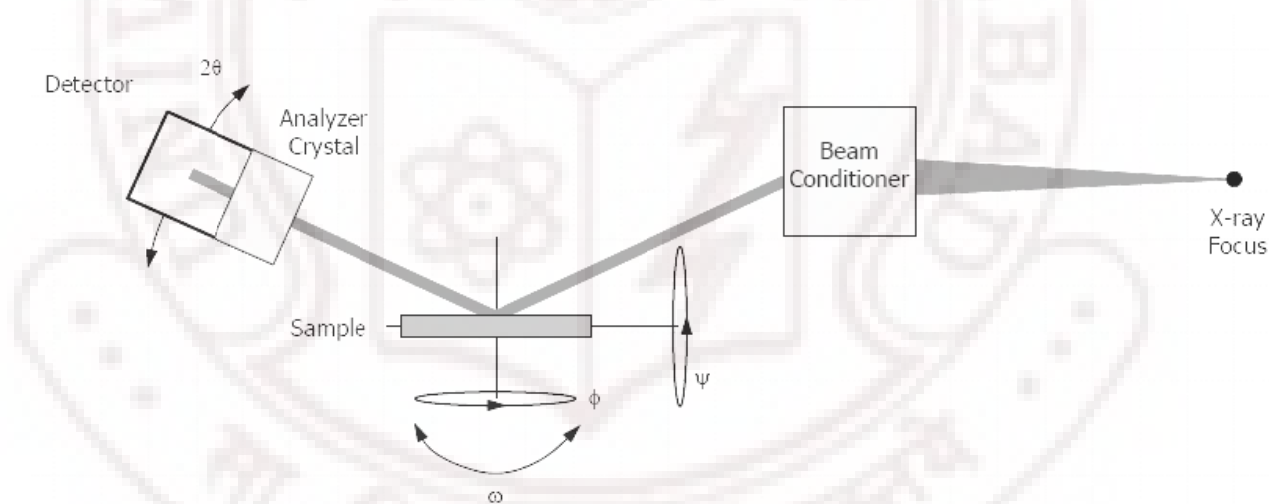


Fig 2.10 Schematic diagram of the HRXRD tripe axis diffractometer

High resolution X-Ray Diffraction (HRXRD) experiments have been carried out using a Philips Material Research Diffractometer (MRD). The  $\omega$ - $2\theta$  scan on (0002) direction are done on all the samples. The experimental radial scans are fitted using Pseudo-Voigt function for integral width (FWHM or  $\beta$ ) and Lorentzian weight fraction ( $f$ ). Lateral correlation and residual strain are calculated from FWHM and ' $f$ ' using the formulas given below. HRXRD studies are based on the diffraction peak widths. The peak broadening is mainly due to finite size of crystalline domains, non uniform strained

regions near to the lattice defects and contributions from instrumental and thermal broadening. The strain broadening of diffraction peak is proportional to the length of the scattering vector which results in Gaussian broadening, but the size effects have an exponential correlation function leading to Lorentzian broadening. The Peak shape analyses of x-ray diffraction are based on the separation of the Lorentzian and Gaussian broadening using Pseudo-Voigt function. By fitting this function one can get the integral width and Lorentzian weight function. [16-18]

$$I[fL(x) + (1 - f)G(x)] \quad (2.9)$$

where

$$L(x) = A \left[ \frac{2}{\pi} \frac{\beta}{(x - x_c)^2 + \beta^2} \right] \quad (2.10)$$

$$G(x) = \sqrt{4 \ln \frac{2}{\pi}} \frac{1}{\beta} e^{-\frac{(4 \ln 2)(x - x_c)^2}{\beta^2}}$$

$f$  = Lorentzian shape function

$\beta$  = Integral width

$x_c$  = Peak position

The instrumental and thermal effects have not been considered in the analysis because these are negligible when compared to the defect broadening in GaN. In general, threading dislocations (TDs) observed in GaN are formed due to the large lattice and thermal mismatch between GaN and Sapphire. In GaN samples there are three major type of threading dislocations observed with dislocation line vector along [0001] direction: (i) Pure edge, Burger vector  $b = 1/3[1120]$ , (ii) pure screw, Burger vector  $b = [0001]$ , and (iii) Mixed type Burger vector  $b = [1210]$ . The pure edge TDs give tilt while the pure screw TDs give twist to the grains as proposed in the mosaic model for x-ray analysis of the GaN. Extensive methods are available for quantitative measurement of screw and edge dislocations in GaN using HRXRD and described in detail elsewhere. [19,20]

Broadening in the rocking curves (angular scans or  $\omega$  scans) of the symmetry reflection are only due to the tilt and small correlation lengths parallel to the substrate surface.

Wafer bending or heterogeneous strain does not influence the peak broadening because of the small detector acceptance angle. Broadening in the radial scans ( $\omega$ - $2\theta$  scans) of the symmetry reflections are due to the small correlation length normal to the substrate surface and heterogeneous strain along c-axis. The effect of small correlation length and strain broadening can be separated by pseudo Voigt function fit using the different nature of broadening. Correlation length ( $L_{\perp}$ ) and perpendicular strain ( $\varepsilon_{\perp}$ ) can be calculated from the value of integral width (FWHM or  $\beta$ ) and Lorentzian function ( $f$ ) by using the formulas given below. [21]

$$L_{\perp} = \frac{(0.9\lambda)}{[\beta(0.017475 + 1.500484f - 0.534156f^2)\cos\theta]}$$

$$\varepsilon_{\perp} = \frac{\left[\beta\left[0.1846 + 0.872692(1 - 0.998497f)^{1/2} - 0.659603f + 0.445542f^2\right]\right]}{(4\tan\theta)} \quad (2.11)$$

$\beta$  = Integral width  
 $f$  = Lorentzian function  
 $\theta$  = Bragg Angle  
 $\lambda$  = Wavelength of x-ray

Here we have analyzed FWHM, peak shape in the log plots, Lorentzian and Gaussian broadening of x-ray peaks of our samples before and after irradiation.

### 2.3.3 Optical characterization

#### (i) Photoluminescence ( PL)

Photoluminescence (PL) investigation was carried out using an experimental set-up properly dedicated to the study of the NIR PL activity characterizing the Er ions. The excitations giving rise to PL are obtained by means of a cw Ar laser, whose pumping lines at 488nm (maximum laser power: 27mW) and at 476.5nm (maximum laser power: 7.5mW) provide rare earth photo-stimulation. These two lines are used to excite  $^4I_{15/2}$  ground state to  $^4F_{7/2}$  excited level of Er ion, under resonance and out-of-resonance conditions (i.e. pumping radiation not directly absorbed by the rare earth). The laser beam has a spot diameter of  $\sim 1$ mm and it is modulated by a mechanical chopper (typically at a frequency of 9Hz). Laser line selection is obtained by suitable interferential filters. A

system of lens and mirrors gives the possibility to focus the laser spot with a well-defined incidence angle on the surface sample, as well as to collect and bring the emitted radiation on the entrance slit of a ORIEL single-grating monochromator. This provides the spectral discrimination of the luminescence signal, which is detected by a photomultiplier tube. For these experiments, we have used a HAMAMATSU N<sub>2</sub>-cooled R5509-72, operating in the 1000-1650nm spectral range. PL emission is acquired with a lock-in amplifier, using the chopper frequency as reference, while data are stored in a PC by dedicated software. Schematic diagram of the PL setup used in this study is given in Fig 2.11.

Time-resolved PL analysis is carried out by switching off the pump beam and by detecting at a fixed wavelength, the PL intensity as a function of time with a transient digitizer (overall time resolution of ~5ms). PL excitation (PLE) measurements have been performed using a 150mW Xe lamp coupled to a monochromator, operating in the 250-800nm range, as pumping source, while the detecting system is the same as described above.

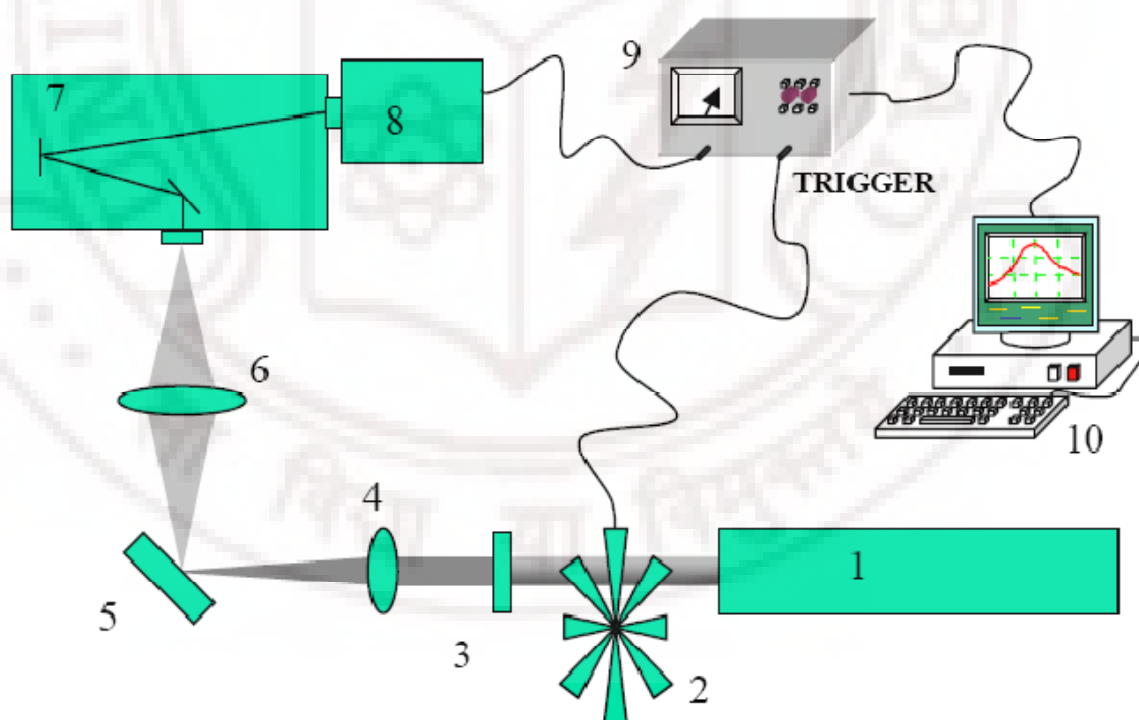


Fig 2.11. Diagram of the PL setup used in this study

## (ii) Optical Transmittance

The optical constants of the thin films were calculated using the envelope technique [22]. The spectral transmission characteristics in the wavelength range 190-1500 nm were measured using a JASCO V570 UV-VIS-NIR spectrophotometer.

Optical transmission and reflectance spectra are recorded from 190 nm to 2000 nm wavelength region, keeping standard samples in reference beam. Absorption coefficient is calculated using the relation.

$$\alpha = \frac{1}{d} \log \left[ \frac{1-R}{T} \right] \quad (2.12)$$

Band gaps are calculated from  $(\alpha E)^2$  vs E plot.

Refractive index is calculated using the relation:

$$n = \sqrt{N + \sqrt{N^2 - S^2}} \quad (2.13)$$

where

$$N = \frac{2 S (T_M - T_m)}{T_M T_m} + \frac{S^2 + 1}{2}$$

### 2.3.4 AFM

The microstructures of the deposited films were obtained using AFM. The AFM consists of a microscale cantilever with a sharp tip (probe) at its end that is used to scan the specimen surface. The cantilever is typically silicon or silicon nitride with a tip of radius of curvature of the order of nanometers. When the tip is brought into the proximity of a sample surface, forces between the tip and the sample lead to a deflection of the cantilever according to Hooke's law. Depending on the situation, forces that are measured in AFM include mechanical contact force, Van der Waals forces, capillary forces, chemical bonding, electrostatic forces, magnetic forces, solvation forces etc. Typically, the deflection is measured using a laser spot reflected from the top of the cantilever into an array of photodiodes. The AFM can be operated in a number of modes, depending on

the application. The primary modes of operation are static (contact) mode and dynamic mode.

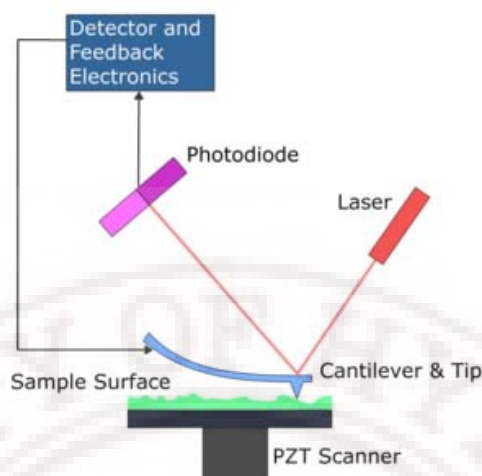


Fig 2.12. Schematic diagram of atomic force microscope.

In the static mode operation, the static tip deflection is used as a feedback signal. Because the measurement of a static signal is prone to noise and drift, low stiffness cantilevers are used to boost the deflection signal. However, close to the surface of the sample, attractive forces can be quite strong, causing the tip to 'snap-in' to the surface. Thus static mode AFM is almost always done in contact where the overall force is repulsive. Consequently, this technique is typically called 'contact mode'. In contact mode, the force between the tip and the surface is kept constant during the scanning by maintaining a constant deflection through feedback circuitry. In the dynamic mode, the cantilever is externally oscillated at or close to its resonance frequency. The oscillation amplitude, phase and resonance frequency are modified by tip-sample interaction forces. These changes in oscillation with respect to the external reference oscillation provide information about the sample's characteristics. Schemes for dynamic mode operation include frequency modulation and the more common amplitude modulation. In frequency modulation, changes in the oscillation frequency provide information about tip-sample interactions. Frequency can be measured with very high sensitivity and thus the frequency modulation mode allows for the use of very stiff cantilevers. In this work we have used the SPA400 of SII Inc, Japan AFM.

## References

- 1) Handbook of modern ion beam analysis, Ed J R Tesmer and Michel Nastasi, MRS, USA, (1995)
- 2) S O Kucheyev et. al, J. Appl. Phys. 93 (2003) 2972
- 3) S O Kucheyev et. al, J. Appl. Phys. 95 (2004) 3048
- 4) S O Kucheyev et. al, Appl. Phys. Lett. 80 (2002) 787
- 5) S O Kucheyev et. al, Appl. Phys. Lett. 79 (2001) 602
- 6) S O Kucheyev et. al, Phys Rev. B 62 (2000) 7510
- 7) S O Kucheyev et. al, J. Appl. Phys. 92 (2002) 3554
- 8) M F Wu et al, Appl. Phys. Lett. 74 (1999) 365
- 9) M F Wu et al Matt. Sci. Eng. B 75 (2000) 232
- 10) Y Quere, Phys. Stat. Sol. 30 (1968) 713
- 11) A P Pathak, Phys. Rev. B 15 (1977) 3309
- 12) Properties processing and applications of GaN and related semiconductors, Ed. J Hedgar et.al, IEE, INSPEC (1994)
- 13) W K Fong, et.al, Microelectronics Reliability 42 (2002) 1179
- 14) E Alves, et.al, Nucl. Instr. Methd. B 147 (1999) 383
- 15) Optical characterization of Epitaxial Semiconductor Layer, Ed G Bauer and W Richter, Springer, Germany (1996)
- 16) S R Lee, et.al, Appl. Phys. Lett. 86 (2005) 241904.
- 17) B. Heying, et.al, Appl. Phys. Lett. 68 (1996) 643.
- 18) V M Kaganer, et.al, Phys. Rev. B 72 (2005) 045423.
- 19) R Chierchia, et.al, Jour. Appl. Phys. 93 (2003) 8918.
- 20) V Srikant, et.al, Jour. Appl. Phys. 82 (1997) 4286.
- 21) T. Metzger, et.al, Phil. Magz. A 77 (1998) 1013
- 22) R Swanepoel, J. Phys. E: Sci Instrum. 16 (1983) 1214



## CHAPTER III

### Effects SHI on Bulk Epitaxial GaN layers

Recent research on ion beam processes in GaN has gained importance because of better understanding achieved about defects production and properties under ion bombardment. The performance of devices such as fast switches and detectors has been improved by subjecting the devices to controlled doses of particle irradiation [1, 2]. Recently there have been considerable developments in the understanding of ion–material interactions in general and ion–beam mixing in particular, especially using high energy ions. In a brief review, S.O.Kucheyev et.al, [3] summarized the effects of low energy ions on the defect processes in III Nitrides. For few MeV heavy ion bombardments strong dynamic annealing processes have been reported. As a result of dynamic annealing processes planar defects are created. Low energy ion beam generates an equal number of lattice interstitials and vacancies where interstitials agglomerate to form planar defects. While due to electronic energy loss processes for SHI, intense ultrafast excitations of valence electrons occur along ion tracks. The effects of SHI irradiation produced by 200 MeV Au ions were studied in S.O.Kucheyev et.al [4]. A better understanding of the physical mechanism of dynamic annealing by SHI in III-Nitrides is needed. It is important to understand the ion beam induced disordering behaviour in GaN. Previous reports [5] have indicated that GaN is very resistant to amorphization and there exists an intermediate stage of disorder saturation during the damage accumulation process. Jiang et.al, [6] reported amorphization process in Au ion irradiated GaN at 150–300 K. Kucheyev et.al, [4] also reported the lattice damage produced in GaN by 200 MeV Au ions. In spite of all these ion beam studies of GaN there are very limited number of systematic studies in the energy range  $\sim 100$  MeV.

Ion irradiation can make the material highly resistive under suitable conditions and hence, can be used for spatial electrical isolation. Electrical isolation of GaN generated by MeV light ion irradiation has been reported by several authors [7-11]. It has been shown that the sheet resistance is increased by more than 7 orders of magnitude as a result of ion irradiation. Defect complexes and anti-site-related defects are responsible for the electrical isolation. For such electrical isolation several necessary conditions need to be



satisfied. In particular, SHI irradiation is known to deposit large electronic energy density along the ion path within a very short time. According to the thermal spike model [12,13], during the passage of SHI, the kinetic energy of the electrons is transmitted to the lattice by electron-phonon interaction in a way sufficient enough to increase the local lattice temperature above the melting point of the material. The temperature increase is followed by a thermal quenching at an extremely high quenching rate. Hence, experiments are needed to reveal the response of each material to intense electronic excitation along SHI tracks. While the detailed physical processes following SHI bombardment of semiconductors in general are unclear, even less is known about the behavior of nitride semiconductors exposed to intense electronic excitations. It is interesting to consider whether intense electronic excitations can result in defect formation in GaN.

The aim of this study is to investigate the mechanism of ion beam induced defects, structural changes (at high energies) and hence changes in the optical properties of GaN. We apply ion beam techniques to improve the material quality, surface properties and reduce interface roughness to optimise the ion beam parameters for controlled modification. Specifically, this work addresses the problem of damage creation in GaN by subjecting the samples to highly energetic heavy ion bombardment. Effects of irradiation on the previously existing defects, strains, transformations of the defects due to the high energy deposition (and hence optical properties) are also studied.

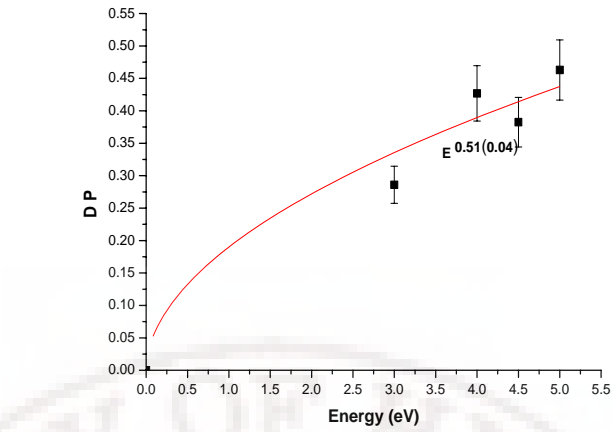
Samples studied are 2  $\mu\text{m}$  thick GaN layers grown on c-plane sapphire by MOCVD. Samples are irradiated with 150 MeV  $\text{Ag}^{12+}$  ions at a fluence of  $5 \times 10^{12}$  ions/ $\text{cm}^2$  using the 15 MV tandem accelerator facility at IUAC, New Delhi. These ions penetrate to depths of approximately 11.03  $\mu\text{m}$  and 11.13  $\mu\text{m}$  in GaN and Sapphire respectively, and lose energy of 24.79 keV/nm in GaN and 22 keV/nm in Sapphire through electronic interactions. Surface morphology of the samples is studied by contact mode AFM. HRXRD studies have been carried out at SSPL, New Delhi and RBS/C energy dependence spectra are measured at Alabama A&M University, USA. Details of the facilities and the measurements carried out have already been discussed in the Chapter 2.

### 3.1. RBS/ Channelling studies

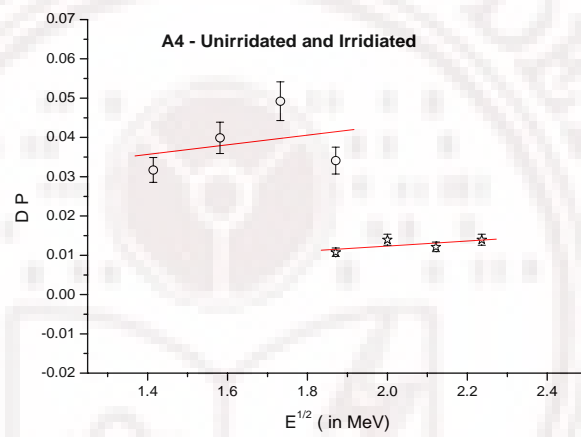
Energy dependence of dechannelling parameter for irradiated and unirradiated samples were carried out by RBS/Channelling. This gives qualitative and quantitative information about the defects present in the crystal. The backscattered yield was obtained using the detector mounted at a scattering angle of  $\sim 170^\circ$ . RBS/C experiments were carried out along  $\langle 0001 \rangle$  axis using incident energies between 2 and 5 MeV. The energy dependence of dechannelling parameter has been deduced from the normalized back scattering spectra. To the best of our knowledge, only one such study has been carried out earlier [14]. All our observed and calculated values for all the samples have been tabulated in Table 3.1. We notice that for  $\langle 0001 \rangle$  axis,  $\chi_{\min}$  for all the samples are higher than expected values by about 2~3 % [15-18]. This may be due to the higher concentration of complex defects, which are normally not seen in good quality GaN crystals. In these materials, threading screw and edge dislocations do not affect  $\langle 0001 \rangle$  axis. So one will get very good  $\chi_{\min}$  in  $\langle 0001 \rangle$  axis of GaN samples. As indicated in last chapter, one should carry out the experiments along the off normal axis  $\langle 1-213 \rangle$  to estimate the dislocation densities [19]. In our samples, off normal axis is heavily distorted by the dislocations and we did not get any channelling spectra for  $\langle 1-213 \rangle$ . RBS/Channelling Energy dependence has been carried out for  $\langle 0001 \rangle$  axis.

Table 3.1.  $\chi_{\min}$  and calculated defect density ( $N_D$ ) of the samples.

Sample	$\chi_{\min}$ (for 2.5 MeV $\text{He}^+$ )	$N_D$ in $\text{cm}^{-2}$
A6U	15.6%	$6.2 \times 10^{11}$
A6I	8.2%	-
A4U	6.4%	$2.4 \times 10^8$
A4I	10.6%	$5.2 \times 10^9$
RE48U	22.1%	$4.6 \times 10^{10}$
RE48I	36.4%	$6.1 \times 10^{11}$



(i)



(ii)

Fig 3.1. (i) Energy dependence of as grown A6 (ii) Calculation of dislocation density for A4 sample from RBS/C data.

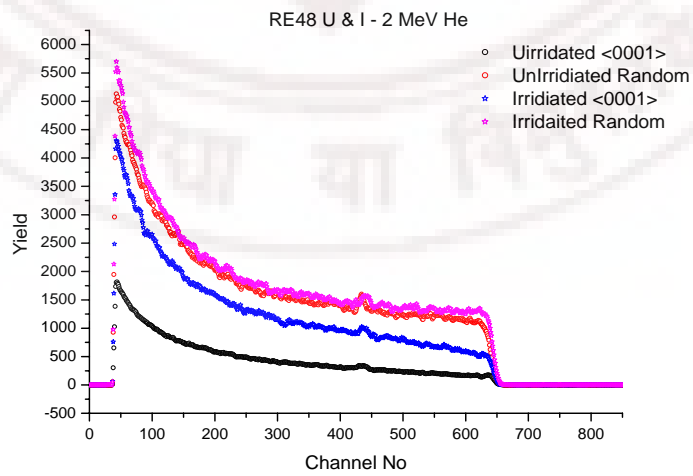


Fig 3.2. RBS/Channelling Spectrum of RE48 asgrown and irradiated.

In the as grown A4 samples,  $\chi_{\min}$  is 6.4% which is very high compared to the reported values of 1.5 ~3 %. This indicates that <0001> axis itself is severely distorted by the defects. As discussed earlier, pure threading screw and edge dislocations do not affect the <0001> axis, so mixed dislocations are present in the sample. Incident ion energy dependence of dechannelling is  $E^{0.5}$  type, which corresponds to dislocations and the calculated dislocation density is found to be  $2.4 \times 10^8 \text{ cm}^{-2}$ . These results are illustrated in Fig 3.1

After irradiation more dislocations have been formed, which is evident from the increase in  $\chi_{\min}$  and dislocation density to  $5.2 \times 10^9 \text{ cm}^{-2}$ . This may be due the epitaxial reconstruction of the low temperature buffer layer by the swift heavy ion irradiation. Generally these buffer layers are grown as 3D layer to reduce the mismatch strain between GaN and Sapphire. When these layers are reconstructed epitaxially mismatch strain is increased and the dislocation density also increases. After irradiation, scatter in the data points in DP vs.  $E^{1/2}$  graph increases which may be due to creation of some point defects by these swift heavy ions.

In unirradiated A6,  $\chi_{\min}$  for 2.5 MeV  $\text{He}^+$  is 15.6 %. This shows that the original samples are of very poor quality. Calculated defect density is found to be  $6.2 \times 10^{11} \text{ cm}^{-2}$ . After irradiation  $\chi_{\min}$  is decreased to 8.2 %, but the energy dependence of dechannelling parameter shows  $E^2$  dependence and the data point are scattered heavily. From the surface morphology of the irradiated A6 one can see large holes (see Fig 3.6), which seem to have been formed due to clustering of the dislocations near the surface. Incident ions initially start steering into these holes and guided to the dislocation core. So initially there is reduction in the  $\chi_{\min}$  and doesn't have any meaningful energy dependence.

In RE48 sample,  $\chi_{\min}$  is 22.1%. This large value may be due to very large dislocation density and low temperature grown AlN cap layer which is basically a 3D textured growth layer. Random and aligned RBS spectra of as-grown and irradiated RE48 samples are shown in Fig 3.2. Defect density calculated from the dechannelling analysis is  $4.6 \times 10^{10} \text{ cm}^{-2}$ . After Irradiation  $\chi_{\min}$  increases to 36.4% and defect density increases further to about  $6.1 \times 10^{11} \text{ cm}^{-2}$ .

### 3.2. High Resolution X-Ray Diffraction

The experimental radial scans are fitted using Pseudo-Voigt function for integral width (FWHM or  $\beta$ ) and Lorentzian weight fraction ( $f$ ). Lateral correlation and residual strain are calculated from FWHM and ' $f$ ' using the formulas given below. HRXRD studies are based on the diffraction peak widths. The peak broadening is mainly due to finite size of crystalline domains, non uniform strained regions near to the lattice defects and contributions from instrumental and thermal broadening. The strain broadening of diffraction peak is proportional to the length of the scattering vector which results in Gaussian broadening. But the size effects have an exponential correlation function leading to Lorentzian broadening. The Peak shape analyses of x-ray diffraction are based on the separation of the Lorentzian and Gaussian broadening using Pseudo-Voigt function.

In GaNs, broadening in the rocking curves (angular scans or  $\omega$  scans) of the symmetry reflection are only due to the tilt and small correlation lengths parallel to the substrate surface. Wafer bending or heterogeneous strain does not influence the peak broadening because of the small detector acceptance angle. Broadening in the radial scans ( $\omega$ - $2\theta$  scans) of the symmetry reflections are due to the small correlation length normal to the substrate surface and heterogeneous strain along c-axis. The effect of small correlation length and strain broadening can be separated by pseudo Voigt function fit using the different nature of broadening. Correlation length ( $L_{\perp}$ ) and perpendicular strain ( $\epsilon_{\perp}$ ) can be calculated from the value of integral width (FWHM or  $\beta$ ) and Lorentzian function ( $f$ ) [20-25].

All the radial scans are fitted (Fig 3.3) and analysed using methods described earlier in the experimental section and the extracted values are tabulated in tables 3.2 and 3.3. The integral widths of as grown samples show that RE48U have better crystalline quality than other samples. A4U and A6U are having nearly equal integral widths i.e. samples of same crystalline quality. In all the as grown samples both Lorentzian and Gaussian broadenings are observed, which shows that both kinds of defects are present in these samples i.e., dislocations as well as point defects. The layer quality along the perpendicular direction to the substrate surface is limited by mixed dislocations which causes Lorentzian

broadening. The Lorentzian weight function of RE48U, A6U and A4U are 0.52, 0.48 and 0.39 respectively. Broadening due to Lorentzian type is more in RE48U (~52%) when compared to A6U (~48%) and A4U (~ 39 %). The as grown sample RE48U is having more dislocations than point defects. But the samples A6U and A4U have more point defects than dislocations.

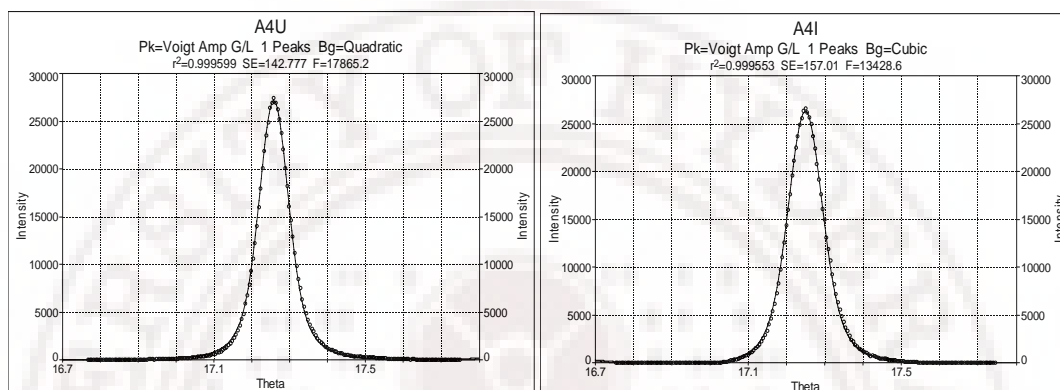


**Fig 3.3. Pseudo-Voigt function fit for the sample as grown and Irradiated A4**

**Table 3.2. Parameters extracted from Pseudo Voigt Function fitting.**

Sample	FWHM ( $\beta$ )	f (weight Lorentzian function)
A6U	0.0968	0.48
A6I	0.1218	1.00
A4U	0.0950	0.39
A4I	0.1100	0.44
RE48U	0.0782	0.52
RE48I	0.0892	0.73

**Table 3.3. Lateral correlation and residual strain.**

Sample	Lateral correlation length $L_{\perp}$ nm	Strain perpendicular $\varepsilon_{\perp}$
A6U	134	—
A6I	663	—
A4U	162	$9.09 \times 10^{-4}$
A4I	125	$9.75 \times 10^{-4}$
RE48U	156	$6.13 \times 10^{-4}$
RE48I	107	$4.8 \times 10^{-4}$

After irradiation the Lorentzian shape function increases from 0.51 to 0.71 in RE48I. However, irradiation did not increase the Gaussian broadening much and the peak was almost Lorentzian in nature. This shows that point defects like N vacancy are either not created or these are very less in this sample. A decrease in the lateral correlation length was observed in irradiated RE48I indicating the poor layer quality along the (0001) direction. This may be due to the high energies deposited by the ion (during irradiation) to electronic subsystem in small regions of the lattice. This energy is enough for the dissociation and movement of the dislocations, which leads to columnar and mosaic structures and loss of vertical correlation [24]. In the log plot (Fig 3.4) a small shoulder peak corresponding to the local strained regions can be observed in both irradiated and unirradiated samples. After irradiation there are no changes in the peak shape i.e. no extra shoulder peak corresponding to the locally strained regions (like N- vacancies) are observed. This may be because of the AlN cap layer that prevents any Nitrogen loss.

The Lorentzian factor increases after irradiation in A4I and the peak broadening consists of both Lorentzian and Gaussian type. As stated earlier, the reason for the Lorentzian broadening may be due to poor layer quality along the (0001) direction while the Gaussian broadening results from point defects, specially due to N vacancies created by



ions . In the log plot, Lorentzian type tail is observed in the unirradiated A4U. Irradiation induces a small shoulder peak (Fig 3.4), which confirms the presence of the Ga rich regions after irradiation in A4I.

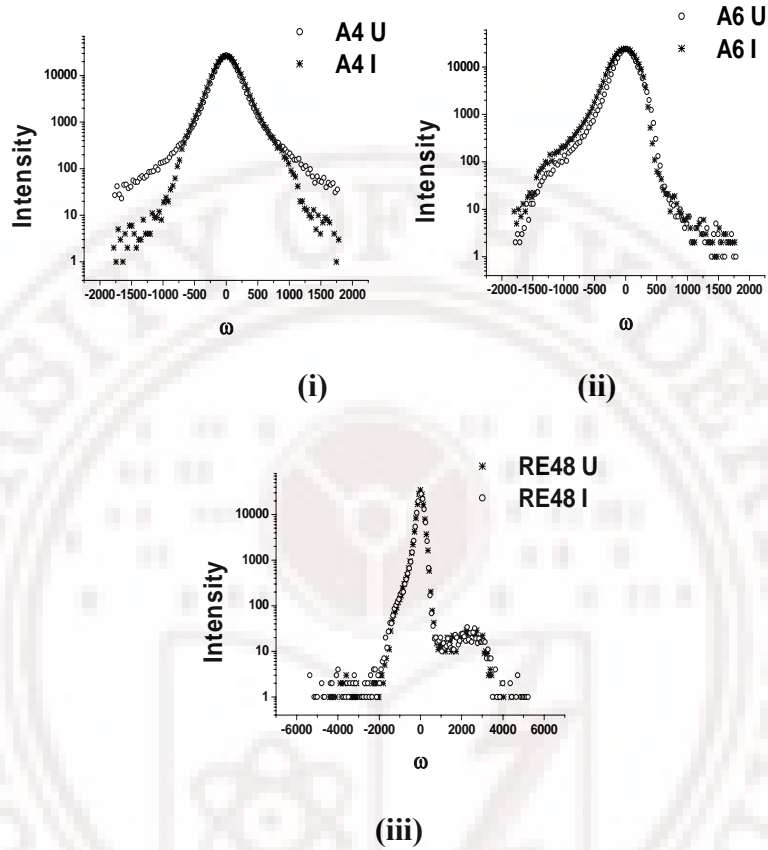


**Fig 3.4. Log plot of 0002  $\omega$ -2 $\theta$  scan of as grown and irradiated samples (i) A4 U&I (ii) A6 U&I (iii) RE48 U&I.**

The Pseudo-Voigt function does not yield a good fit because of peak asymmetry in the as grown and irradiated A6 samples. In the unirradiated sample (A6U) one side of the peak has Lorentzian and other side tail falls off as Gaussian. In the log plot a small shoulder peak corresponding to the point defects are observed in the unirradiated sample (A6U), which increases after irradiation (A6I) showing that irradiation increased point defects in A6.

FWHM of all the samples increased after irradiation which shows that the samples are damaged after irradiation. In the sample RE48, increase in FWHM is less compared to the other two samples. In A4, increase in FWHM is less when compared to that of A6, indicating that the damage caused in A6 is more compared to all other samples.



**Table 3.6. RMS roughness (nm) measured from AFM**

<b>Sample (details)</b>	<b>A4</b>		<b>A6</b>		<b>RE48</b>	
	<b>2<math>\mu</math>m GaN/Sapphire</b>		<b>2<math>\mu</math>m GaN/Sapphire</b>		<b>Thin AlN/2<math>\mu</math>m GaN/Sapphire</b>	
	<b>U</b>	<b>I</b>	<b>U</b>	<b>I</b>	<b>U</b>	<b>I</b>
<b>RMS roughness</b>	<b>3.328 nm</b>	<b>2.171 nm</b>	<b>2.28 nm</b>	<b>7.014 nm</b>	<b>2.861 nm</b>	<b>4.197 nm</b>

### 3.3. Atomic Force Microscopy

Figs 3.5-3.8 show AFM images of as grown and Irradiated A4, A6 and RE48 samples respectively. Measured RMS roughness values are given in table 3.6. As grown samples show similar morphology having larger hillock sizes varying from 200 to 1700 nm. These are commonly observed in GaN films. Ending of threading screw dislocation normally results in this kind of morphology [26-28]. It has been demonstrated using ab-initio theory that these dislocations will have very high line energy. As a result of energy minimisation, material from the core of dislocation will move far away from the strained region i.e. to the surface. The same is predicted from equilibrium theories also, but the size of hillocks predicted by classical equilibrium theories and experiments do not match [27]. After irradiation qualitative as well as quantitative changes are observed.

In our samples, as a result of irradiation, both hillocks and deep holes are observed in A4. But in A6 there are no hillocks, only deep holes are formed, and their sizes are of the order of hillock sizes present in as grown samples. We have not observed any qualitative changes before and after irradiation in RE48 as in A4 and A6; but the sizes of the pinned steps have reduced after irradiation.

A4 and A6 samples show different morphologies, showing hillocks and deep holes after irradiation. Fig 3.7 shows that after irradiation these holes clustered under one big hole of size of about 700 nm. Generally the size of these deep holes ranges from few nm to few hundred nm for GaN depending on the growth conditions. It has been reported using TEM, that these V defects and deep holes are associated with inversion domains, dislocation half loops, impurities and threading edge dislocations [26, 29-32].

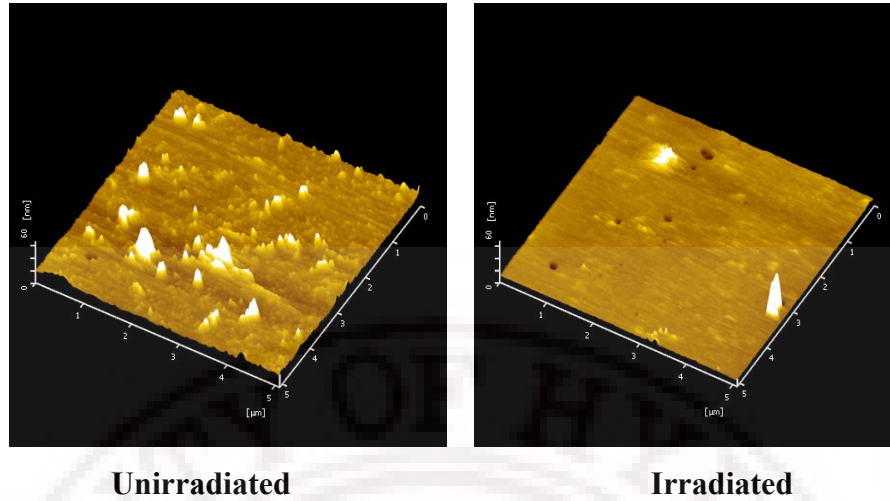


**Fig 3.5. 5 x 5  $\mu\text{m}$  AFM scans of surface morphology of the A4 U & I.**

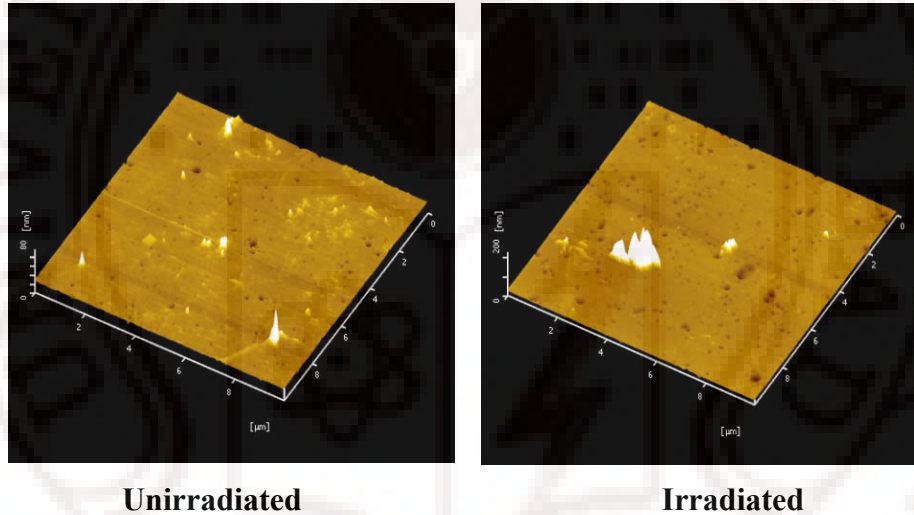
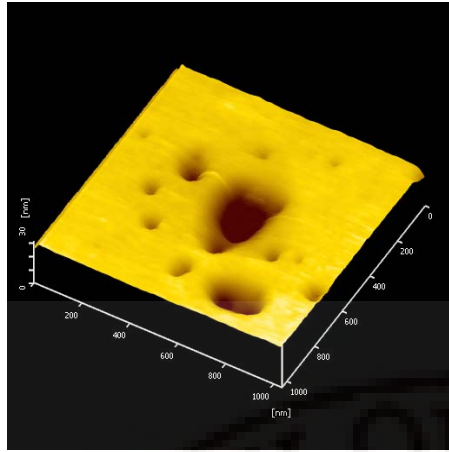
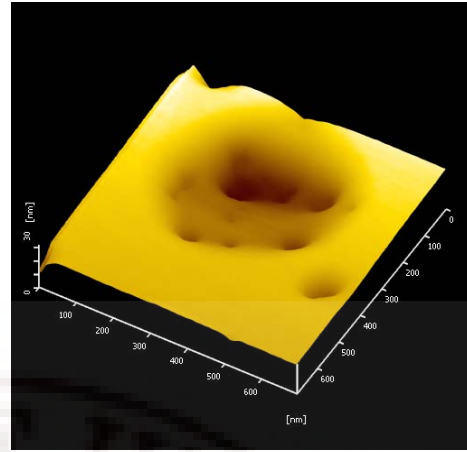


**Fig 3.6. 10 x 10  $\mu\text{m}$  AFM scans of surface morphology of the A6 U & I.**

It has been demonstrated that for moving the dislocations, very high energy is needed [33]. TRIM calculations show that 150 MeV Ag ion deposits about  $\sim 25$  keV/nm in a small radius. Energy loss of the ions used for irradiation may provide high energy for the dislocation movements. In this process, if these dislocations cross impurities or point defects they break into partial dislocations and the energy of the dislocation relaxes then to form dislocation half loops and may result in the kind of surface morphology observed in our experiments. In RE48, it has thin AlN layer on the top of the GaN. Strain energy in the AlN/GaN interface prevents any change in the surface morphology.

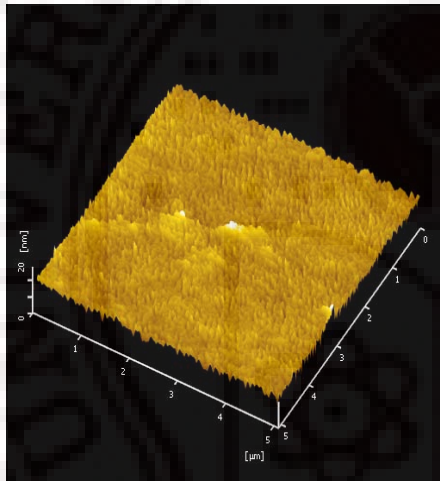


**Unirradiated ( 1 $\mu$ m Scan)**

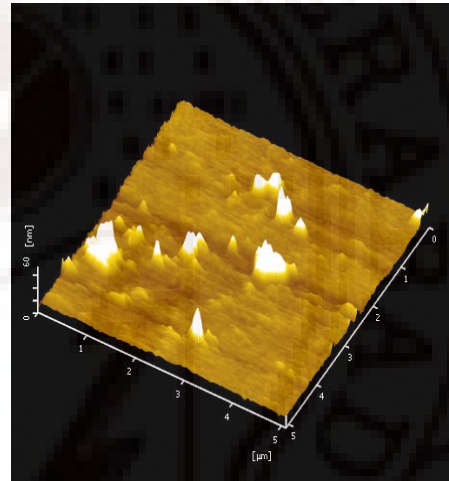


**Irradiated ( 700 nm scan )**

**Fig 3.7. Surface morphology of the A6 U & I from AFM scans.**



**Unirradiated**



**Irradiated**

**Fig 3.8. 5 x 5  $\mu$ m AFM scans of surface morphology of the RE48 U & I.**

### 3.4. Optical Studies

The spectral transmittance curves (Fig 3.9) show sharp absorption edge for as grown samples. This is generally observed in MOCVD grown GaN in spite of high defect density [34-37]. GaN has very high absorption coefficient of the order of  $10^5 \text{ cm}^{-1}$  and hence transmittance is very less [38-41]. Here our sapphire substrate is single side polished so we have only 6-8 % transmittance and the spectra is normalised to the blank sapphire spectra.

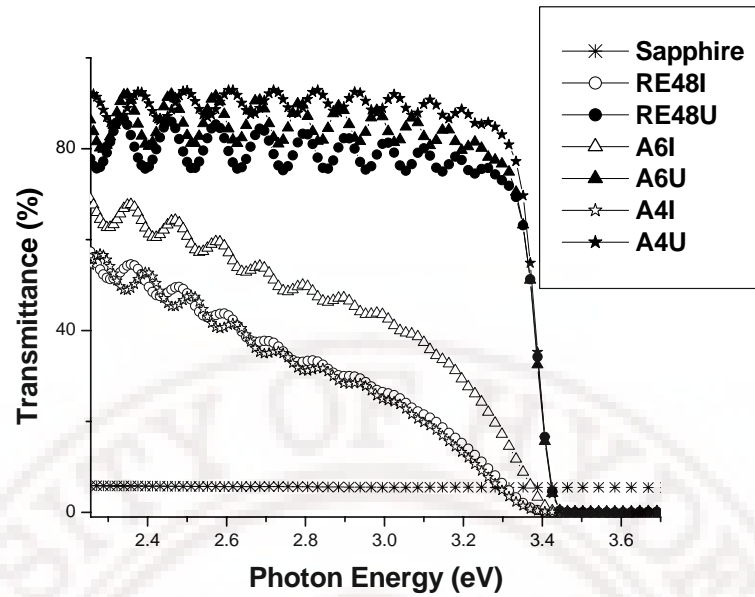


**Fig 3.9. Spectral transmission curves of the as grown and irradiated samples**

After irradiation, band edge absorption increases exponentially instead of sharp step like increase. This kind of behaviour is observed in highly defected samples or at high doping level. From  $(\alpha E)^2$  vs.  $h\nu$  plots (Fig 3.10) band edges are calculated. In the as grown samples measured band gaps are 3.39, 3.39 and 3.38 eV for RE48U, A4U and A6U respectively. After irradiation the calculated band gap values are decreased to 3.34, 3.24 and 3.29 eV for RE48I, A4I and A6I respectively.

This kind of broadening of near band edge absorption may be due to irradiation induced point defects and locally strained regions or relaxed into extended defects [42-44]. Effect of irradiation is relaxation of high energy dislocations, (like threading screw dislocations) leading to formation of partial dislocations and dislocation half loops at the near surface or near interface regions. As a consequence the energy gap of the excitons associated in the locally strained regions may reduce. This kind of defects relaxation is observed in AFM surface morphology and also results in the increase in the Lorentzian weight function of the  $\omega$ -2 $\theta$  scan. The colour change in the samples shows the formation of the point defects and this is also confirmed by the small shoulder peaks in the HRXRD scans. Marques et.al [45] reported that, Ag implantation on Sapphire forms F and F<sup>+</sup> centres at 4.8 eV and 2.4 eV respectively, which resulted in broad absorption peak in the region 350 - 500 nm. They also observed colour change from transparent to goldish yellow, which

has also been seen in our samples. Canut et al. [46] studied the effects of electronic energy loss on sapphire and observed that F centres are formed in sapphire with absorption at 4.8 and 5.4 eV. We confirmed this possibility by irradiating the blank sapphire samples by same 150 MeV Ag ions at the fluence of  $5 \times 10^{12}$  ion/cm<sup>2</sup>. In the current study, however no colour changes in the sapphire were observed.

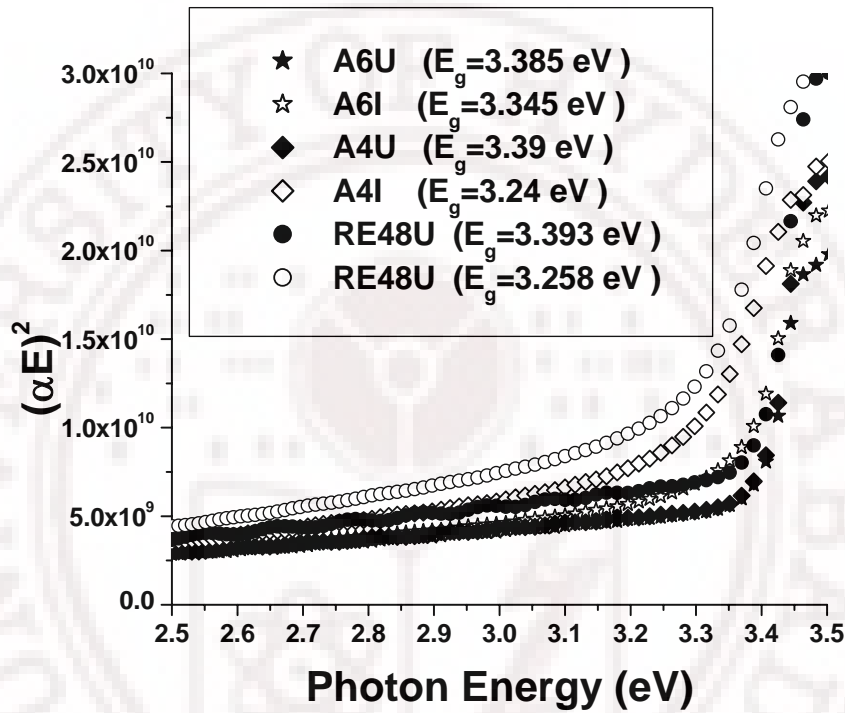


**Fig 3.10. Band gap values derived from Optical transmission data for as grown and irradiated samples.**

### 3.5. Conclusions

RBS/C energy dependence analysis has been carried out along  $\langle 0001 \rangle$  axis on all the samples (A4, A6, RE48 U & I) and defect densities were calculated at the depth of about 100 nm from the surface. The calculated dislocation densities are high as expected in GaN samples, which is evident from the high  $\chi_{\min}$  values. In GaN samples with pure edge and screw dislocations one should carry out energy dependence analysis in the off normal axis  $\langle 1-213 \rangle$  to get the information as these defects do not affect  $\langle 0001 \rangle$  axis. But in the samples with mixed dislocations and complex defects channelling in  $\langle 0001 \rangle$  axis itself

gives the information about the defects. In the sample A6I, we did not observe any meaningful energy dependence. This may be due to the random scattering from the dislocation core. In the other irradiated samples A4I and RE48I, there is a large scatter of the data points in DP vs.  $E^{1/2}$  curve. This may be due the point defect created by the swift heavy ions.

SHI gives enough energy for the material to reconstruct at the interface i.e. low temperature buffer layer/Sapphire interface. As a result of this, more strain is induced and more dislocations are formed in the GaN layer. This increase in dislocation densities after irradiation has been confirmed by the HRXRD results, where strain was found to increase after irradiation. Damage creation in GaN by Swift Heavy Ions (SHI) is very complex process. The high energy deposited by the ion to the lattice, results in two kinds of damage creation in GaN. One is N loss and Ga rich regions, as confirmed by the Gaussian broadening of X-Ray peak widths and small shoulder peaks. Broadening of the optical band-edge absorption also confirms this. AlN cap layer can be used to reduce the N loss due to irradiation. The second damage is induction of dislocations due to the reconstruction of LT GaN buffer layer. Also the initial defect configuration in the pristine samples plays a major role in the damage creation by swift heavy ion irradiation.

## References

1. S J Pearton, Mater. Sci. Res. 4 (1990) 313.
2. S C Binari, H B Dietrich, G Kelner, L B Rowland, K Doverspike and D K Wickenden, J. Appl. Phys. 78 (2005) 3008.
3. S O Kucheyev, et.al, Vacuum 73 (2004) 93.
4. S O Kucheyev, et.al, J. Appl. Phys. 95 (2004) 5360.
5. S O Kucheyev, J S Williams and S J Pearton, Mat. Sci.Eng. R 33 (2001) 51.
6. W Jiang, W J Weber, M Wang and K Sun, Nucl. Inst. Meth. Phys. Res. B 218 (2004) 427.
7. H Boundinov, et.al, Appl. Phys. Lett. 78 (2001) 943.
8. S O Kucheyev, et.al, J. Appl. Phys. 91 (2002) 4117.
9. S O Kucheyev, et.al, J. Appl. Phys. 91 (2002) 3940.
10. A I Titov, et.al, J. Appl. Phys. 92 (2002) 5740.
11. S O Kucheyev, et.al, Appl. Phys. Lett. 81 (2002) 3350.



12. G Szenes, Z E Horvath, B Pecz, F Paszti, and L Toth, Phys. Rev. B 65, (2002) 045 206.
13. M Toulemonde, C Dufour, and E Paumier, Phys. Rev. B 46, 14 362 (1992).
14. W K Fong, C F Zhu, B H Leung, C Surya, B Sundaravel, E Z Luo, J B Xu, I H Wilson, Microelectronics Reliability 42 (2002) 1179.
15. Ding Zhi-Bo, et.al. Chin. Phys. Lett. 24 (2007) 831.
16. Wang Huan, et.al. Chin. Phys. Lett. 23 (2006) 2510.
17. M F Wu, et.al Appl. Phys. Lett. 74 (1999) 365.
18. M F Wu, et.al. J. Vac. Sci. Technol. B 12 (1999) 1502.
19. See the calculations RBS/Channeling part of the chapter 2.
20. S R Lee, M West, A Allerman, E Waldrip, M Follstaedt, P Provencio, D Koleske and R Abernathy. Appl. Phys. Lett. 86 (2005) 241904.
21. B Heying, X H Wu, S Keller, Y Li, D Kapolnek, S P Denbaars, and J S Speck, Appl. Phys. Lett. 68 (1996) 643.
22. V M Kaganer, O Brandt, A Trampert and K H Ploog, Phys. Rev. B 72 (2005) 045423.
23. R Chierchia, T Bottcher, H Heinke, S Einfeldt, S Figge and D Hommel. Jour. Appl. Phys. 93 (2003) 8918.
24. V Srikant, J S Speck and D R Clarke, Jour. Appl. Phys. 82 (1997) 4286.
25. T Metzger, R Hoepler, E Born, O Ambacher, M Stutzmann, R Stoemmer, M Schuster, H Goebel, S Christiansen, M Albrecht and H P Strunk, Phil. Magz. A 77 (1998) 1013
26. J Elsner, R Jones, P K Sitch, V D Porezag, M Elstner, Th Frauenheim, M I Heggie, S Öberg and P R Briddon, Phys. Rev. Lett. 79 (1997) 3672.
27. B Heying, E J Tarsa, C R Elsass, P Fini, S P Den Baara and J S Speck, J. Appl. Phys. 85 (1999) 6470.
28. W Qian, G S Rohrer, M Skowronski, K Doverspike, L B Rowland, D K Gaskill, Appl. Phys. Lett. 67 (1995) 2284.
29. Z Liliental-Weber, Y Chen, S Ruvimov, and J Washburn, Phys. Rev. Lett. 79 (1997) 2835.
30. J E Northrup, R Di Felice, and J Neugebauer, Phys. Rev. B. 56 (1997) R4325.
31. E C Piquette, P M Bridger, Z ZBandic, and T C McGill, J. Vac. Sci. Tech. B. 17 (1999) 1241.



32. H W Choi, M G Cheong, M A Rana, S J Chua, T Osipowicz, and J S Pan, J. Vac. Sci. Tech. B. 21 (2003) 1080.
33. Properties Processing Applications of Gallium Nitride and Related Semiconductors, Ed by James H Edgar. IEEE, UK. Chapter A-7.3.
34. M Tchounkeu, O Briot, B Gil, J P Alexis, and R L Aulombard, J. Appl. Phys. 80 (1996) 5352.
35. B Monemar, P P Paskov, T Paskova, J P Bergman, G Pozina, W M Chen, P N Hai, I A Buyanova, H Amano, I Akasaki, Mater. Sci. Eng. B. 93 (2002) 112.
36. T Kawashima, H Yoshikawa, S Adachi, S Fuke, and K Ohtsuka, J. Appl. Phys. 82 (1997) 3528.
37. V G Dejbuk, A V Voznyy, M M Sletov and A M Sletov, Semiconductors. 36 (2002) 398.
38. B B Kosicki, R J Powell, and J C Burgiel, Phys. Rev. Lett. 24 (1970) 1421.
39. L H Qin, Y D Zheng, D Feng, Z C Huang, and J C Chen, J. Appl. Phys. 78 (1995) 7424.
40. J F Muth, J H Lee, I K Shmagin, R M Kolbas, H C Casey, B P Keller, U K Mishra, and S P Den Baars, Appl. Phys. Lett. 71 (1997) 2572.
41. R Goldhahn, S Shokhovets, J Scheiner, G Gobsch, T S Cheng, C T Foxon, U Kaiser, G D Kipshidze and W Richter, Phys. Stat. Sol. A. 177 (2000) 107.
42. M O Manasreh, Phys. Rev B. 53 (1996) 16425.
43. L. Balagurov and P J Chong, Appl. Phys. Lett. 68 (1996) 43.
44. W Rieger, R Dimitrov, D Brunner, E Rohrer, O Ambacher, M Stutzmann, Phys. Rev. B. 54 (1996) 17596.
45. C Marques, R C da Silva, A Wemans, M J P Maneira, A Kozanecki and E Alves, Nucl. Inst. Meth. B. 242 (2006) 104.
46. B Canut, A Benyagoub, G Marest, A Meftah, N Moncoffre, S M M Ramos, F Studer, P Thevenard and M Toulemonde, Phys. Rev. B. 51 (1995) 12194

## CHAPTER IV

### Effects of SHI on AlGa<sub>N</sub>/Ga<sub>N</sub> Heterostructures

Strain in the heterostructures modifies the electronic energy band structures and used to tailor and engineer the band gaps in optoelectronic devices. It can be used as an additional parameter to tune the device properties apart from the composition and the layer thickness of a heterostructure. The ternary semiconductor material AlGa<sub>N</sub> is of high importance for various devices. It is used in laser diodes as a cladding layer for waveguides as well as in field-effect transistors to form a two-dimensional electron gas. GaNs crystallize preferentially in the hexagonal wurtzite structure and are difficult to grow as large bulk crystals. Therefore, GaN is grown as heteroepitaxial film on various substrates, commonly on an Al<sub>2</sub>O<sub>3</sub> substrate. Apart from the large lattice mismatch of 16% between GaN and Al<sub>2</sub>O<sub>3</sub> along the [0001] plane, also there is a strain due to thermal mismatch between GaN and Al<sub>2</sub>O<sub>3</sub>. This elastic strain relaxation is an important issue and it affects the band gap of GaN based materials [1-4] and line-width of electroluminescence (EL) or photoluminescence (PL) spectra [5]. Generally this strain relaxation results in formation of threading dislocations which results in yellow luminescence band [6].

Usually AlGa<sub>N</sub> is pseudomorphically grown on GaN which is under tensile stress due to the mismatch of lattice parameters of -2.4% between AlN and GaN. This stress is reported to mostly relieve via the formation of cracks. As 'Al' content of AlGa<sub>N</sub> layer increases, two serious problems arise. First, AlGa<sub>N</sub> layers tend to crack since they are under high tensile stress when pseudomorphically grown on thick GaN buffers [7]. Second, p-type conductivity of Mg-doped AlGa<sub>N</sub> rapidly drops as the acceptor ionization energy increases [8]. Both the issues significantly degrade the device performance. In the case of AlGa<sub>N</sub> on GaN, the additional fact has to be considered that stress relief by the formation of misfit dislocations at the interface is very unlikely. High peierls forces in the 0001 oriented wurtzite layers prevent pre-existing threading dislocations from gliding. Even though GaN based materials and devices have been investigated very rapidly and intensely in recent years, there have been very few reports concerning the elastic strain in GaN based materials, especially in AlGa<sub>N</sub> and InGa<sub>N</sub> films. RBS/Channeling is a

reliable, nondestructive and accurate method for determining the strain in heterostructures [9-13]. In this chapter, we first discuss our results on the strain and crystalline quality of unirradiated AlGa<sub>0.2</sub>N layers by RBS/channeling and HRXRD. Then the effects of SHI on this AlGa<sub>0.2</sub>N layer have been presented based on the results of GaN layers given in the previous chapter.

Samples studied in this work are (50 nm) Al<sub>0.2</sub>Ga<sub>0.8</sub>N / (1 nm) AlN / (1  $\mu$ m) GaN / (0.1  $\mu$ m) AlN grown on SI 4H-SiC. These samples were irradiated with 150 MeV Ag ion at fluence of  $5 \times 10^{12}$  ion/cm<sup>2</sup>. Irradiation was performed at room temperature using NEC 15 MV pelletron accelerator at IUAC, New Delhi. Surface morphology of the samples has been studied by contact mode AFM. RBS/C measurements were carried out using 1.7 MV tandetron accelerator facilities at IGCAR, Kalpakkam. Strain values on irradiated and unirradiated samples were extracted from these RBS/C measurements. Incident ions energy dependence of dechannelling parameter has also been analyzed. Dependence of dechannelling parameter on the incident ion energy gives the quantitative and qualitative information about the defects present in the crystal.  $\langle 1213 \rangle$  axial channelling was carried out for dechannelling analysis by varying the incident energies between 2.3 and 3.8 MeV in steps of 0.3 MeV. The dechannelling parameter is calculated from the normalized back scattering yield to see the energy dependence for defects analysis as mentioned in the Chapter II. High resolution XRD experiments have been performed using the Philips X'Pert system at Padova, Italy. Reciprocal space mapping has been carried on 0002 direction in triple crystal mode while  $\omega$  &  $\omega$ -2 $\theta$  scans were extracted from the map. The experimental radial scans are fitted using Pseudo-Voigt function for integral width (FWHM or  $\beta$ ) and Lorentzian weight fraction ( $\eta$ ). Lateral correlation length and residual strain are calculated from FWHM and ' $\eta$ '. All the analysis has been carried as specified in the experimental details discussed in Chapter II.

#### **4.1. RBS/Channelling**

Energy dependence of dechannelling parameter has been studied in detail and the results have been analyzed from the known energy dependencies for various types of defects. As discussed in the experimental section, the normal axis  $\langle 0001 \rangle$  is not likely to be affected by the threading dislocations commonly observed in GaNs. So we have carried out the

dechannelling analysis on the off-normal axis  $\langle 1213 \rangle$ . Fig 4.1 shows the phi scan around the  $\langle 0001 \rangle$  axis. To get the  $\langle 1213 \rangle$  axis we first aligned the beam to  $\langle 0001 \rangle$  axis. Once we aligned the sample  $\langle 0001 \rangle$  axis then we rotated the sample  $30^\circ$  in  $\theta$  direction to get the  $\langle 1213 \rangle$  axis. There we did small iteration steps in  $\theta$  and  $\phi$  scans to obtain the  $\langle 1213 \rangle$  axis. Fig 4.2 shows the RBS aligned spectra of  $\langle 0001 \rangle$  and  $\langle 1213 \rangle$  axis. We observed very good  $\chi_{\min} \sim 2\%$  on  $\langle 0001 \rangle$  axis and  $\chi_{\min} \sim 18\%$  on  $\langle 1213 \rangle$  axis, which clearly indicates the most of the defects present in the sample are pure edge or screw dislocations. There are no mixed dislocations, which generally distorts the  $\langle 0001 \rangle$  axis. We observed high  $\chi_{\min}$  along off normal axis, which may be due to very high dislocation densities of the order of  $10^8$  to  $10^{10} \text{ cm}^{-2}$  commonly found in GaN. All these threading dislocations are expected to distort the off normal axis as calculated in the chapter 2.

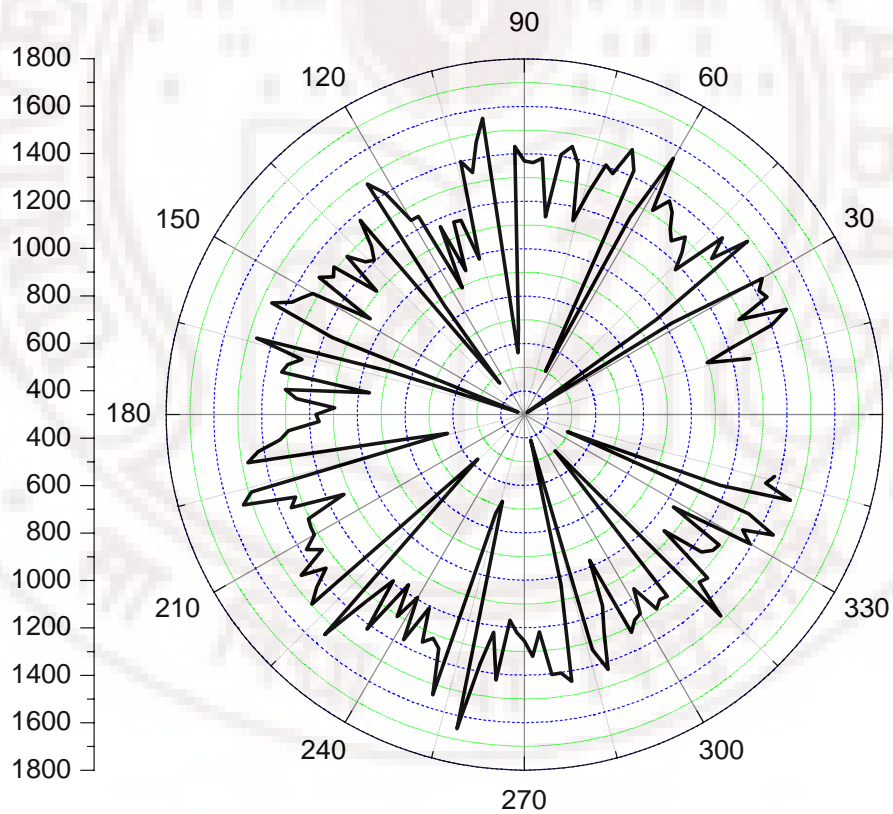


Fig 4.1  $\phi$  scan for the finding  $\langle 0001 \rangle$  axis

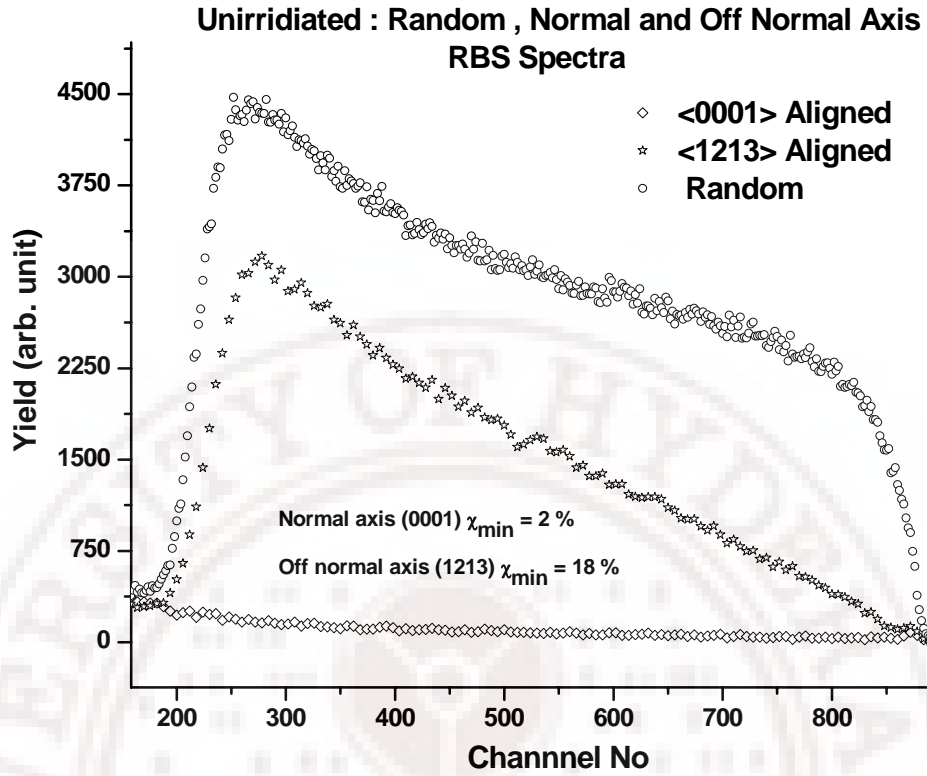


Fig 4.2. Normal and off normal axis aligned RBS/Channelling spectra of unirradiated sample.

RBS/Channelling strain measurements and energy dependence analysis were carried out along an off normal axis i.e. <1213> since angular scans along off normal axis give the tetragonal distortion ( $\epsilon_t$ ). In unirradiated sample, the layers are partially relaxed and AlGa<sub>N</sub> layer is still under a tensile strain of  $\epsilon_t = -0.55\%$  (See Fig 4.3). The  $\chi_{\min}$  of AlGa<sub>N</sub> layer is 12% and Ga<sub>N</sub> layer is 18% [14-16]. This shows that the samples have a high defect density. It also shows that  $\chi_{\min}$  along the normal axis is not affected by dislocations and the major effects are on the  $\chi_{\min}$  along the off normal axis. Incident ion energy dependent channelling shows  $\sim E^{0.5}$  behaviour and the defect density calculated was found to be  $2.1 \times 10^8 \text{ cm}^{-2}$  for Ga<sub>N</sub> layer and  $2.0 \times 10^8 \text{ cm}^{-2}$  for AlGa<sub>N</sub> layer (See Fig 4.4 (a), (b)). These values are close to each other. This may be due to the fact that we calculated defect density both at the layer and in the region just below the AlGa<sub>N</sub> layer.

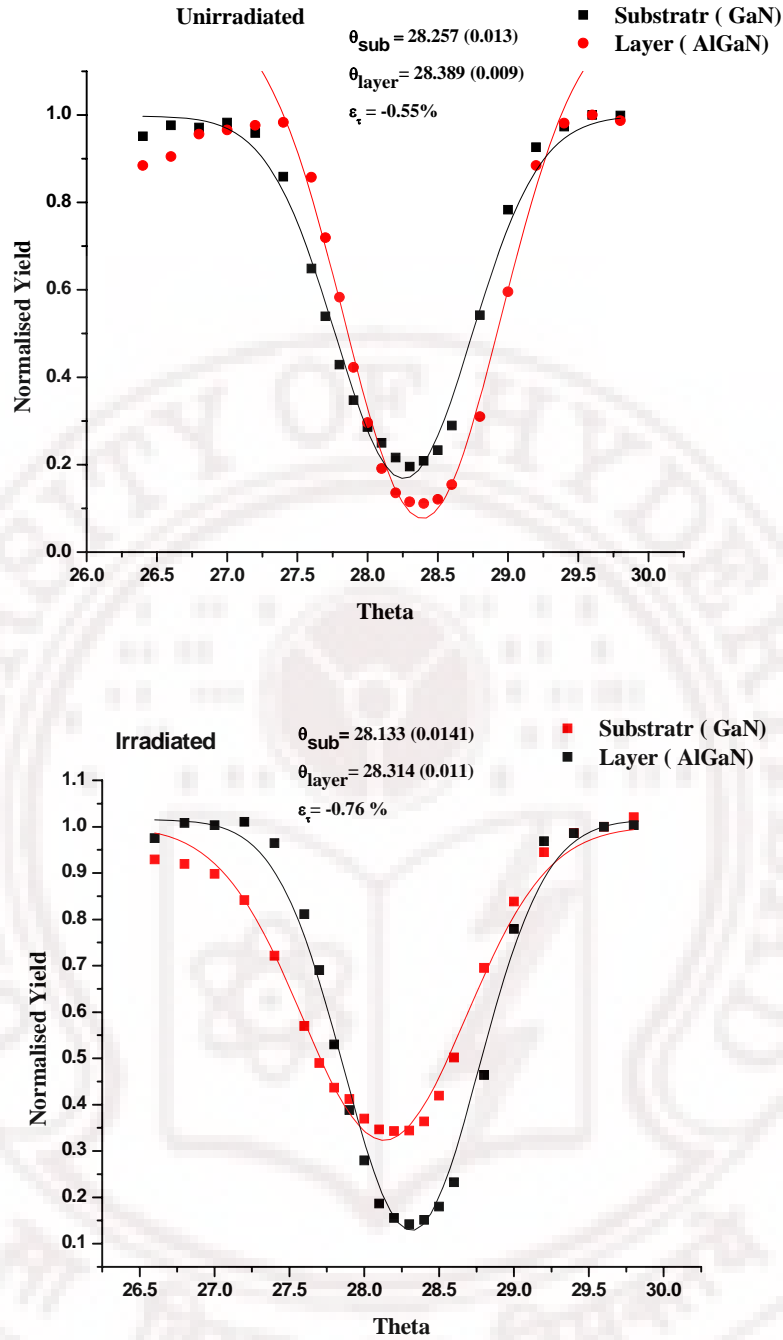


Fig.4.3. Channelling angular scans for the strain measurement on the off normal axis.

In the irradiated samples we observed that the  $\chi_{\min}$  of GaN layer has increased to 33.6% and that of AlGaN to 15.8%. It is clearly evident from these increases that the AlGaN layer is more radiation resistant than the GaN layer and therefore very few defects are created in the AlGaN layer. Irradiation and dynamic annealing induces more tensile strain in AlGaN layer as seen from the calculated value  $\epsilon_t = -0.76$  in fig 4.3. The energy

dependence of DP for GaN layer is  $E^{0.37}$  and for AlGaIn layer is  $E^{0.69}$ . Also there is an increase in the scattering of data points (see Fig 4.4 (c)). This may be due to the irradiation induced clustering of threading dislocations. At the core of these complex defects ions sees a random matrix. Defect density of GaN layer is  $3.7 \times 10^8 \text{ cm}^{-2}$  and that of AlGaIn layer is  $3.2 \times 10^8 \text{ cm}^{-2}$  as seen in Fig 4.4 (d) and we notice that there is an increase in the defects after irradiation in both the layers. However the increase in AlGaIn layers is less than in GaN, which may be because of the strain introduced in the top layer.

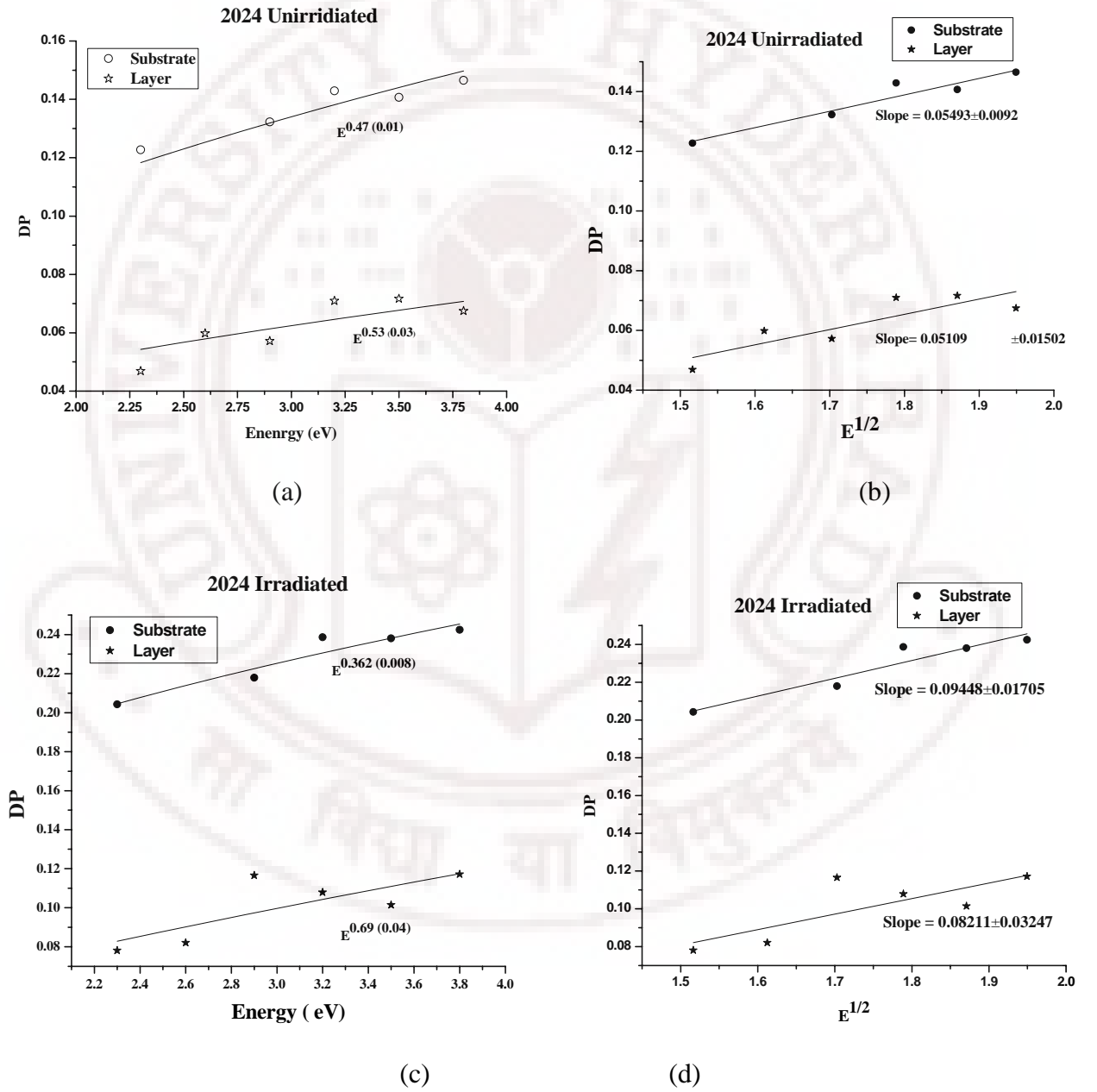


Fig.4.4. Incident ion energy dependence analysis of the dechannelling parameter on the off normal axis.



Generally, point defects are not expected in MBE grown samples. Angular scans from both, the layer (AlGaIn) and the substrate (GaIn) regions were analyzed for possible point defects after irradiation. The yield from interstitial atoms located near the centre of the channels will be greater than the non-channelling value, generally referred to as flux peaking in the angular scans. From fig 4.3, absence of interstitial atoms at the centre of the <1213> channels of angular scans for both AlGaIn and GaIn layers are confirmed. But to completely rule out the possibility of interstitial point defects, one has to carry out the channelling angular scans along three axes i.e. one normal and two off normal axes.

The flux distribution of the channelled ions may not be stationary at smaller thicknesses as reported by theoretical and recent computational studies [17–20]. The flux oscillation which increases with increase in beam divergence, is 3 times smaller in axial case compared to the planar case. It has been reported that the quantitatively, theoretical and experimental values do not yield satisfactory agreement [21]. For 1.8 MeV He channelling along the <110> direction of Si, the statistical equilibrium achieved at a depth of 220 nm determined experimentally as against the theoretical prediction of about 97.5 nm [21]. We have calculated the mean free path  $\lambda_1$  to achieve equilibrium using the following equation [21 – 22],

$$\frac{1}{\lambda_1} = \left( \frac{\pi^2}{4} \right) \left( Nda \frac{\psi_1^2}{\psi} \right)$$

where N is the atomic density of the material, ‘a’ is the Thomas-Fermi screening radius, and ‘ $\psi$ ’ is the incident angle with respect to the channel axis. The calculated value of  $\lambda_1$  is 89.7nm for 3MeV He channelling along <0001> direction of GaIn assuming  $\psi_1=\psi$ . Our results indicate that the statistical equilibrium is probably achieved at smaller thickness (~50nm) than predicted by the above formula. The present results are consistent with ones reported in Ref [21], where experimental values were found to be higher than the theoretical values. Also, we observed symmetric angular scans for <1213> axis, which indicates that the flux distribution is stationary at these thicknesses. The partially relaxed AlGaIn layer and larger channels might be a reason for the observed stationary flux

distribution at smaller thickness. Defect studies by channelling on thin samples similar to the present ones have been reported in the past [23-26].

## 4.2. HRXRD

Fig 4.5 & 4.6 show  $\omega$  and  $\omega$ -2 $\theta$  scans extracted from the reciprocal space map of <0002> direction, and all the scans were fitted using Pseudo-Voigt function. Lateral Correlation length ( $L_{||}$ ), Lorentzian shape function ( $\eta$ ) and defect density ( $N_D$ ) were calculated from the parameters extracted from the fit and all the calculated values are given in Tables 4.1 & 4.2. FWHM of unirradiated GaN layer is  $0.168^\circ$  and Lorentzian shape function is 0.74. This shows that GaN has many defects and the broadening is mainly due to dislocations.  $L_{||}$  of GaN layer is 192 nms which implies that the layer is having many dislocations with a calculated density of  $9.4 \times 10^7 \text{ cm}^{-2}$ . AlGaIn layer has a FWHM of  $0.204^\circ$ , which is very high and the broadening is due to defects and thickness effects. Lorentzian shape function of the layer is 0.60, which implies that the defects from the GaN layers are travelling across interface to AlGaIn layer. Lateral correlation length of 172 nms shows that the AlGaIn layer has more defects than the GaN layer. It may be due to strain relaxation that adds more dislocations in the AlGaIn layer with a calculated defect density of  $2.4 \times 10^8 \text{ cm}^{-2}$  [27-30].

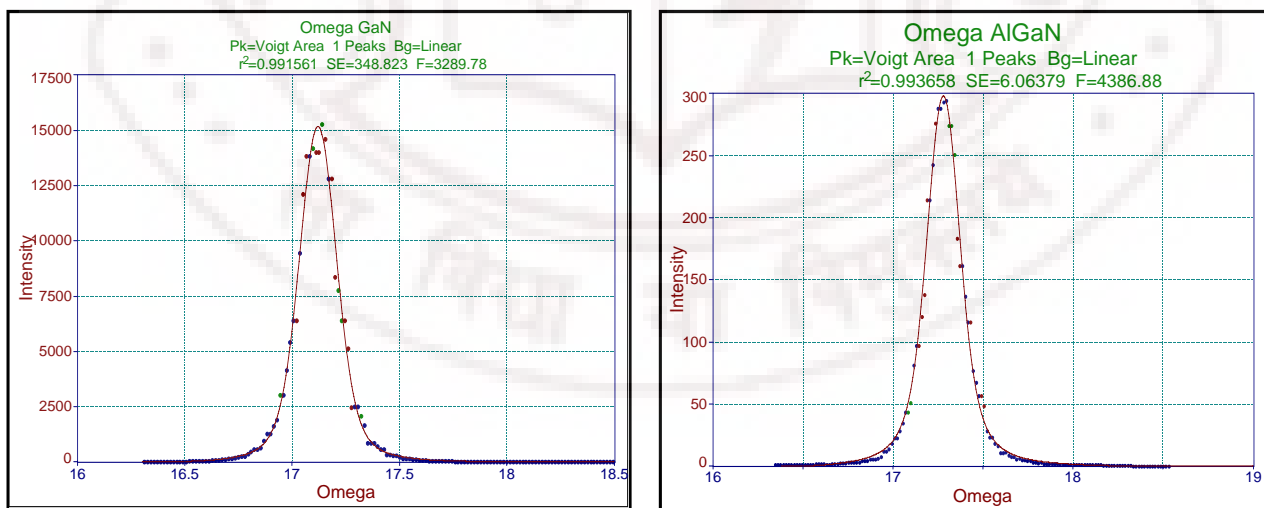


Fig4.5. Omega scan of GaN and AlGaIn layers irradiated sample.

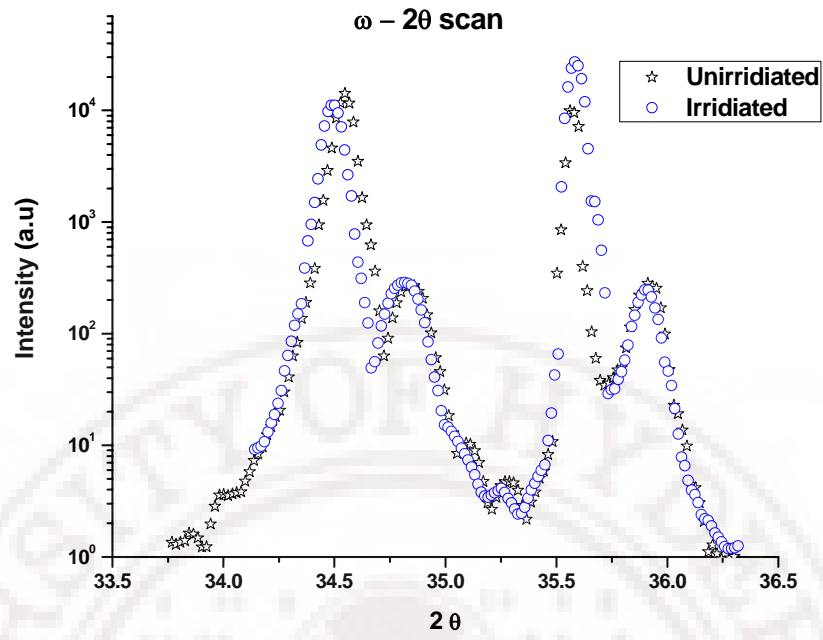


Fig .4.6. Radial ( $\omega$ - $2\theta$ ) scans of unirradiated and irradiated 2024 samples.

Table.4.1. Lateral Correlation Length, Defect density and strain obtained from HRXRD and RBS/Channelling

Sample	Lateral Correlation Length ( $L_{ll}$ )	Defect Density ( $N_D$ )HRXRD	Tetragonal distortion Stain ( $\epsilon_t$ )	Defect density ( $N_D$ )RBS/C
Unirradiated GaN Layer	192 nm	$9.4 \times 10^7 \text{ cm}^{-2}$		$2.1 \times 10^8 \text{ cm}^{-2}$
Unirradiated AlGaIn Layer	172 nm	$2.4 \times 10^8 \text{ cm}^{-2}$	-0.55 %	$2.0 \times 10^8 \text{ cm}^{-2}$
Irradiated GaN Layer	276 nm	$5.0 \times 10^8 \text{ cm}^{-2}$		$3.7 \times 10^8 \text{ cm}^{-2}$
Irradiated AlGaIn Layer	167 nm	$2.9 \times 10^8 \text{ cm}^{-2}$	-0.76%	$3.2 \times 10^8 \text{ cm}^{-2}$

Table.4.2. FWHM,  $\eta$  and  $\omega$  extracted from the Pseudo voigt function fitting of HRXRD scans.

Sample	FWHM	Shape	Omega
2024U – GaN	0.1686	0.74	17.1454
2024U – AlGaIn	0.2042	0.60	17.2868
2024I – GaN	0.2075	0.35	17.1193
2024I – AlGaIn	0.2231	0.59	17.2785

After irradiation, the thick GaN layer shows an increase in FWHM to  $0.207^\circ$  and reduction in Lorentzian shape function to 0.35, clearly indicating the increase in defects. Lateral correlation length is increased to 276 nms. Irradiation gives enough energy to dislocations to move laterally. As a result, these dislocations cluster and the lateral correlation length increases even though the defects density increases to  $5.0 \times 10^8 \text{ cm}^{-2}$ . In AlGaIn layer, FWHM increases to  $0.223^\circ$ , which shows that there is an increase in defects. However there is no change in Lorentzian shape function within the experimental error. In addition, with a calculated defect density of  $2.9 \times 10^8 \text{ cm}^{-2}$ , the change is very less compared to corresponding changes in GaN layer. So the increase in FWHM may be due to the defects created at the interface of the AlGaIn layer and point defects introduced by the swift heavy ions. It has been reported that AlN based nitrides have shown strong dynamic annealing behaviour due to swift heavy ion irradiation [31, 32].

Reciprocal space map of 2024 in  $\langle 0002 \rangle$  direction clearly shows that the layers are relaxed (See Fig 4.7 (a) & (b) ). After irradiation it has been observed that there is a very diffuse scattering due to the defects introduced by swift heavy ions.

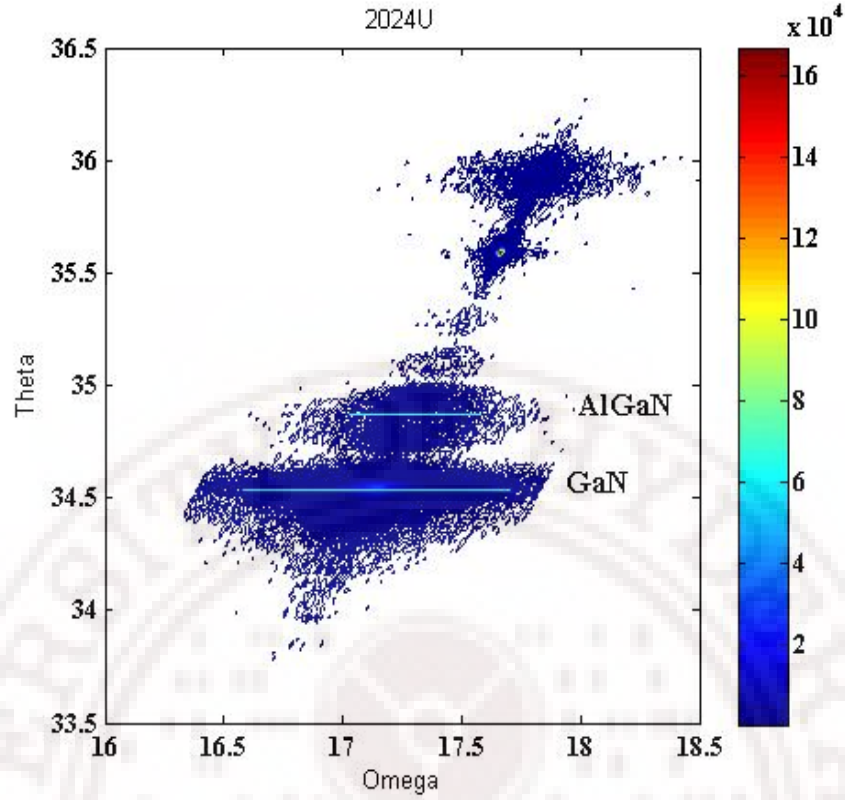


Fig 4.7 (a) Reciprocal space map of unirradiated 2024.

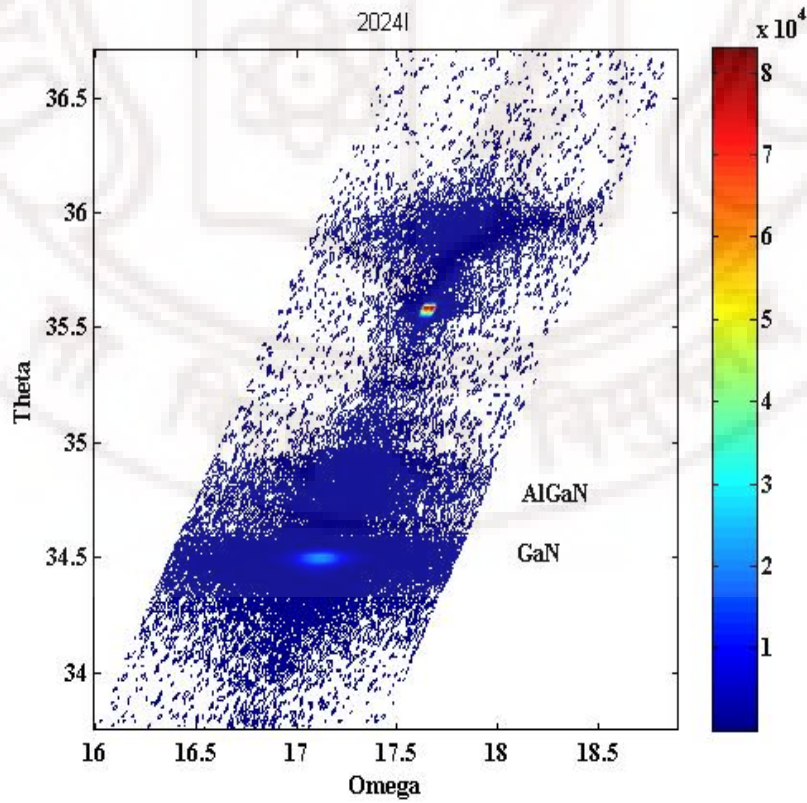


Fig.4.7 (b) Reciprocal space map of irradiated 2024.

### 4.3. AFM

Contact mode AFM was carried out on both irradiated and unirradiated samples. In as grown samples, we observe pinned steps or hillocks and holes (See Fig 4.8). The size of hillocks ranges from 10 to 100 nms. Generally these hillocks or pinned steps are formed as the screw threading dislocations ends at the surface. The size of these hillocks normally depends on the strain involved in the dislocation core, which resulted in pushing the material away from the dislocation core i.e. to the surface. Deep holes are formed when the edge threading dislocations terminate at the surface and the sizes of these holes are few nms [33]. In as grown samples we observed both kinds of morphology. It is evident from the surface morphology that both kinds of defects i.e. Edge and screw dislocations are present in our sample.

In the irradiated samples we observe similar morphology as in the unirradiated ones, with surface blistering. This may be due to the surface mass transport induced by SHI. In III-Nitrides the dislocation density is high; SHI gives the enough energy for the movement of dislocations. When it reaches the surface, it clusters and forms a bigger hole. Clustering of dislocations was observed when we did the AFM scans inside one of the big holes (see Fig 4.9). Apart from this we did not observe any other major changes on the surface; this may be due to strong natural strength (hardness) of AlGaIn layer to irradiation.

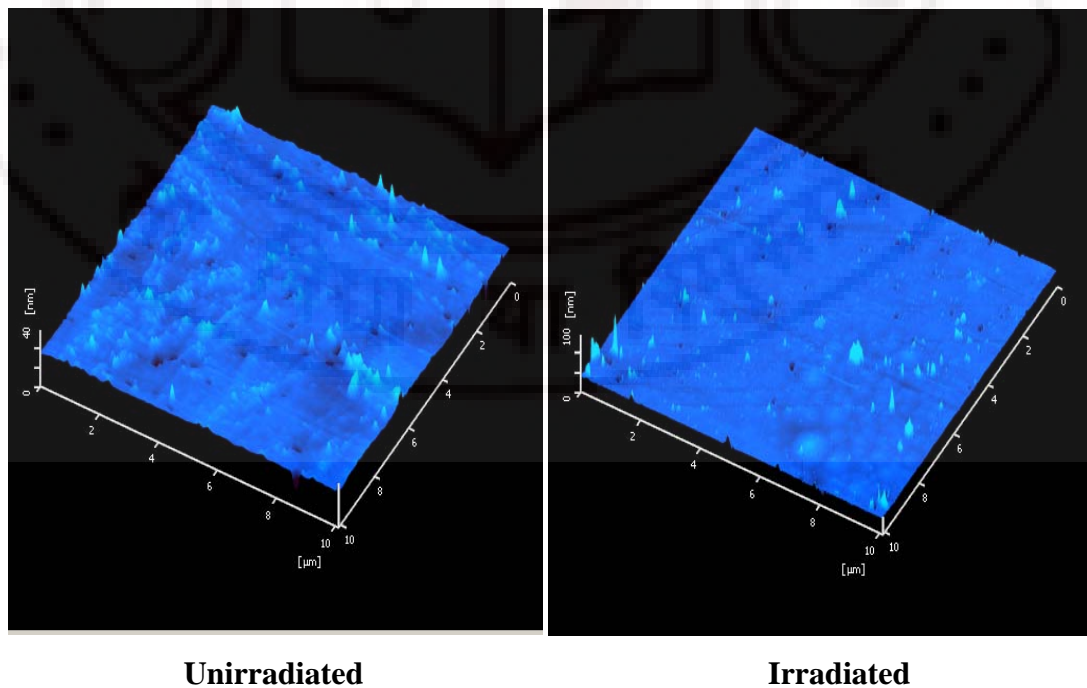


Fig 4.8. 10  $\mu\text{m}$  scan of surface morphology of unirradiated and irradiated sample.



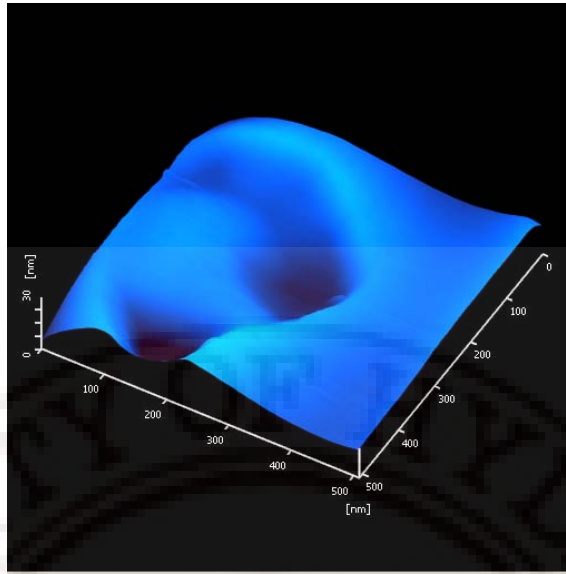


Fig.4.9. AFM scan shows clustering of the small holes to form bigger ones.

#### 4.4. Conclusion

Swift heavy ion irradiation effects on relaxed AlGaIn/GaN heterostructures have been analysed using RBS/Channelling, HRXRD and AFM. Channelling strain measurement shows that unirradiated sample has a small residual tensile strain which increases after irradiation. One would expect that when strain increases defect density should decrease. But here, the defect density in AlGaIn and GaN layers increases after irradiation. AFM surface morphology shows that there is a clustering of defects at the surface due to irradiation. This complements the increase in lateral correlation length from HRXRD measurements. The difference in the calculated defect density by RBS/Channelling and HRXRD was attributed to the fact that HRXRD gives depth averaged information, whereas RBS/C yields depth resolved information. SHI deposits very high energy into the materials by electronic interactions. These electrons transfer this energy into the lattice by electron phonon coupling. The energy transferred depends on the material properties. There are two competing processes which decide the material modification. First one is the deposited high energy in small diameter causing the materials to melt at very small time scale i.e. in order of pico seconds. Second process is the dynamic self annealing of materials initiated by its bond strength which tries to crystallise the material at the same time. These two processes compete with each other depending on the material properties.



In III-Nitrides the process of dynamic annealing is very strong because of its high bond strength. Al-N bond is stronger than Ga-N, so Al-N recombines faster and complete epitaxial reconstruction of AlGa<sub>N</sub> layer has been observed. However, in Ga<sub>N</sub> layer epitaxial reconstruction has also been observed which causes the reconstruction of 3D grown Ga<sub>N</sub> buffer layer (existing in the form of islands). This results in release of the strain to the extent of about ~16 % between Ga<sub>N</sub>/Sapphire. The same has been reported by S. O. Kucheyev et.al, [34] where they observed *peeling off* from the bulk epitaxial Ga<sub>N</sub> layer upon 200 MeV Au ions at fluence of  $1 \times 10^{13}$  ions/cm<sup>2</sup>. In our samples the lower  $S_e$  and lower fluence prevented the peeling of the layer due to irradiation. Consequently, we observed more threading dislocations in both the layers. Swift heavy ion induces more strain in AlGa<sub>N</sub> and Ga<sub>N</sub> layers by the process of dynamic annealing. At the same time, as a result of Ga<sub>N</sub> buffer layer getting reconstructed, more threading dislocations are induced and travel to the surface.

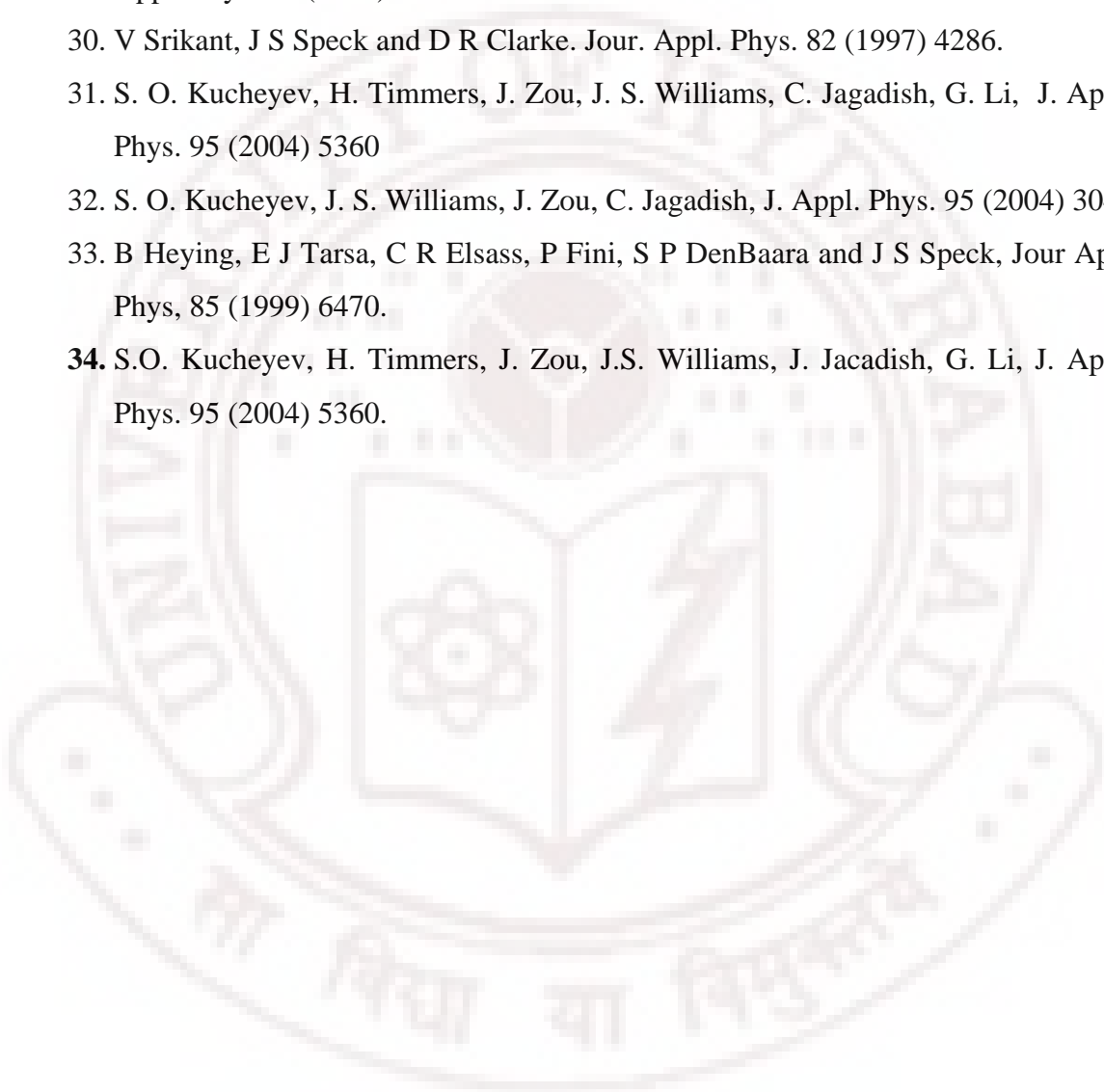
Generally one would expect that ion beams generate defects and common question is that, why to subject Ga<sub>N</sub> to ion beam irradiation, as it is already highly defected? One could avoid the defects creation due to the ion beam by using very thick (~100  $\mu$ m) Ga<sub>N</sub> layers (like HVPE grown Ga<sub>N</sub> templates for AlGa<sub>N</sub> layer) and then subjecting it to ion irradiation will result in improving the AlGa<sub>N</sub> layer and its interface quality without increasing the dislocation density (which is of importance). In these samples, these ions will not reach the Ga<sub>N</sub>/Sapphire interface, as their range is ~ 11 to 13  $\mu$ ms.

## References

1. T. Takeuchi, H. Takeuchi, S. Sota, H. Sakai, H. Amano, and I. Akasaki, Jpn. J. Appl. Phys., Part 2 36, L177 (1997).
2. M. D. Bremser, W. G. Perry, T. Zheleva, N. V. Edwards, O. H. Nam, N. Parikh, D. E. Aspnes, and R. F. Davis, MRS Internet J. Nitride Semicond. Res. 1 (1996).
3. X. Zhang, P. Kung, A. Saxier, D. Walker, T. C. Wang, and M. Razeghi, Appl. Phys. Lett. 67, 1745 (1995).
4. C. Wetzel, T. Takeuchi, S. Yamaguchi, H. Katoh, H. Amano, and I. Akasaki, Appl. Phys. Lett. 73, 1994 (1998).
5. K. P. O'Donnell, T. Breitkopf, H. Kalt, W. Van der Stricht, I. Moerman, P. Demeester, and P. G. Middleton, Appl. Phys. Lett. 70, 1843 (1997).
6. F. A. Ponce, MRS Bull. 22, 51 (1997).

7. K. Itoh, K. Hiramatsu, H. Amano, and I. Akasaki, *J. Cryst. Growth* 104, 533 (1990).
8. M. Suzuki, J. Nishio, M. Onomura, and C. Hongo, *J. Cryst. Growth* 189, 511 (1998).
9. L C Feldman, J W Mayer and S T Picraux, *Materials Analysis by Ion Channeling*, Academic Press, New York (1982).
10. J H Barret, *Appl. Phys. Lett.* 40 (1982) 482.
11. C Wu, S Yin, J Zhang and G Xiao, *J. Appl. Phys.* 68 (1990) 2100.
12. A V Drigo, A Aydinil, A Carnera, F Genova, C Rigo, C Ferrari, P Franzosi and G Salviati, *J. Appl. Phys.* 66 (1989) 1975.
13. M Mazzer, A V Drigo, F Romanato, G Salviati and L Lazzarni, *Phys. Rev. B* 56 (1997) 6895.
14. M. F. Wu, Shude Yao, A. Vantomme, S. M. Hogg, G. Langouche, J. Li, G. Y. Zhang, *J. Vac. Sci. Technol. B* 17 (1999) 1502
15. M.F. Wu, A. Vantomme,<sup>1</sup>, S. Hogg, G. Langouche, W. Van der Stricht, K. Jacobs, I. Moerman, *Nucl. Instr. Meth. B* 174 (2001) 181
16. D Zhi-Bo, W Kun, Z SHeng-Qiang, C Tian-Xiang, Y Shu-De, *Chin. Phys. Lett.* 24 (2007) 831.
17. J H Barrett, *Phys. Rev B* 3 (1971) 1527.
18. M L Swanson, *Rep. Prog. Phys.* 45 (1982) 47.
19. L Nowicki, A Turos, R Ratajczak, A Stonert and F Garrido, *Nucl. Instr. and Meth. B* 240 (2005) 277.
20. L Nowicki, A Turos, C Choffel, F Garrido, L Thome, J Gaca, M Wojcik, HJMatzke, *Phys. Rev. B* 56 (1997) 534.
21. B A Davidson, L C Feldman, J Bevk and J P Mannaerts, *Appl. Phys. Lett* 50 (1987) 135.
22. J A Golovchenko, *Phys. Rev B* 13 (1976) 4672.
23. S Hashimoto, L S Wielunski, J –L Peng, W M Gibson and L J Schowalter, *Nucl. Instr. and Meth. B* 13 (1986) 65.
24. A C Chami, E Ligeon, J Fontenille and R Danielou, *J. Appl. Phys.* 62 (1987) 3718.
25. G Linker, *Nucl. Instr. and Meth.* 149 (1978) 365.
26. L J M Selen, L J Van. IJzendoorn, M J A de Voigt and P M Koenraad, *Phys. Rev. B* 61 (2000) 8270.

27. T. Metzger, R. Hoepler, E. Born, O. Ambacher, M. Stutzmann, R. Stoemmer, M. Schuster, H. Goebel, S. Christiansen, M. Albrecht and H. P. Strunk, *Phil. Magz. A* 77 (1998) 1013
28. Kaganer VM, Brandt O, Trampert A and Ploog KH. *Phys. Rev. B* 72 (2005) 045423.
29. R Chierchia, T Bottcher, H Heinke, S Einfeldt, S Figge and D Hommel. *Jour. Appl. Phys.* 93 (2003) 8918.
30. V Srikant, J S Speck and D R Clarke. *Jour. Appl. Phys.* 82 (1997) 4286.
31. S. O. Kucheyev, H. Timmers, J. Zou, J. S. Williams, C. Jagadish, G. Li, *J. Appl. Phys.* 95 (2004) 5360
32. S. O. Kucheyev, J. S. Williams, J. Zou, C. Jagadish, *J. Appl. Phys.* 95 (2004) 3048
33. B Heying, E J Tarsa, C R Elsass, P Fini, S P DenBaara and J S Speck, *Jour Appl Phys*, 85 (1999) 6470.
34. S.O. Kucheyev, H. Timmers, J. Zou, J.S. Williams, J. Jacadish, G. Li, *J. Appl. Phys.* 95 (2004) 5360.



# CHAPTER V

## Er implantation into GaN layers

The Electro-Luminescence (EL) of Rare Earth (RE) and Transition Metal (TM) ions is an important subject of research and development, both from fundamental as well as applied view points. RE and TM ions may be introduced into different hosts like oxides, sulfides or semiconductors. If these ions are excited by collisions with high energy electrons, they emit characteristic light of different colors. These so-called phosphors are used for fluorescent lamps, field emission displays, color TV tubes and plasma displays [1]. They are potentially useful for modern flat panel displays and optoelectronic emitters, because they do not need the crystalline perfection of the typical direct bandgap semiconductors, which are the basis for light emitting diodes or laser diodes. At present, the wide bandgap semiconductor GaN has emerged as an important host for RE-EL [2–4]. In these applications, GaN is not used as a bandgap recombination emitter of blue light, but as a host with large bandgap (3.4 eV) and sufficient carrier mean free path. Over the past few years gallium nitride (GaN) has attracted considerable worldwide attention due to its excellent properties, making it a promising material for a variety of optoelectronic and microelectronic applications. This is due to its wide and direct band gap of 3.4 eV, which makes this semiconductor very attractive candidate as a host for optical doping with rare-earth (RE) elements. Among these RE elements, Erbium has been intensively investigated as a possible dopant since it exhibits sharp emission lines in the infrared (around 1.54  $\mu\text{m}$ ) as well as visible region (green emission at 537 nm and 558 nm).

AlN as a host had been studied earlier [5–8] which has a high band gap of 5.6 eV and hence very good insulator. Annealing temperatures of at least 800°C are needed to activate the RE ions. No diffusion of the RE ions has been observed even at 1100°C (60 min). Dimitrova et al [8] have fabricated an Er:AlN thin film for use as EL device, which is operated at 116 V and 60 Hz at a film thickness of 200 nm. The Er concentration was 0.08–0.25 at. % [9]. The most impressive results so far have been achieved by RE doped films of GaN [2–4, 9–14]. For an overview see ref [2]. Especially due to the efforts of the Cincinatti group a full range of colors have been demonstrated. The EL devices under investigation are operated under low voltages (e.g.  $\sim 7$  V) and show very satisfactory

quantum efficiencies. The excitation and de-excitation processes for ion implanted solid state EL devices have been discussed in the above referred literature. For the purpose of thin film optical emitters, at present the RE doped GaN films offer the greatest potential with a full range of colors, a very satisfactory quantum efficiency and long term stability. DC and AC driven devices have been demonstrated. In addition, different RE systems are also evaluated as potential light sources, which may be compatible with silicon processing for silicon based optical emitters [15]. Ongoing research on the Er:Si system leads to the expectations of a RE laser on a silicon substrate, since the Er:Si pnp transistor as well as the RE doped GaN films are most promising for future developments.

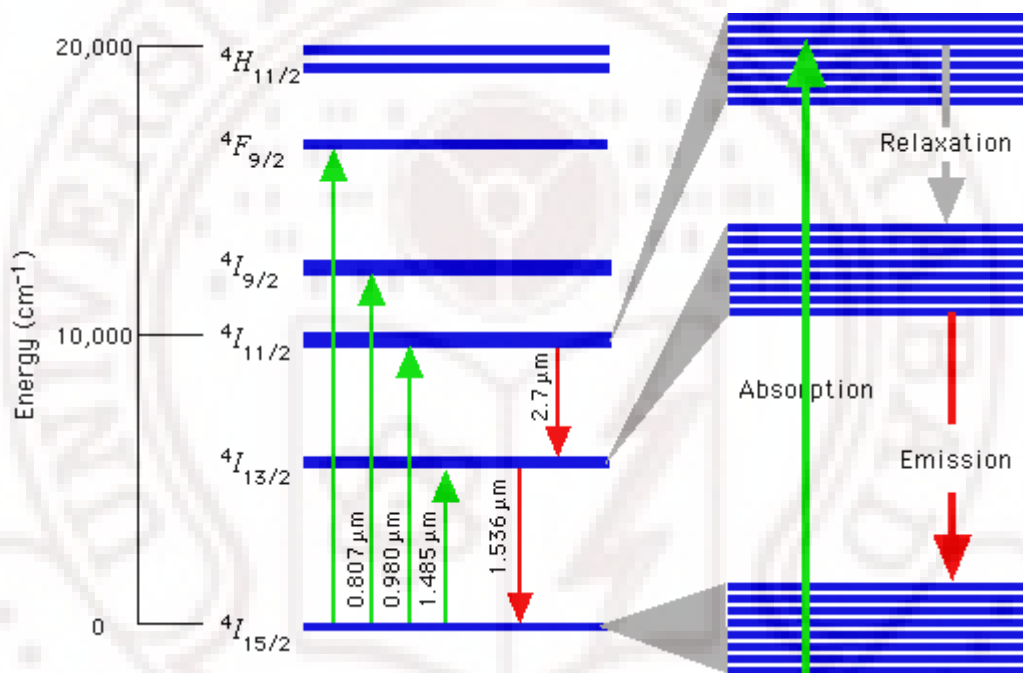


Fig 5.1 energy levels of the Er ions

Generally emission wavelength of the 4f shell of rare-earth elements is not affected by the solid host. But the transition probability (i.e. emission intensity) is affected by the host matrix. However, incorporating rare-earth (RE) elements into a solid with an appropriate crystal field induces a small perturbation to the 4f levels and relaxes the selection rule by admixing states of opposite parity. RE ions incorporated into a partially ionic solid, occupying the cation sites are exposed to uneven crystal fields that produce perturbation and partially relax the selection rules [16]. But the intra-4f transitions are still not fully allowed, resulting in the experimentally observed excited state lifetimes of the order of

ms [17]. Most probable site of Er ions is Ga substitutional in GaN with symmetry of  $C_{3v}$  and the neighboring environment of GaN are good for incorporating large number of Er-emitting centers [18]. The different energy levels of  $Er^{3+}$  ions are shown in the Fig 5.1.

GaN has proven to be an accomplished host, with reports of fabrication of light-emitting diodes (LEDs) operating in the visible and infrared region [19-21]. Fig. 5.2 shows the results of an Er-doped GaN Schottky diode synthesized by MBE for which a strong IR (1.54  $\mu m$  transition) and VIS emission (537,556 nm transition) is seen [20]. It has been demonstrated that the GaN:Er have emissions at Green ( 550 and 665 nm) and IR (1000 and 1550 nm) regions. Green emission is visible at room temperature. There are four possible mechanisms of emission in GaN:Er ; those are N-Vacancy related ( $V_N$ ),  $RE_{Ga}-V_N$  defect complex,  $N_{Ga}$ - Nitrogen anti-site point defects and RE dopant emission. It has been shown that emission is more from N rich regions and it is independent of defects upto a critical concentration. Up to 1 at % of Er it is stable and beyond that Er-Er cross relaxation and Er-GaN defects relaxations are observed. In the implanted samples, it is observed that up to a dose of  $5 \times 10^{14}$  ions/cm<sup>2</sup>, damages created can be recovered by annealing or partially by self dynamic annealing. Higher dose implantation leads to complete amorphisation of the material. Normally, Er ion can be activated at 900°C annealing for 30 mins but in the implanted samples even 1100°C did not recover the implantation induced damages. High temperatures (say~ 1200 °C) and high pressure annealing can be used to complete epitaxial re-growth of the material.

Eventhough the devices based upon Er-doped GaN have been achieved, but these still suffer from low quantum efficiency at the IR wavelength. So the better understanding of the excitation and emission dynamics of the Er-doped GaN system and Er lattice position under different processing conditions are required. In the present study we have reported systematic implantation of Er by varying the ion fluence and annealing temperature for a better optical activation. RBS/Channeling has been carried out to characterize the lattice site of Er atoms and Photoluminescence study to measure the optical quality of the sample. The effects of implantation dose and annealing temperature on the optical activation and the Er lattice sites in GaN have been investigated.



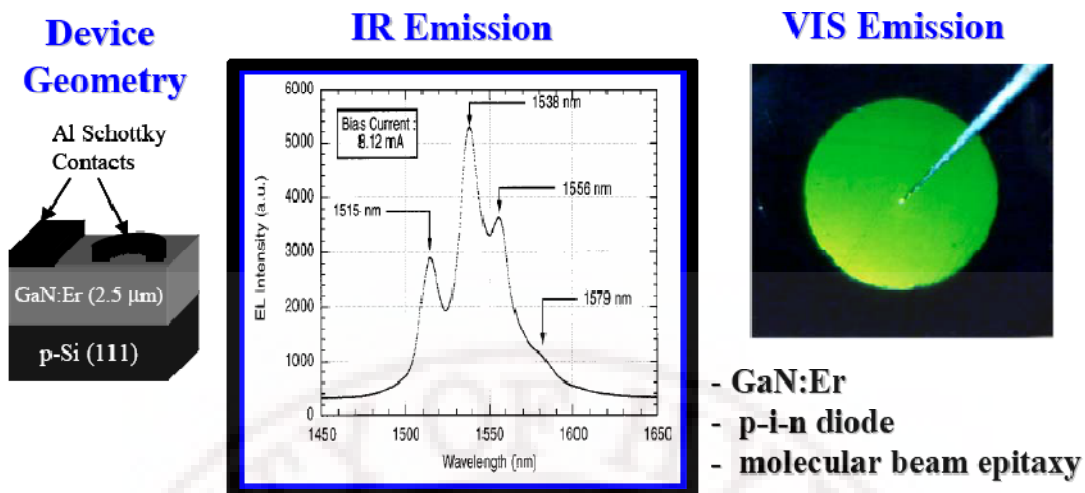


Fig 5.2 Er doped GaN schottky diode synthesized by MBE

Set of samples cut from same wafer of GaN film on  $\text{Al}_2\text{O}_3$  substrate has been implanted with 190 keV  $\text{Er}^{3+}$  ions, followed by post-implantation annealing. Projected range of these 190 keV Er ions are 35 nms with straggling of 11 nms. Annealing was carried out in a conventional furnace, with a  $\text{N}_2$  flow kept constant during the process. The duration was always set at 1h, with annealing temperature fixed at 800°C, 950°C and 1100°C. Optical absorption (OA) measurements, PL, Time-resolved PL analysis, PL excitation (PLE) measurements and RBS/Channelling have been performed as specified in the experimental part of this thesis i.e. chapter2.

## 5.1 PL studies

### 5.1.1 Optical properties of the as-implanted ErGaN samples

After the implantation process, no luminescence related to the presence of the rare earth was detected. On the other hand, all the series exhibit a darkened surface, going from dark yellow for *ErGaN1 as-implanted* to a plain metallic colour for *ErGaN10 as-implanted*. This might be due to Ga segregation effect induced by the Er ion implantation. The effects are more on the system with the higher implantation dose of Er, as evidenced by the colour change of the samples. We observed (Fig.5.3) a structured background, characterized by a climbing profile going towards the UV with a band around 450nm.



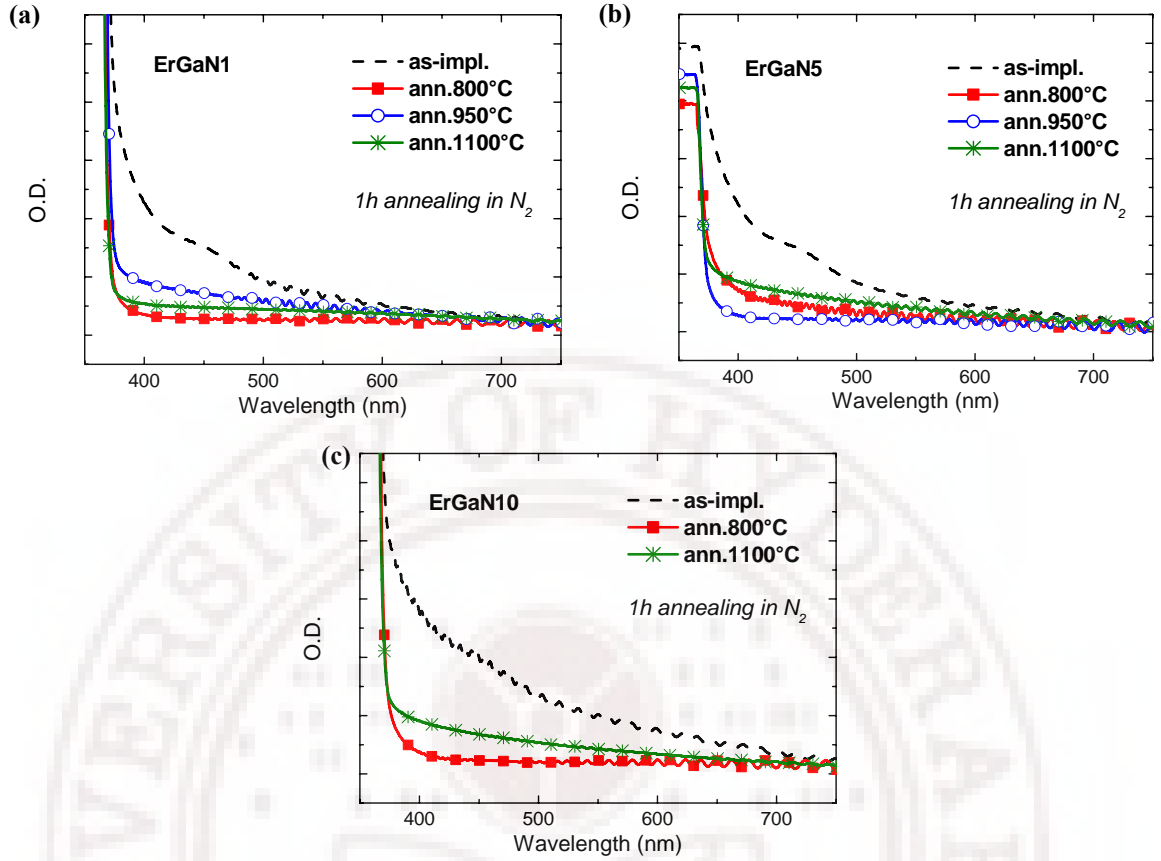


**Fig.5.3.** Optical absorption spectra in the visible range for all the samples analyzed in these experiments. (a) *ErGaN1* (b) *ErGaN5* (c) *ErGaN10*

After annealing, the samples become almost completely transparent, possibly due to the recovery of the GaN matrix by  $N_2$  atmosphere. In Fig.5.3, we observed that the annealing treatment reduces the optical activity in the visible of the as-implanted samples. It is worth noticing that all the spectra are characterized by a prominent threshold at around 370nm, with signal saturation in the UV, which may be due to the band edge of the GaN (3.4eV).

### 5.1.2 Annealing effects on the ErGaN PL properties

After post-implantation annealing, the main result is the activation of the typical Er ion PL emission in the 1450-1650 nm range, related to radiative  $^4I_{13/2} \rightarrow ^4I_{15/2}$  transition from first excited level to ground state. For each set, depending on the Er doping dose, we observe a specific behaviour linked to the variation of the annealing temperature that strongly determines PL emission band shape, intensity and lifetime. Fig.5.4 shows the normalised and un-normalised PL spectra for the annealed samples of all the series.

The analysis of the normalized spectra gives important elements for the study of the structural site in which the optically active Er ions are located. In general, it is observed that increasing the annealing temperature up to 1100°C all the three series show a very similar PL spectral shape (see Fig.5.4(h)): a main peak located at 1542nm with a shoulder at around 1558nm (FWHM of 33nm) and a series of weaker PL structures at 1519, 1572 and 1591nm, due to the Stark sub-level splitting. These features emerge as the temperature is raised, as evidenced by the behaviour of *ErGaN5* (see Fig.5.4(d)) and *ErGaN10* (see Fig.5.4(f)). The presence of these Stark structures is strongly related to the crystallinity of the environment in which the Er ion site is located. In fact they reflect the interaction with the phonon modes of the GaN lattice structure.

For *ErGaN1* samples, (see Fig.5.4(b)) the 800°C-annealed sample shows a completely different shape from the other set of samples for the PL emission linked to the  $^4I_{13/2} \rightarrow ^4I_{15/2}$  transition. In fact the structure is characterized by a broad band covering the whole explored range in which we can distinguish only the main peak at 1542nm and the shoulder at 1558nm (FWHM of 63nm). This is the typical behaviour for Er ions embedded in an amorphous host (as a glass). The intensity of the NIR PL emissions are shown in Fig.5.5 where *ErGaN1* shows a different behaviour with respect to the other two series. While the later two series show signals dropping down at 1100°C, *ErGaN1-1100°C* exhibits an evident signal increase in comparison with the other samples belonging to the same series. In principle, a larger signal (due to temperature increase) can be related to: (i) the recovery of the matrix damaged by the implantation process, resulting in an overall increase of the quantum efficiency for the PL process; (ii) the progressive optical activation of the rare earth ions embedded in the matrix. As reported by Fei Lu et.al [22] the PL decrease at such high temperatures might be due to a couple of effects: (i) the Er ion diffusion causing an aggregation involving the rare earth to some extent, with possible concentration quenching effect responsible for PL signal degrading; (ii) the 1100°C annealing causing great change in the constitution of the GaN film, which exerts a negative effect on the Er luminescence.

In the case of *ErGaN5* and *ErGaN10*, the PL intensity decrease at 1100°C is definitely due to the high implantation dose, which enhances the effect of diffusion and aggregation processes for the rare earth ions.

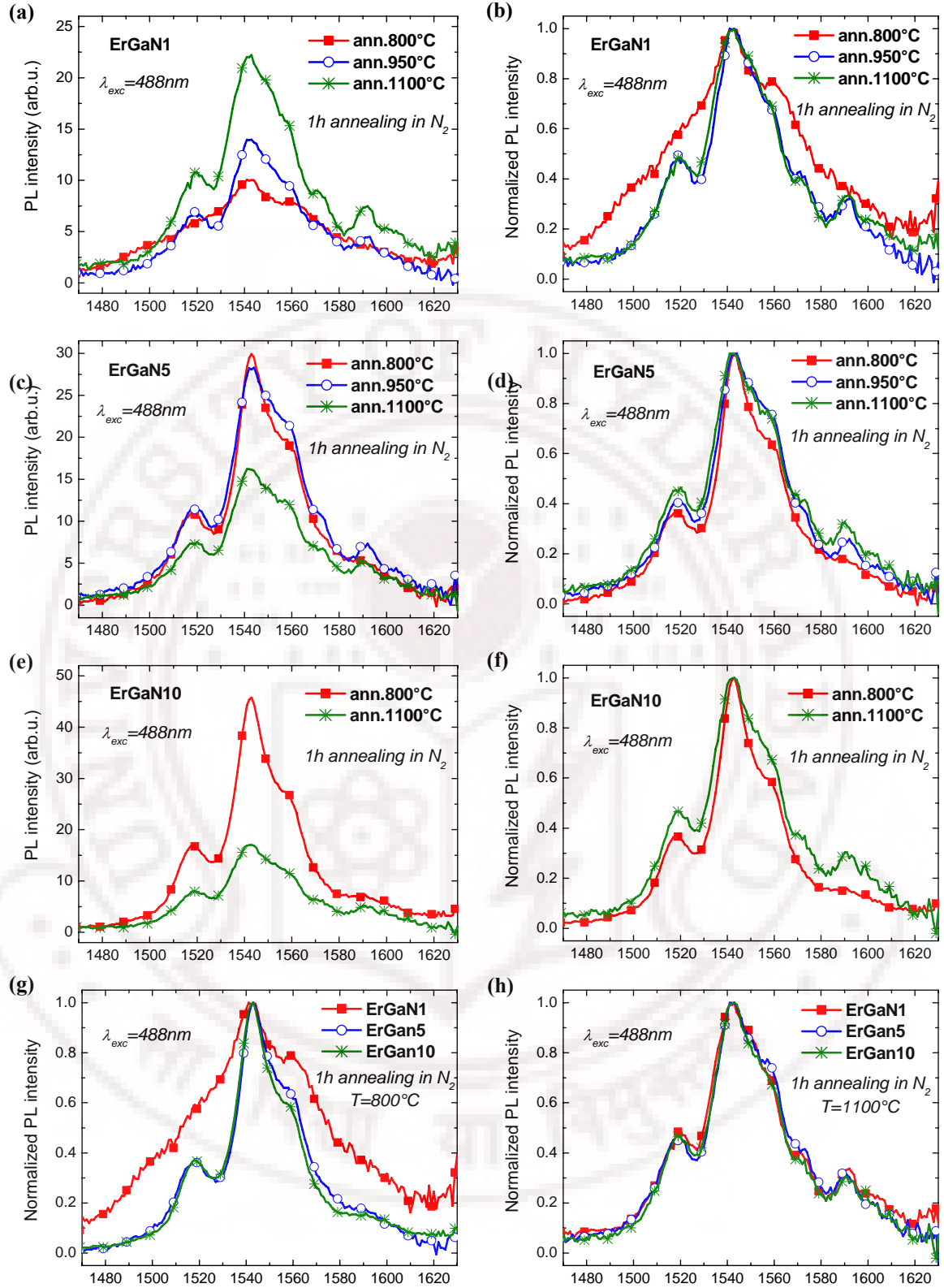


**Fig.5.4.** PL analysis by 488nm Ar laser excitation: PL spectra and normalized ones after annealing at different T for *ErGaN1* ((a) and (b), respectively) *ErGaN5* ((c) and (d)) and *ErGaN10* ((e) and (f)) series. Normalized spectra comparison for samples annealed at  $T=800^\circ\text{C}$  (g) and  $T=1100^\circ\text{C}$  (h).

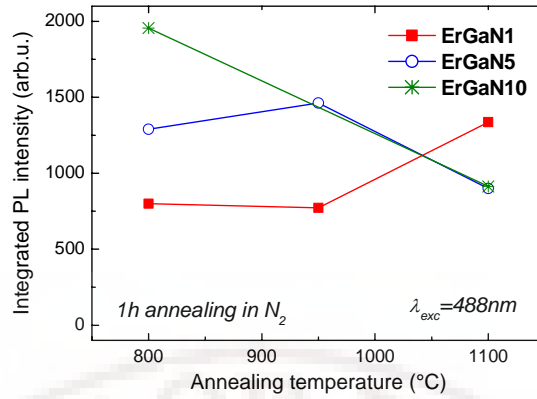


**Fig.5.5.** Annealing temperature dependence of the integrated PL intensity, as determined from the spectra of Figs.5.4 (a)-2(c)-2(e), for the *ErGaN1*, *ErGaN5* and *ErGaN10* series.

### 5.1.3 Mechanism for the excitation of the PL emission process

The analysis of the PL excitation spectra provides important information regarding the mechanism for the Er ion photostimulation. The spectra of Figs.5.6 (a)&(b) have been obtained by means of a tunable Xe lamp, emitting in the NUV-visible region. They give the possibility to make a comparison between samples belonging to different series (*ErGaN1* and *ErGaN10*) treated at different annealing temperature (800 and 1100°C). At first we notice that the PL emission in the NIR can be continuously stimulated in the whole excitation range, even by pumping at wavelengths where the Er ions are typically transparent. This clearly indicates an indirect excitation path linked to the interaction with the GaN matrix. Moreover, we observe deep modification by varying the temperature, while similar spectra for samples of different series treated in the same annealing conditions. For instance, the 1100°C annealed films show a main structure peaked at around 360nm which probably corresponds to the edge of the GaN band gap (~3.4eV). However we can't exclude that this feature is connected to a direct rare earth absorption process involving the transition into one of its excited states, as the  $^4I_{15/2} \rightarrow ^4G_{11/2}$  transition (~3.3eV). At the lower energies (larger wavelengths) the 1542nm PL signal is evidently weakened, even though the ErGaN system remains continuously photoexcitable, with such a band peaked at around 530nm: this feature is presumably linked to the PL emission originating from the rare earth excitation to one of the higher-lying energy levels in the green region, like the  $^2H_{11/2}$  state (~2.3eV), typically characterized by large excitation cross section values.

The two samples treated at 800°C still show the structure (probably) linked to the edge of the semiconductive gap (more evident for *ErGaN1-800°C*), whereas going towards the UV we observe a manifest loss in efficiency for the activation of the NIR PL signal. Furthermore the excitation spectra present a new band structure located at around 410nm: this can be linked to the presence of such a sub-band gap energy level related to a defective site in the GaN structure, or to the occurrence of the Er ion photostimulation to a further excited state, like the  $^2H_{9/2}$  energy level (3.0eV). Figs.5.6 (c)&(d) allow a comparison between normalized PL spectra obtained by using two different Ar laser lines for ErGaN system excitation. It is demonstrated that the emission shape is not affected by the pumping conditions, even by exciting the rare earth in resonance (at 488nm) or in out-of-resonance (at 476.5nm) configurations.

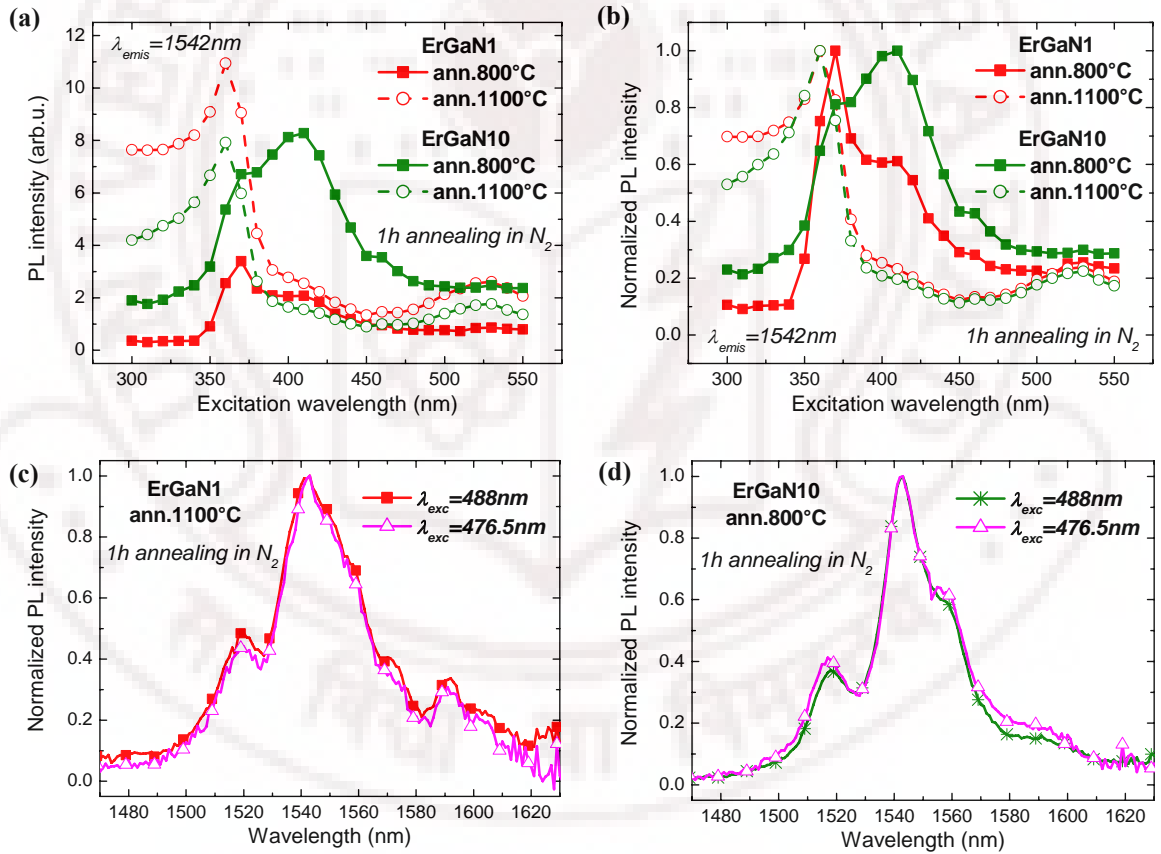


**Fig.5.6.** PL excitation spectra (a) and normalized ones (b) for the samples treated at 800°C and 1100°C, belonging to the series *ErGaN1* and *ErGaN10*; sample stimulation has been realized by using a broad emitting Xe lamp coupled to a monochromator. Normalized PL spectra comparison for the samples *ErGaN1\_1100°C* (c) and *ErGaN10\_800°C* (d) by Ar laser 488nm resonant and 476.5nm non-resonant pumping.

#### 5.1.4 Dynamics of the PL emission process

Through time-resolved PL experiments, we have studied the dynamics of the Er emission process in the NIR regions. Fig.5.7 shows the PL decay transient at 1542nm measured for all the samples, giving a comparison at different annealing temperature for the series *ErGaNI*, *ErGaN5* and *ErGaNI0*. The main evidence is that the observed curves follow a non-exponential trend and well described by a stretched exponential function of the form

$$I_{PL}(t) = I_{PL}(0)e^{\left[-\left(\frac{t}{\tau}\right)^\beta\right]} \quad (5.1)$$

where  $\tau$  is the PL lifetime and  $\beta$  represents the stretching factor, which ranges between 0 and 1. It is worth considering that this kind of transient behaviour is observed for all the investigated samples and this effect can be related to some fluctuations in the Er ion environment, incorporation in the GaN matrix, giving a spread in the probability for the de-excitation process. Therefore the  $\beta$  factor quantifies the dispersion in the relaxation rate and the observed time-resolved PL curves represent a convolution of the different excited state lifetimes related to the entire optically active Er ion population.

So we define the following effective transient time  $\tau_{eff}$  to characterize the PL dynamics for the ErGaN system.

$$\tau_{eff} = \frac{1}{I_{PL}(0)} \int_0^\infty I_{PL}(t) dt \quad (5.2)$$

where  $I_{PL}(t)$  is the luminescence intensity as a function of the time. According to Eq.5.1 and Eq.5.2 and considering the definition of the  $\Gamma(x)$  function,  $\tau_{eff}$  can be determined from the fitting parameters  $\tau$  and  $\beta$  using the relationship.

$$\tau_{eff} = \frac{\tau}{\beta} \Gamma\left(1/\beta\right) \quad (5.3)$$

From the analysis of the time-resolved PL curves of the samples studied as shown in Fig.5.7, we find that the  $\tau_{eff}$  values are around 1-1.5 ms, except for *ErGaNI-800°C* which shows a longer  $\tau_{eff}$  of  $\sim 3$  ms (see Fig.5.8). It is worth considering that the typical



$^4I_{13/2} \rightarrow ^4I_{15/2}$  transition lifetime for Er ions in dielectrics are of the order of 10 ms, whereas polymeric hosts are characterized by decay time in the  $\mu\text{s}$  range. It is clear that the nature of the matrix and environment surrounding the rare earth are strongly affecting the dynamics for the de-excitation processes.

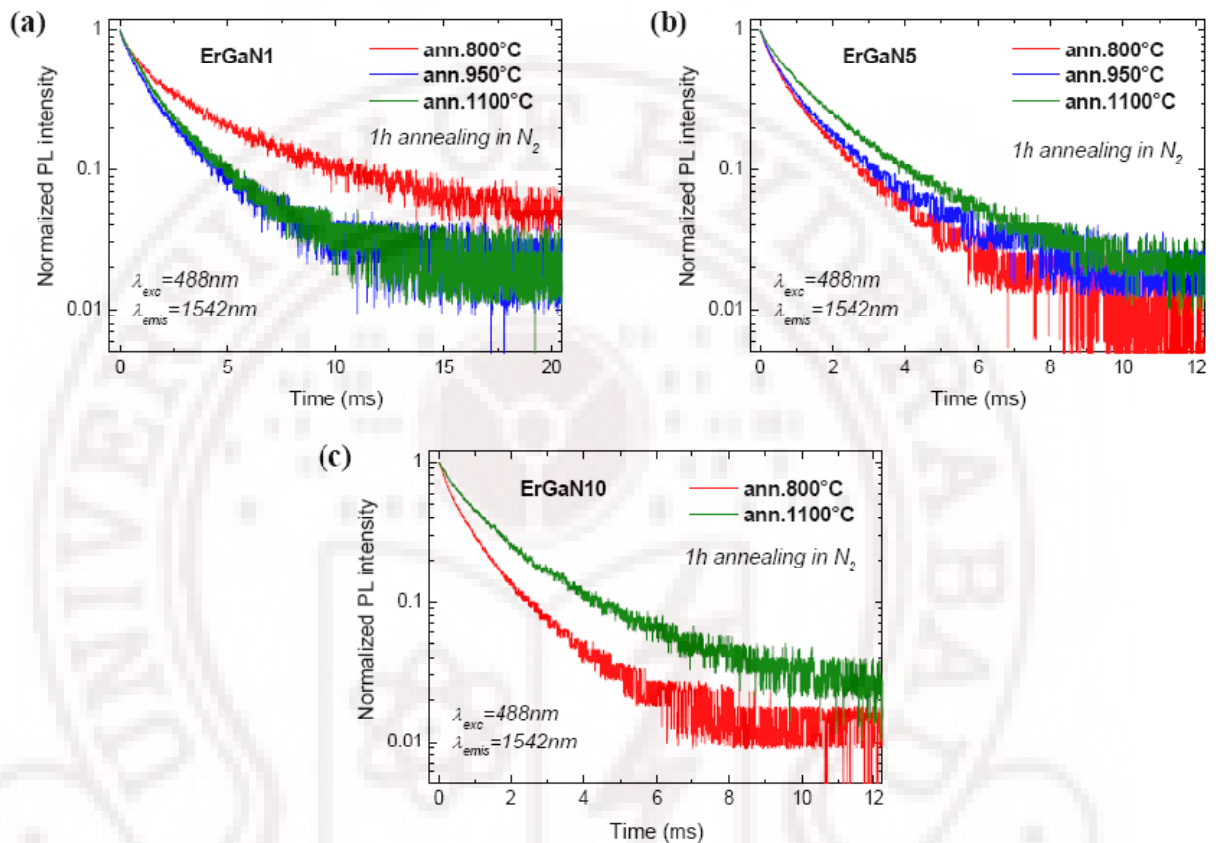


Fig 5.7 Time-resolved PL decay curves taken at 1542 nm for the series ErGaN1 (a) , ErGaN5 (b) and ErGaN10 (c). Pumping source is the 488 nm line of an Ar laser.

In Fig.5.8, we observe that a  $\tau_{eff}$  increases with increase in annealing temperature, which may be due to the recovery of the implantation damaged matrix and reduction of the impact of non-radiative processes related to the defective sites. Also, we studied the spontaneous lifetime characterizing the PL relaxation processes is determined by radiative and non-radiative events for  $^4I_{13/2} \rightarrow ^4I_{15/2}$  transition, and follows a relation given by

$$\frac{1}{\tau} = \frac{1}{\tau_{rad}} + \frac{1}{\tau_{n-rad}} \quad (5.4)$$



where  $\tau_{rad}$  and  $\tau_{n-rad}$  include all the radiative and non-radiative terms, respectively. In absence of non-radiative events, the spontaneous lifetime should match the pure radiative term, as in the (ideal) case of a completely isolated emitting ion. In ErGaN system, the presence of a surrounding matrix implies the occurrence of alternative relaxation channels faster than (and competing with) the direct emissive de-excitation process. Since it is well known that the implantation process generates defective sites constituting non-radiative centers for the Er ions (typically observed for glassy systems), it can be finally pointed out that the observed lifetime increase derives from a reduction of non-radiative relaxation process connected to the progressive matrix recovery promoted by the heat treatment.

In this context, the fact that *ErGaN1* shows larger lifetime values with respect to the other two series, can be related to a lower Er doping dose and to a lower damage level for the implanted matrix. *ErGaN1-800°C* shows a completely different spectral shape with respect to the other sample so that we can hypothesize that the Er ions are located in a structural site characterized by a slower overall relaxation dynamics.

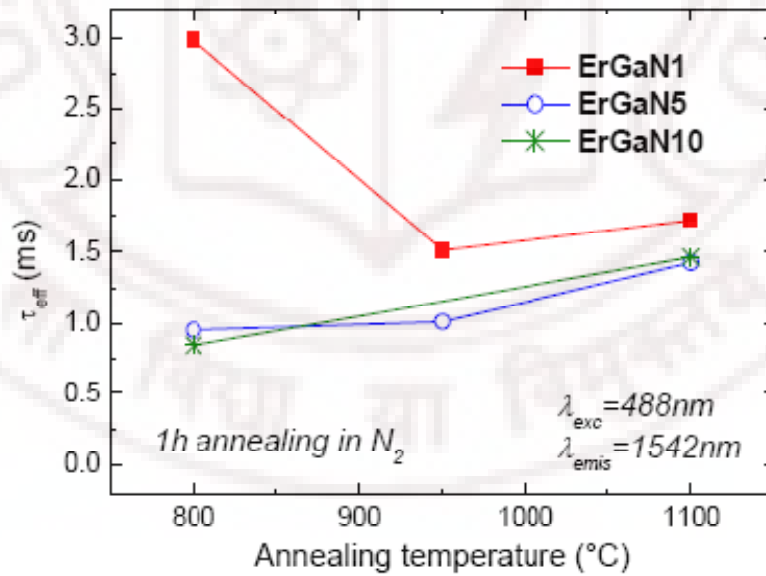


Fig 5.8 Annealing temperature dependence of the effective lifetime  $\tau_{eff}$  for all the series of samples.

### 5.1.5 Estimation of the effective Er excitation cross section

Since, PL excitation measurements suggest the activation of an indirect excitation path for Er ions embedded in GaN, it can be pointed out that the interaction with the semiconductor matrix has a significant impact on the physics related to the rare earth optical properties. An important parameter associated to the efficiency of the overall PL process is the effective cross section  $\sigma_{eff}$  for Er ion photostimulation mediated by the GaN host. Thus, we calculated the  $\sigma_{eff}$  for our Er implanted samples.

In general, the PL intensity for the  $^4I_{13/2} \rightarrow ^4I_{15/2}$  transition follows the relationship

$$I_{PL} \propto \frac{N^*}{\tau_{rad}} \quad (5.5)$$

where  $N^*$  is the concentration of the excited Er ions and  $\tau_{rad}$  is the pure radiative lifetime for the decay from the first excited level to the ground state.

In continuous pumping condition, the Er concentration  $N^*$  can be obtained by assuming that the relaxation time from the higher lying energy states are extremely short compared to the lifetime of the  $^4I_{13/2}$  metastable level. So, considering a simple two-level scheme describing the Er ion system, the population rate of the  $^4I_{13/2}$  level can be expressed by the following first order differential rate equation [23, 24].

$$\frac{dN^*}{dt} = \sigma_{eff} \phi (N_{act} - N^*) - \frac{N^*}{\tau} \quad (5.6)$$

where  $\sigma_{eff}$  is the effective rare earth excitation cross section,  $\phi$  is the photon flux of the optical pumping source,  $\tau$  is the excited state lifetime and  $N_{act}$  is the total concentration of the optically active Er ions given by

$$N_{act} = N_{Er} f_{act} \quad (5.7)$$

with  $N_{Er}$  is the rare earth concentration ( $N_{Er} \geq N_{act} \geq N^*$ ), proportional to the implantation dose, and  $f_{act}$  is fraction of the optically active ions ( $0 \leq f_{act} \leq 1$ ). It is important to underline that in the previous equation the occurrence of non-linear effects such as upconversion and excited state absorption have been neglected.

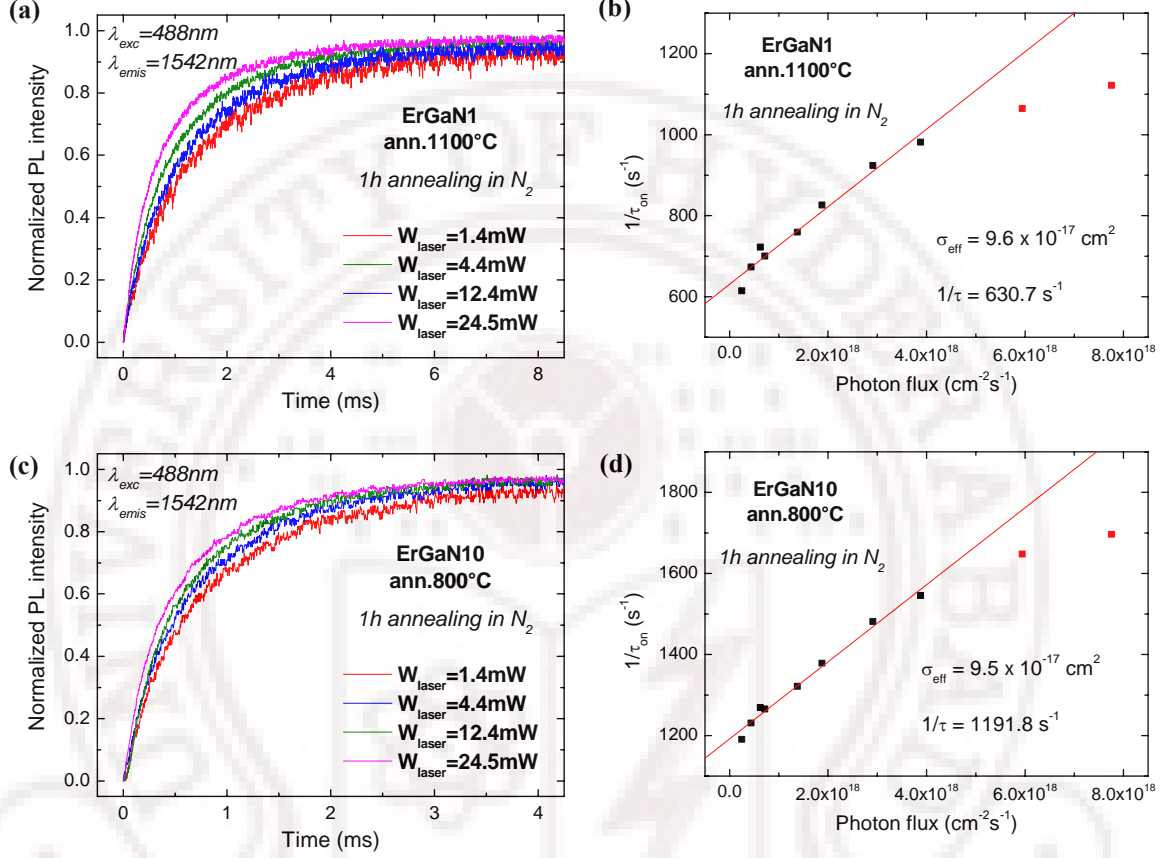


**Fig.5.9.** 1542 nm PL rising curves at different laser power, normalized at the steady state emission ( $t \gg 0$ ), and inverse of the risetime  $\tau_{on}$  as a function of the exciting photon flux for *ErGaN1-1100°C* ((a) and (b) respectively) and *ErGaN10-800°C* ((c) and (d)). The continuous lines in (b) and (d) are the linear fit of the  $1/\tau_{on}$  values done in order to estimate the Er ion excitation cross section  $\sigma_{exc}$  from Eq.5.9.

Using Eq. 5.5 and Eq.5.6 and assuming that the light source is turned on at  $t=0$ , we obtain that the PL intensity grows up according to the law

$$I_{PL}(t) = I_{PL}^S \left\{ 1 - \exp \left[ - \left( \sigma_{eff} \phi + \frac{1}{\tau} \right) t \right] \right\} \quad (5.8)$$

where  $I_{PL}^S$  represents the steady state PL intensity. Therefore the risetime  $\tau_{on}$  can be expressed as

$$\frac{1}{\tau_{on}} = \sigma_{eff}\phi + \frac{1}{\tau} \quad (5.9)$$

So the effective excitation cross section can be estimated by evaluating the  $\tau_{on}$  dependence from the pumping photon flux. We have followed this approach for the samples *ErGaN1-1100°C* and *ErGaN10-800°C*. Figs.5.9 (a)&(c) show the typical time evolution of the 1542 nm emission signal when the laser is turned on and these curves have been recorded by 488 nm pumping at different laser powers and the corresponding risetime  $\tau_{on}$  has been estimated from PL transients fitting procedure.

These quantities have been plotted in Figs.5.9 (b)&(d) as a function of the photon flux. We observe a linear dependence with the laser photon flux (at least at the lowest  $\phi$  values). Then using Eq.5.9 in conjunction with the slope of the fitting curve, we obtain for the two samples, a similar Er ion effective cross section  $\sigma_{eff}$ , which is around  $0.9-1.0 \times 10^{-16} \text{cm}^2$ . From the  $1/\tau$  fitting parameter, we obtain lifetime parameters of 1.59 and 0.84 ms for *ErGaN1-1100°C* and *ErGaN10-800°C* respectively which are in good agreement with the ones directly obtained from the PL decay curves. The typical absorption cross sections in the visible for Er ions in dielectrics are of the order of  $10^{-20}-10^{-21} \text{cm}^2$ . This demonstrates that there is an improvement of the efficiency for the rare earth photostimulation process through the interaction with the semiconductor host, resulting in a manifest activation of the Er PL emission process in the NIR.

### 5.1.6 Optical activation of the Er ions

Finally we have calculated the parameters that determine the whole optical response for the ErGaN system. Table.5.1 gives the main quantities characterizing its PL activity, as determined from the above discussed PL spectra and time decay curves. In general, by c.w. laser excitation and in low pumping power regime, the rare earth PL intensity  $I_{PL}$  in the NIR is given by:

$$I_{PL} \propto \sigma_{eff} \phi N_{Er} f_{act} \frac{\tau}{\tau_{rad}} \quad (5.10)$$

Having used the same laser photon flux  $\phi$  during the PL parameter measurements and assuming reasonably that the radiative lifetime  $\tau_{rad}$  is not affected by implantation and/or annealing conditions, we can define a figure-of-merit based on the ratio between PL intensity and lifetime (for our samples: integrated  $I_{PL}$  and  $\tau_{eff}$ ), normalized for the implantation dose, which should depend only on  $f_{act}$  and  $\sigma_{eff}$ .

$$\frac{I_{PL}}{\tau} \times \frac{1}{Er \text{ dose}} \propto \sigma_{eff} f_{act} \quad (5.11)$$

For each series, the evolution with the annealing temperature for the Er dose normalized  $I_{PL}/\tau$  ratio has been calculated from the data reported in Table.5.1 and plotted in Fig.5.10.

**Tab.5.1.** PL parameters for all the samples studied

Sample		PL intensity			Lifetime at 1542nm			Er dose norm. $I_{PL} / \tau_{eff}$ (arb.u.)
		peak $I_{PL}$ ex 488 (arb.u.)	peak $I_{PL}$ ex 476.5 (arb.u.)	Int. $I_{PL}$ ex 488 (arb.u.)	$\tau$ (ms)	$\beta$	$\tau_{eff}$ (ms)	
<i>ErGaN1</i>	<i>as-impl.</i>	0	0	0	-	-	-	-
	<i>800°C</i>	10.1	12.6	800.0	2.07	0.62	2.99	267.9
	<i>950°C</i>	14.0	14.2	772.0	1.21	0.71	1.51	510.4
	<i>1100°C</i>	22.2	22.0	1336.2	1.46	0.76	1.72	778.0
<i>ErGaN5</i>	<i>as-impl.</i>	0	0	0	-	-	-	-
	<i>800°C</i>	29.9	37.3	1289.2	0.72	0.67	0.96	269.8
	<i>950°C</i>	28.3	31.0	1462.2	0.78	0.68	1.02	288.0
	<i>1100°C</i>	16.2	15.9	900.4	1.17	0.73	1.43	126.2
<i>ErGaN10</i>	<i>as-impl.</i>	0	0	0	-	-	-	-
	<i>800°C</i>	45.8	65.6	1956.0	0.68	0.71	0.85	230.3
	<i>1100°C</i>	17.0	16.7	913.1	1.20	0.73	1.47	62.3

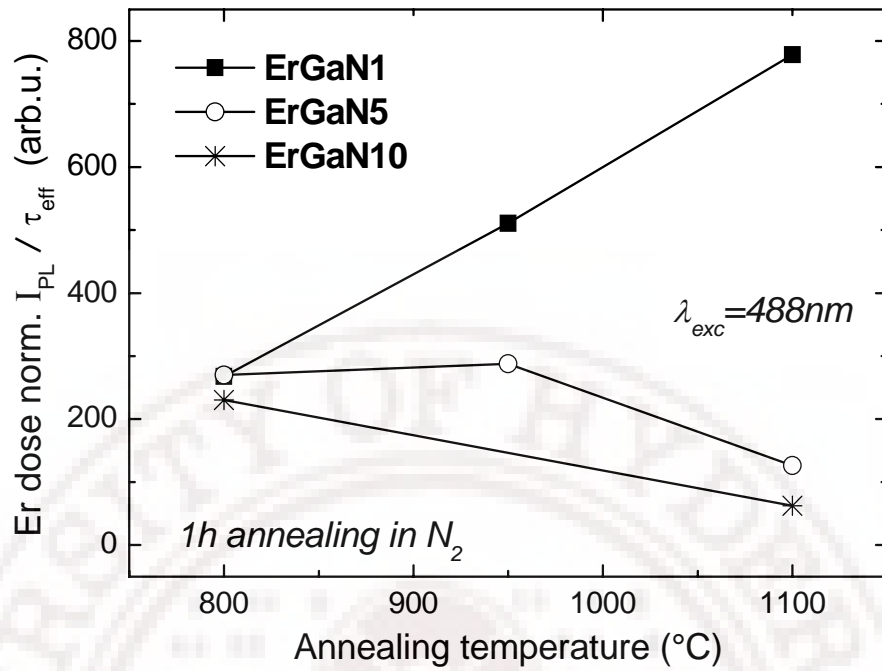


**Fig.5.10.** Annealing temperature dependence of the figure-of-merit defined in Eq.5.11, derived from the ratio between the  $I_{PL}$  and  $\tau_{eff}$  values normalized for the Er dose, for the series.

## 5.2 RBS/Channelling Lattice site location studies

### 5.2.1 ErGaN1

In this sample we did not observe any Er signal as the dose of implantation is very small. The typical PL spectrum of ErGaN-1100 sample is same as the other series (ErGaN5 & ErGaN10) 1100 annealed samples. So the RBS/Channeling measurements on the other sample will give insight into the ErGaN1 series. Normal axis  $\langle 0001 \rangle$  spectrum is shown in Fig 5.11 where we observed very good  $\chi_{min} \sim 4.2\%$ . This shows that the annealing at  $800^\circ\text{C}$  has resulted in full recovery of GaN matrix. As it is seen from the RBS spectra that implantation induced damages are negligible in these samples, one can attribute this fact and lower Er concentration for the observed better figure of merit from PL measurements on these set of samples. Also it has been reported that as implanted Er preferentially goes to the Ga substitutional site [25, 26].

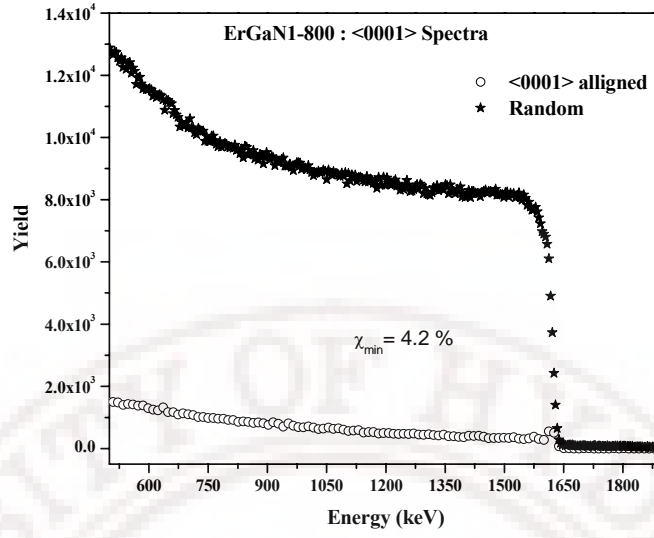


**Fig 5.11** RBS Spectra of the <0001> axial channeling of ErGaN1-800

### 5.2.2 ErGaN5

Fig 5.12 shows the random and aligned <0001> and <10-11> RBS spectra of the ErGaN5-800 sample. We notice that in <0001> & <10-11> axes, the  $\chi_{\min}$  is 10% & 69% respectively. This may be due to the higher implantation dose and lower annealing temperature. The direct scattering from the implanted regions indicates the presence of defects in these regions. As we know that the effects of dislocations on this <0001> axis are small, so increase in  $\chi_{\min}$  must be due to the lattice damages created by implantations. This shows that at 800<sup>0</sup> C annealing the lattice recovery of GaN matrix is not complete at this temperature.

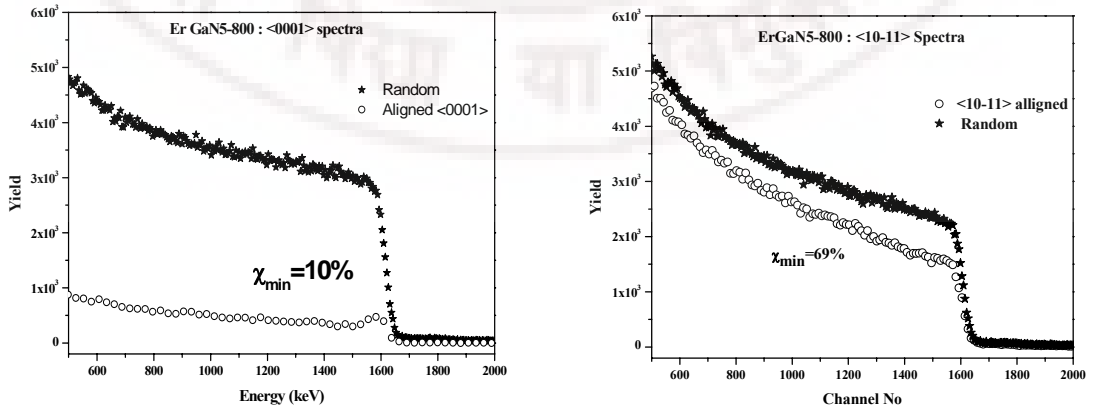


**Fig 5.12** Aligned and random RBS spectra along <0001> and <10-11> of the sample ErGaN5-800.



Channeling angular scans measured along  $\langle 0001 \rangle$  and  $\langle 10\text{-}11 \rangle$  for Er and implanted Ga regions are shown in the Fig 5.13. Normal axis angular scans show that Ga width is smaller than Er width, which is not expected generally. But the width of Ga and Er in  $\langle 10\text{-}11 \rangle$  axis is matching. This indicates that Er goes to substitutional Ga sites along and  $\langle 10\text{-}11 \rangle$  direction and Ga atoms are displaced inside the  $\langle 0001 \rangle$  channels. This may be attributed to the partial recovery of the GaN matrix. As reported earlier the as implanted Er preferentially goes to Ga substitutional site [25]. When the annealing temperature increases the Er ion tends to move to the interstitial sites.

The fraction of Er atoms displaced away from the lattice sites is calculated using the simple formula [27],

$$f_{dis} = \frac{\chi_{Er} - \chi_{Ga}}{1 - \chi_{Ga}} \quad (5.12)$$

The fractional Er atoms moving away from the channel is calculated to be 5.4% in  $\langle 0001 \rangle$  direction. As we know that  $\langle 0001 \rangle$  is having mixed atoms of Ga and N in row, but in  $\langle 10\text{-}11 \rangle$  it is separated. Narrowing of the angular dip occurs when the atoms are displaced by small distance ( $< 5 \text{ \AA}^0$ ) from the lattice sites. So here we see that along  $\langle 10\text{-}11 \rangle$  matching of Ga and Er signal widths, indicates that Er atoms are going to the Ga substitutional sites.

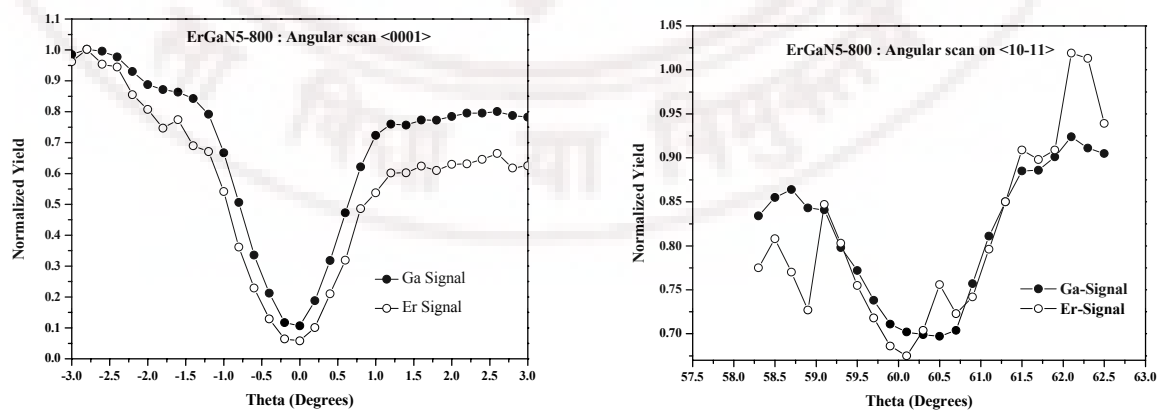


**Fig 5.13** Channeling angular scans of Er and Ga signal along  $\langle 0001 \rangle$  and  $\langle 10\text{-}11 \rangle$  axis

### 5.2.3 ErGaN10

In the higher implantation dose samples i.e. ErGaN10 series,  $\chi_{\min} \sim 30\%$  along  $\langle 0001 \rangle$  axis is very high for the  $800^\circ\text{C}$  annealing which decreases to  $13.2\%$  for annealing at  $1100^\circ\text{C}$ . This indicates better recovery of implantation induced damages in GaN matrix. For implanted regions the direct scattering and surface peaks are merged, since the Er ions damages the material heavily and the implanted region is very near to the surface (i.e. at depth of 30 nms from the surface). Fig 5.14 shows the angular scans along  $\langle 0001 \rangle$  axis of the Er and Ga atoms of ErGaN10-800 sample. When some of the Er atoms are having small displacement into the channel then we observed this kind of dip. Here majority of the dip is overlapped, but in the bottom, Er dip is narrowed. We have calculated the percentage of Er atoms displaced using the above formula. In this sample about  $15.6\%$  of Er atoms are displaced from the original Ga substitutional site.

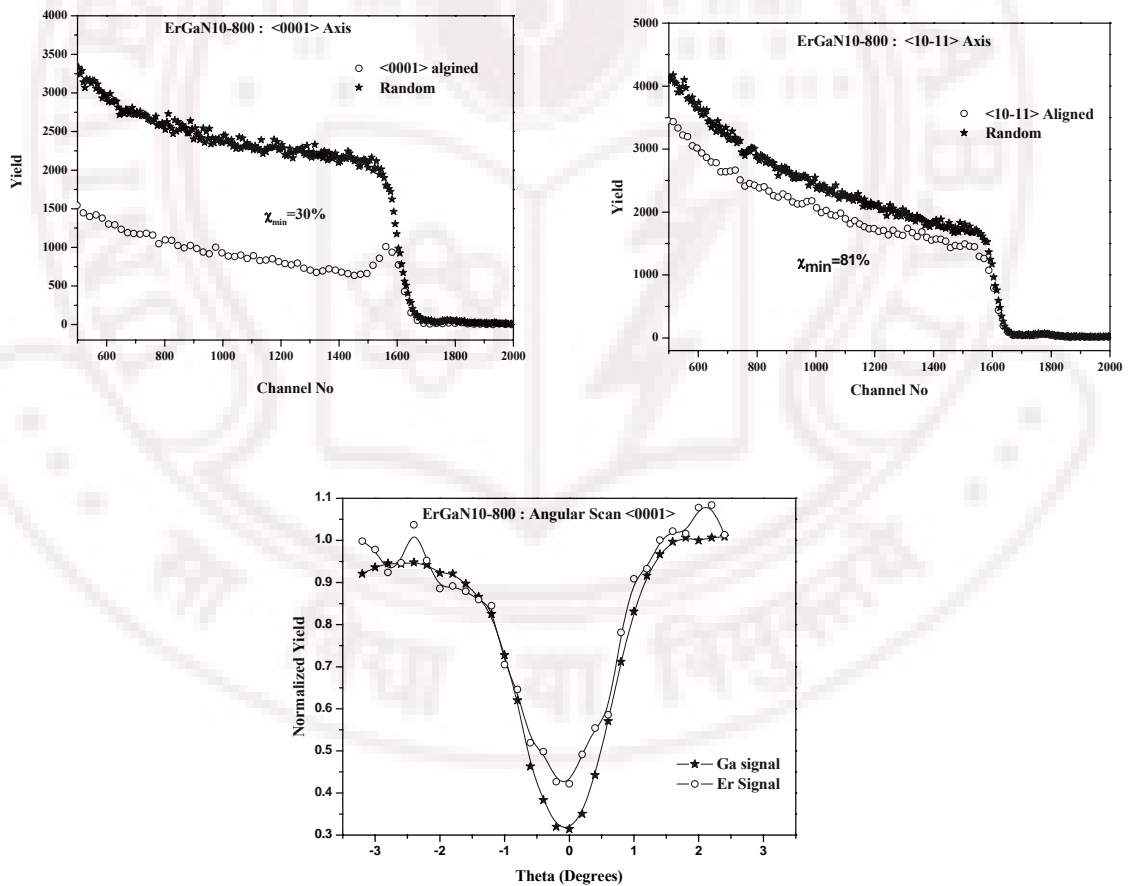


**Fig 5.14** RBS spectra and angular scans along  $\langle 0001 \rangle$  and  $\langle 10-11 \rangle$  axis of the sample ErGaN10-800

In the ErGaN10-1100 sample, we observed maximum recovery of GaN matrix. The  $\chi_{\min}$  in  $\langle 0001 \rangle$  and  $\langle 10-11 \rangle$  axis are reduced after 1100<sup>o</sup> C annealing (See Fig 5.15). Angular scans in the  $\langle 0001 \rangle$  shows that narrowing and higher  $\chi_{\min}$  of Er signal is due to the larger percentage of Er atoms, having large displacement ( $\sim 0.05$  nms) into the channel. In the  $\langle 10-11 \rangle$  direction the Er width is larger than the Ga width. This is due to the Er atoms' large displacement in the  $\langle 0001 \rangle$  direction. Our calculations show that  $\sim 52\%$  Er atoms are having large displacement into the channel i.e. moved towards the interstitial sites.

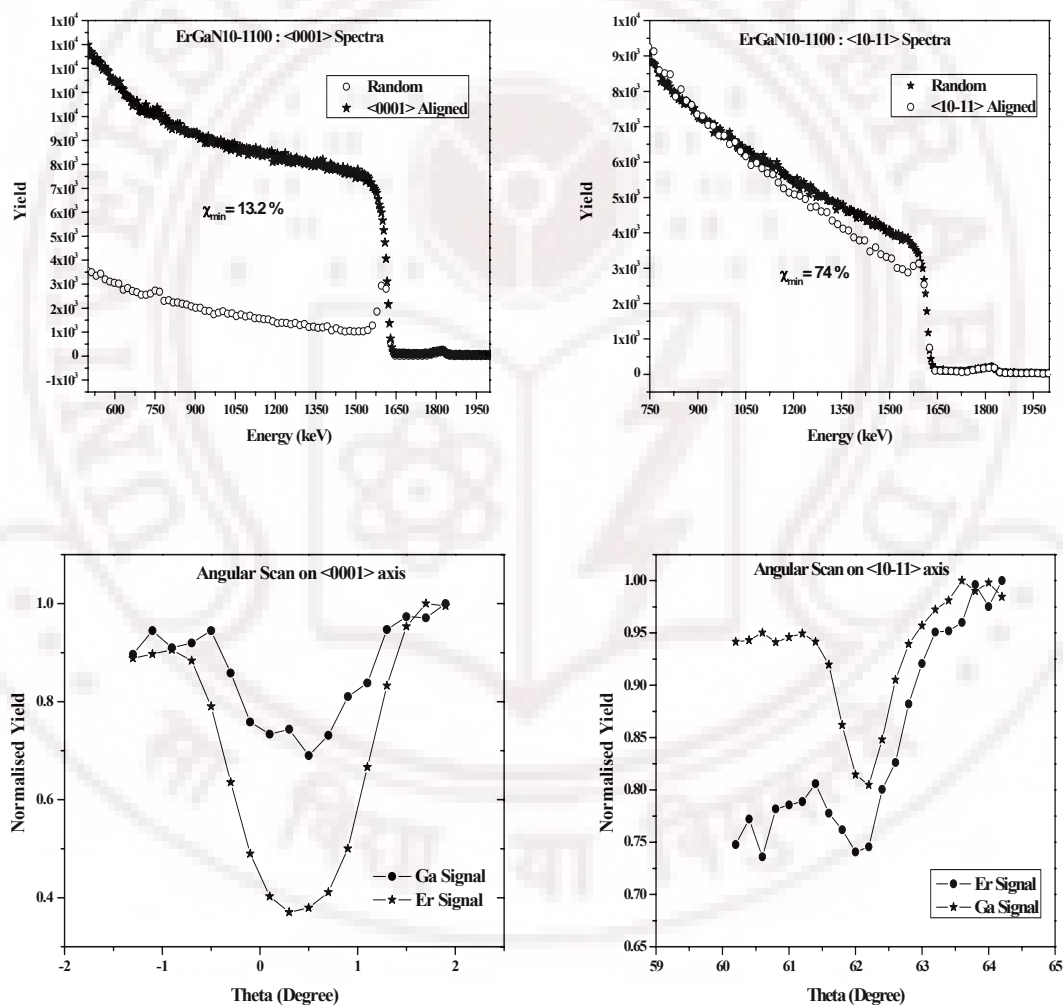


**Fig 5.15** (a) Random and aligned RBS/Channeling spectra on  $\langle 0001 \rangle$  and  $\langle 10-11 \rangle$  axis  
(b) angular scans along the  $\langle 0001 \rangle$  and  $\langle 10-11 \rangle$  axis. For the sample ErGaN10-1100

**Table 5.2:** Comparison of the main results of PL and RBS/Channeling measurements for different samples.

Sample		Int. I <sub>PL</sub> ex 488 (arb.u.)	$\tau_{\text{eff}}$ (ms)	Figure of merit	$\chi_{\text{min}}$ along <0001> (%)	% of Er atoms displaced $f_{\text{dis}}$ (%)
<i>ErGaN1</i>	800°C	800.0	2.99	267.9	4.2	-
	950°C	772.0	1.51	510.4	-	-
	1100°C	1336.2	1.72	778.0	-	-
<i>ErGaN5</i>	800°C	1289.2	0.96	269.8	10	5.4
	950°C	1462.2	1.02	288.0	-	-
	1100°C	900.4	1.43	126.2	-	-
<i>ErGaN10</i>	800°C	1956.0	0.85	230.3	30	15.6
	1100°C	913.1	1.47	62.3	13.2	52

### 5.3 Conclusions

After annealing, all the samples show Er NIR luminescence activation. The peak shapes show the typical  $^4I_{13/2} \rightarrow ^4I_{15/2}$  transitions with stark structures. Table 5.12 compares the main results of PL and RBS/Channelling measurements of all the sets of samples. We have analysed the observed behaviour for different samples using figure-of-merit and fraction of the displaced Er atoms. *ErGaN1\_1100°C* and *ErGaN10\_800°C* samples, which are doped with different Er amounts and annealed at different temperatures have very close excitation cross section ( $\sigma_{\text{eff}}$ ). So, excitation cross section is an intrinsic parameter of the ErGaN system and having weak dependence on the synthesis conditions. Now the figure of merit depends on temperature dependence of fraction of Er activated atoms ( $f_{\text{act}}$ ), rather than on the effective excitation cross section.

ErGaN10 series shows smaller figure-of-merit values than ErGaN5, which may be due to a higher Er doping level resulting in concentration quenching effects. The percentage of the Er atoms displaced from the symmetrical site is also high for the ErGaN10 series. As the concentration increases more Er atoms are moving towards the interstitial site, where Er-Er cross relaxation are favourable. Increase in annealing temperature drives higher

level of Er to interstitial sites, which results in reduction in the overall figure of merit parameter. The enhanced Er diffusivity at the high temperatures results in the reduction of activation in both the series. The effect of concentration is to increase the percentage of Er atoms going to the low symmetry sites from substitutional sites.

On the other hand *ErGaN* is having completely different behaviour. The figure of merit increases with increase in the temperature. This may be due to the low Er doping level, where concentration quenching effects can be limited. Also the less GaN damages drive the Er atoms in the perfect symmetrical sites. So, as the temperature is raised, it is possible that the progressive matrix recovery makes easier for an Er ion to arrange in a local structural site favourable for its optical activation, resulting in an optimization of the  $f_{act}$  parameter.

## References

- 1) B.R. Chalamala, R.H. Friend, T.N. Jackson, F.R. Libsch (Eds.), Flat-Panel Displays and Sensors – Principles, Materials and Processes, Mater. Res. Soc. Symp. Proc. 558(2000).
- 2) A.J. Steckl, J.M. Zavada (Eds.), Photonic Applications of Rare-Earth-Doped Materials, Mater. Res. Soc. Bull. 24 (1999) 9.
- 3) J. Heikenfeld, A.J. Steckl, Appl. Phys. Lett. 77 (2000) 3520.
- 4) D.S. Lee, J. Heikenfeld, R. Birkhahn, M. Garter, B.K. Lee, A.J. Steckl, Appl. Phys. Lett. 76 (2000) 1525.
- 5) X. Wu, U. Hommerich, J.D. Mackenzie, C.R. Abernathy, S.J. Pearton, R.N. Schwartz, R.G. Wilson, J.M. Zavada, Appl. Phys. Lett. 70 (1997) 2126.
- 6) K. Gurumurugan, H. Chen, G.R. Harp, W.M. Jadwisieniczak, H.J. Lozykowski, Appl. Phys. Lett. 74 (1999) 3008.
- 7) W.M. Jadwisieniczak, H.J. Lozykowski, F. Perjeru, H. Chen, M. Kordesch, I.G. Brown, Appl. Phys. Lett. 76 (2000) 3376.
- 8) V.I. Dimitrova, P.G. van Patten, H.H. Richardson, M.E. Kordesch, Appl. Phys. Lett. 77 (4) (2000) 478.
- 9) J.T. Torvik, C.H. Qiu, R.J. Feuerstein, J.I. Pankove, F. Namavar, J. Appl. Phys. 81 (9) (1997) 6343.

- 10) A.J. Steckl, M. Garter, R. Birkhahn, J. Scofield, Appl. Phys. Lett. 73 (17) (1998) 2450.
- 11) M. Garter, J. Scofield, R. Birkhahn, A.J. Steckl, Appl. Phys. Lett. 74 (2) (1999) 182.
- 12) R. Birkhahn, M. Garter, A.J. Steckl, Appl. Phys. Lett. 74 (15) (1999) 2161.
- 13) J. Heikenfeld, M. Garter, D.S. Lee, R. Birkhahn, A.J. Steckl, Appl. Phys. Lett. 75 (9) (1999) 1189.
- 14) J. Heikenfeld, D.S. Lee, M. Garter, R. Birkhahn, A.J. Steckl, Appl. Phys. Lett. 76 (11) (2000) 1365.
- 15) S. Coffa, L. Tsybeskov (Eds.), Silicon-Based Optoelectronics, Mater. Res. Soc. Bull. 23 (1998) 4.
- 16) G. Blasse and B. C. Grabmaier, Luminescent Materials, Springer; Berlin (1994).
- 17) R. Reisfeld, C. K. Jorgensen, Lasers and Excited States of Rare-Earths, Springer-Verlag, New York, (1977)
- 18) R. Birkhahn et al., J. Vac. Sci. Technol. B 17 (1999) 1195
- 19) J. T. Torvik, R. J. Feuerstein, J. I. Pankove, C. H. Qiu, and F. Namavar, Appl. Phys. Lett. 69 (1996) 2098.
- 20) M. Garter, J. Scofield, R. Birkhahn, and A. J. Steckl, Appl. Phys. Lett. 74 (1999) 182.
- 21) J. M. Zavada, S. X. Jin, N. Nepal, H. X. Jiang, J. Y. Lin, P. Chow, and B. Hertog, Appl. Phys. Lett. 84 (2004) 1061 .
- 22) Fei Lu et al., J. Phys. D: Appl. Phys. 37 (2004) 1544
- 23) Franzò et al., Appl. Phys A 69 (1999) 3
- 24) F. Enrichi et al., J. Appl. Phys. 96 (2004) 3925
- 25) K. Lorenz et al. Nucl. Instru. Methd. B 161 (2000) 946
- 26) E. Alves et al. Nucl. Instru. Methd. B 147 (1999) 383
- 27) Handbook of modern ion beam analysis, Ed J R Tesmer and Michel Nastasi, MRS, USA, (1995).

# CHAPTER VI

## **Dielectric function theory of stopping power of GaAs: An optical data model calculation**

During, recent years there has been considerable interest on compound semiconductors like GaN, InP and GaAs because of their applications in optoelectronics, high power and high temperature electronics and telecommunications. Ion beam technique plays major role in modification and characterization of these materials and hence in development of the related technologies. The main purpose and motivation of this work is to understand the process of swift heavy ion interaction in semiconductor materials for several applications. At present no single theory can explain observed results satisfactorily. To gain the fundamental understanding of the processes we need to perform detailed simulation of transport and energy loss. In the recent years use of optical data model and its extension to E-q plane with higher order correction has given fairly accurate description of the stopping powers for electrons and protons in energy range from few keV to several MeV, in some biological materials. It will be interesting to see the detailed MC simulation of charged particle transport in semiconductor materials. In particular, our group has been working on swift heavy ion interaction in GaAs, InP and GaN based multilayers, which are technologically important in the field of optoelectronics. We observed reduction of dislocation densities due to SHI irradiation in relaxed materials (i.e. beyond critical layer thickness). In the strained systems, it was found that the strain is modified during the ion irradiation and is decreasing with the increase in ion fluence. We also found that the SHI irradiation can induce a tensile strain in an initially lattice matched system [1-5]. To explain the observed results and to gain fundamental understanding, we would like to calculate the Stopping power of GaAs for protons and then extend it to swift heavy ions. These stopping power results are very useful in MC simulation of ion tracks in these materials. At present such optical data is available only for GaAs based materials so that we have reported results of our calculations for stopping powers for proton and Swift Heavy Ions in GaAs compound semiconductor. We hope to extend these calculations for the III Nitride materials like GaN, AlGaIn and InGaIn as and when such optical data becomes available for these.



## 6.1 Dielectric theory of stopping power

The knowledge of electronic stopping power of swift protons and ions are important in many applications. Bethe's theory represents the standard framework for calculating the SP above the Bragg peak [6-8]. At energies near the Bragg peak its accuracy decreases because of limitations of the first Born approximation and dipole approximation for the mean excitation and ionization energy. Shell corrections and the higher order corrections like Barkas and Bloch effects are important for reliable estimation of the SP using the Bethe's theory [9]. A successful methodology for heavy ion stopping is binary theory of Sigmund with the higher order and shell corrections [10]. An alternative method based on the first order Born approximation is to use the dielectric function of the materials [11]. The advantage of using the dielectric function theory is that, shell corrections applied to Bethe's theory are automatically included through the energy and momentum dependent dielectric function.

We start with the Maxwell's equations in vacuum, which are given by

$$\begin{aligned}\nabla \cdot E &= 4\pi\rho_e \\ \nabla \times E &= -\frac{1}{c} \frac{\partial B}{\partial t} \\ \nabla \cdot B &= 0 \\ \nabla \times B &= \frac{1}{c} \frac{\partial E}{\partial t} + \frac{4\pi}{c} J_e\end{aligned}\tag{6.1}$$

where  $\rho_e(r, t)$  and  $J_e(r, t)$  are charge and current densities respectively. When we apply the coulomb gauge, the field equations in terms of electromagnetic potentials are given as

$$\nabla^2 \phi = -4\pi \rho_e\tag{6.2}$$

$$\nabla^2 A - \frac{1}{c^2} \frac{\partial^2 A}{\partial t^2} - \frac{1}{c} \nabla \frac{\partial \phi}{\partial t} = -\frac{4\pi}{c} J_e\tag{6.3}$$

A general expression of charge density in terms of its Fourier components may be written as

$$\rho_e(r, t) = \int d^3 k \int d\omega \rho_e(k, \omega) e^{i(k \cdot r - \omega t)}\tag{6.4}$$

with similar expressions for  $J_e(r, t)$  and other fields. This charge and current density can be split into external and induced contributions in the material medium as,

$$\rho_e = \rho_{e,ext} + \rho_{e,ind} \quad (6.5)$$

$$J_e = J_{e,ext} + J_{e,ind} \quad (6.6)$$

where  $\rho_{e,ind}$  and  $J_{e,ind}$  are the response of the medium to the field. By applying the linear response and adopting the Ohms' law to the Eq 6.4. we can write induced charge density using the dielectric function:

$$\rho_{e,ind} = -\frac{k^2}{4\pi} [\epsilon(k, \omega) - 1] \phi(k, \omega) \quad (6.7)$$

where, the complex dielectric function is defined as

$$\epsilon(k, \omega) = 1 + \frac{4\pi i \sigma(k, \omega)}{\omega} \quad (6.8)$$

Now consider a point charge  $Z_1 e$  in uniform motion with a velocity  $v$  so that the external charge density and current density in Fourier space is given by

$$\rho_{e,ext}(k, \omega) = \frac{Z_1 e}{8\pi^3} \delta(\omega - k \cdot v) \quad (6.9)$$

$$J_{e,ext}(k, \omega) = \frac{Z_1 e}{8\pi^3} v \delta(\omega - k \cdot v) \quad (6.10)$$

The electric field is given by

$$E(r, t) = \int d^3k \int d\omega e^{i(k \cdot r - \omega t)} (-i k \cdot \phi(k, \omega) + i \frac{\omega}{c} A(k, \omega)) \quad (6.11)$$

In homogeneous, isotropic and infinite medium, the stopping force is directed opposite to velocity  $v$ . Hence, the energy loss function is given by

$$\frac{dE}{dx} = -\frac{Z_1 e}{v} v \cdot E(v, t) \quad (6.12)$$

Inserting the potential and fields we arrive at the following equation

$$\frac{dE}{dx} = -\frac{Z_1^2 e^2}{\pi v^2} \int_0^\infty k dk \int_{-kv}^{kv} \omega d\omega \frac{1/\varepsilon - v^2/c^2}{k^2 - \varepsilon \omega^2/c^2} \quad (6.13)$$

Fermi [12] was the first to derive the stopping power of solids using the Maxwell's equations. The quantum mechanics enters here through the complex dielectric function. Lindhard [12] later derived the dielectric function theory as universal tool.

## 6.2. The Method

In the present calculations we used the Dielectric Function Theory (DFT) within the framework of first born approximation. Here we used the Riche-Howie [14] formalism of the DFT theory of stopping power, According to Pines [15], when the charged particles move in solid with energy  $E$  and velocity it is characterized by the complex dielectric function. The basic quantity for any charged particle calculations is Differential Inverse Mean Free Path (DIMFP)  $d\lambda^{-1}/d(\hbar\omega)$  (which is proportional to stopping power), where  $\hbar\omega$  is the energy transfer to solids. We start with formula for stopping power of swift point charge in a condensed medium, which is derived from the first order dielectric function theory [16]

$$\frac{dE}{dx} = \frac{Z_1 \text{eff}^2}{\pi \alpha_0 T} \int \hbar\omega d(\hbar\omega) \int \frac{1}{q} \text{Im} \left[ \frac{-1}{\varepsilon(q, \omega)} \right] dq \quad (6.14)$$

where  $\alpha_0 = \hbar/me^2$  is Bohr radius, the kinetic energy  $T = mV^2/2$  with  $m$  as the electron rest mass and  $V$  as the projectile velocity,  $\varepsilon(q, \omega)$  is complex dielectric response function and  $\hbar\omega$  &  $q$  are energy and momentum transfer, respectively. Effective charge of projectile is given by

$$Z_1 \text{eff} = Z_1 \left[ 1 - e^{-\frac{\sqrt{\frac{2T}{M}}}{Z_1^{2/3} \sqrt{\frac{27.8}{m}}}} \right] \quad (6.15)$$

The limits of integration are given as [17]

$$q = \sqrt{\frac{2M}{\hbar^2}} \left( \sqrt{T} \pm \sqrt{T - \hbar\omega} \right) \quad \text{For ions} \quad (6.16)$$

In the Eq (6.14), the main material dependent parameter in Energy Loss Function (ELF) is the complex dielectric function. Experimentally it is not possible to measure the full range of  $\omega$  and  $q$  of interest. First we construct the ELF's from valence and inner shells. Valence shell contributions are modeled from the optical data of GaAs taken from optical measurements [18]. In the valence shell contribution, shell corrections proposed to Bethe's theory have been included selfconsistently. Inner shell contributions have been modeled from x-ray photoabsorption data available in NIST data base for *Ga* and *As* atoms [19].

Valence shell ELF is calculated from the following equation

$$\text{Im} \left[ \frac{-1}{\varepsilon(0, \omega)} \right]_{\text{Valence}} = \frac{2nK}{(n^2 - K^2) + (2nK)^2} \quad (6.17)$$

where  $n$  is refractive index and  $K$  is extinction coefficient

Inner shell ELF is calculated by

$$\text{Im} \left[ \frac{-1}{\varepsilon(0, \omega)} \right]_{\text{Inner}} = \frac{\omega_p^2}{8\pi Z \alpha \alpha_0 R} \sigma_{\text{Photo}} \quad (6.18)$$

where,  $Z$  is atomic number,  $\alpha$  is fine structure constant,  $R$  is Rydberg constant,  $\sigma_{\text{Photo}}$  is X-Ray photo-absorption coefficient and  $\omega_p = \sqrt{4\pi N e^2 / m}$  is free electron plasma energy and  $N$  electronic density.

The Calculated ELF's, Valence shell from the optical experiment data and Inner shell from X-Ray photo absorption data, were fitted with Eq (6.19) proposed by Ritchie and Howie [14]. A quadratic dispersion relation has been used to arrive at the dispersion relation.

Here the dispersion relation is plasmon like for small  $q$  and goes into free particle at large  $q$  values. This is more convenient form for extension to ELF in momentum space. The use of experimental optical data is that it includes all possible collective and single excitation effects. In this representation,  $A_i$ ,  $E_i$ , and  $\gamma_i$  correspond to the height, position and width of the respective transition peaks in the spectrum. After modeling the parameters of the Drude function, it has been checked for sum rule consistency.

However, for compound materials, not much experimental ELF data are available for high energy range. Therefore, we construct the ELF of a compound  $A_xB_y$  from the ELF of its elementary constituents, by applying additivity rule for respective ELF/ $n$  ratios, where  $n$  is the atomic or molecular density of the target. This rule is not applicable at low energies corresponding to the excitation of the valence electrons. However, it can be applied for energies comparable to those of the inner shells, since the external electrons participate in the formation of the compound, but inner shells are insensitive to this process.

$$\text{Im}\left[\frac{-1}{\varepsilon(q=0, \omega)}\right] = \sum_i \frac{A_i \gamma_i \hbar \omega}{(\hbar^2 \omega^2 - E_{0i}^2)^2 + (\gamma_i \hbar \omega)^2} \quad (6.19)$$

where

$$E_{0i}' = E_{0i} + (\hbar q)^2 / 2m \quad (6.20)$$

$E_{0i}$  is the characteristic energy of  $i^{th}$  oscillator,  $A_i$  is fraction of electrons which have energy  $E_{0i}$  and  $\gamma_i$  is the  $i^{th}$  energy damping coefficient.

We used the extended Drude model dispersion relation (Eq 6.20) for extension of the optical ELF into the momentum space. This model has been applied successfully to describe the dispersion of interband transition for many compound materials [17]. Emfietzoglou et.al, have reviewed [20] the available dispersion schemes in a recent article. Drude scheme was considered to be good only for free electron gas plasmon excitations like in metals. Akkerman et.al showed that it works well for semiconductors,

namely silicon. In our calculations, we have shown that the extended Drude type dispersion relation can be applied to compound semiconductors like GaAs.

The validity of the energy and momentum dependent ELF for full range of  $\omega$  and  $q$  is checked by the sum rules. This was originally proposed by Pines [15] for dielectric function  $\varepsilon(q, \omega)$ . Here we use the following sum rules to check the consistency of ELFs: (i) f-sum rule which gives the total valence electrons and (ii) the perfect screening sum rule, which goes to 1 as  $\hbar\omega \rightarrow \infty$

$$Z_{eff} = \frac{2}{\pi E_P^2} \int_0^\infty \hbar\omega \operatorname{Im} \left[ \frac{-1}{\varepsilon(0, \omega)} \right] d(\hbar\omega) \quad (6.21)$$

$$P = \frac{2}{\pi E_P^2} \int_0^\infty \frac{1}{\hbar\omega} \operatorname{Im} \left[ \frac{-1}{\varepsilon(0, \omega)} \right] d(\hbar\omega) + \frac{1}{n_0} = 1 \quad n_0 = 3.601 \text{ for GaAs} \quad (6.22)$$

The advantage of using Dielectric Function Theory (DFT) is that one can derive the mean ionization potential (I) from ELFs. This quantity has been used in Bethe's stopping power formula for heavy ions. The mean excitation and ionization energy of material can be expressed in terms of optical ELF as follows:

$$\ln(I) = \frac{\int_0^\infty \omega \ln(\hbar\omega) \operatorname{Im} \left[ \frac{-1}{\varepsilon(0, \omega)} \right] d(\hbar\omega)}{\int_0^\infty \omega \operatorname{Im} \left[ \frac{-1}{\varepsilon(0, \omega)} \right] d(\hbar\omega)} \quad (6.23)$$

### 6.3. Results and discussions

The experimental optical data which are used to model the valence shell contributions are taken from Ref [18] and inner shell contributions are taken from NIST X-ray photo-absorption data. ELFs of valence and inner shells are calculated using the Eq (6.17) & (6.18) respectively. As one can see, the valence shell contributions are pronounced till  $\sim 183$  eV. So we have considered the shells which are having binding energy higher than 183 eV as inner shells and all other shells are considered to be valence shells. Thus, we have 3 inner shells from Ga and 4 inner shells from As atoms.

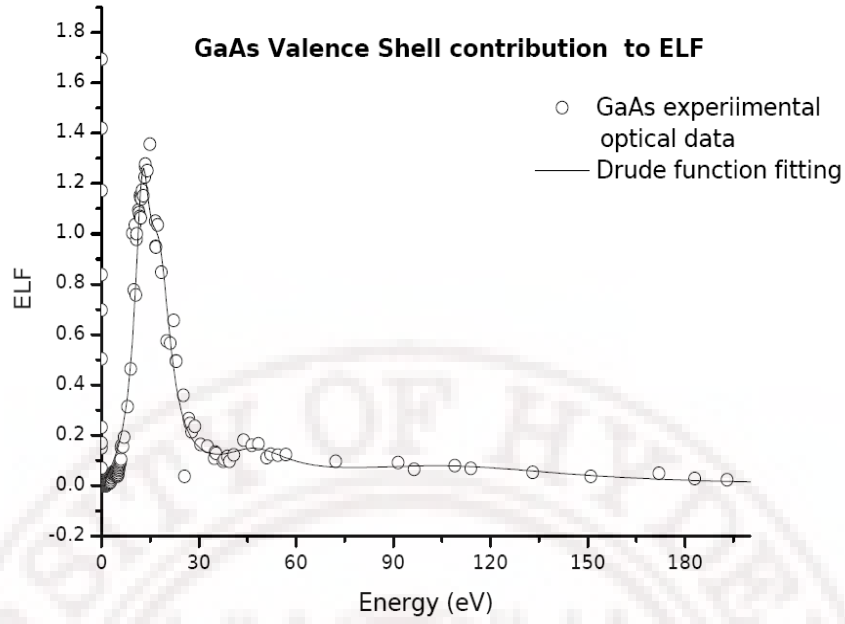


Fig 6.1. Extended Drude function fitting of valence shells contributions.

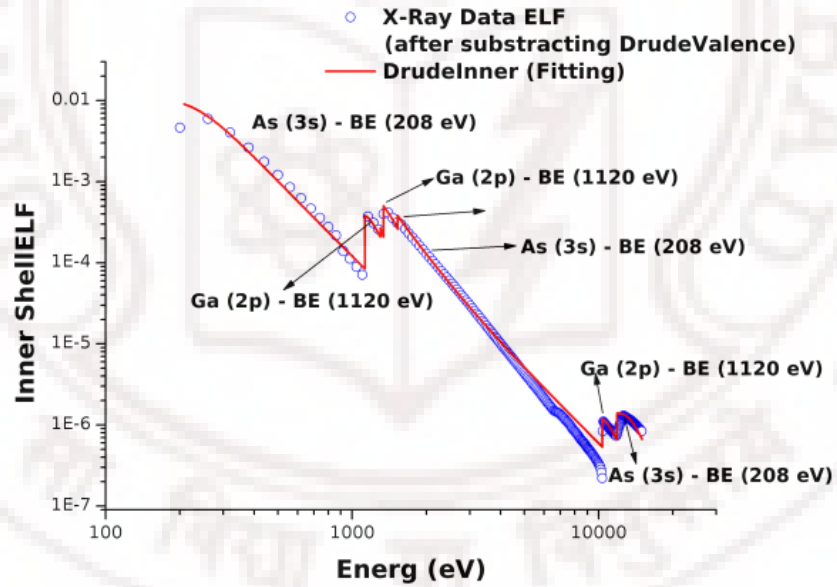


Fig 6.2. Extended Drude function fitting of inner shells contributions.

Figs.6.1& 6.2 show the fitting of valence and inner shell ELF's for extended Drude function at  $q=0$ . The solid line represents our fitting using Eq (6.19) and open circles are experimental data. Fig 6.1 is the ELF due to the valence shell electrons, whereas Fig 6.2



represents the ELF due to the excitations of inner shell electrons plotted in logarithmic scale. Our model function describes the sharp structures of valence and inner ELFs. It also models perfectly the effects like band gap transitions, collective plasma oscillations of valence electrons and single excitations of the inner shells. The parameter used in the fit of the valence shell contributions are given in the table 6.1. Sum rule also gives the satisfactory values; with f-sum rule value as 0.9899 which is close to unity. The perfect screening sum rule yields the value of 0.9337. Calculated  $I$  value is 379 eV which is close to 385 eV, the Bragg value for GaAs [21]. The characteristic of ELF structure shows, at low energies the transitions are inter-band and highest maximum is due to the excitation of volume plasmons.

Table 6.1 Parameters used to fit the optical ELF corresponding to the valence shell electrons.

<b>i</b>	<b><math>A_i</math></b>	<b><math>\gamma_i</math></b>	<b><math>E_i</math></b>
<b>1</b>	66.35	5.629	12.87
<b>2</b>	120.6	8.949	18.30
<b>3</b>	136.5	26.52	49.13
<b>4</b>	793	97.38	116.6

In fig 6.3, we plot the results obtained from our model for different values of momentum and frequency. It shows that, plasmon excitation is peaked around 10-30 eV for zero momentum transfer. When the momentum transfer increases, collective effects vanish and single excitations are pronounced. This has been clearly seen in our model since for  $q > 0$  the plasmon excitation peak weakens and shifts towards higher energy. Thus, the extended Drude type function and quadratic dispersion scheme can be used to model the compound semiconductors like GaAs.

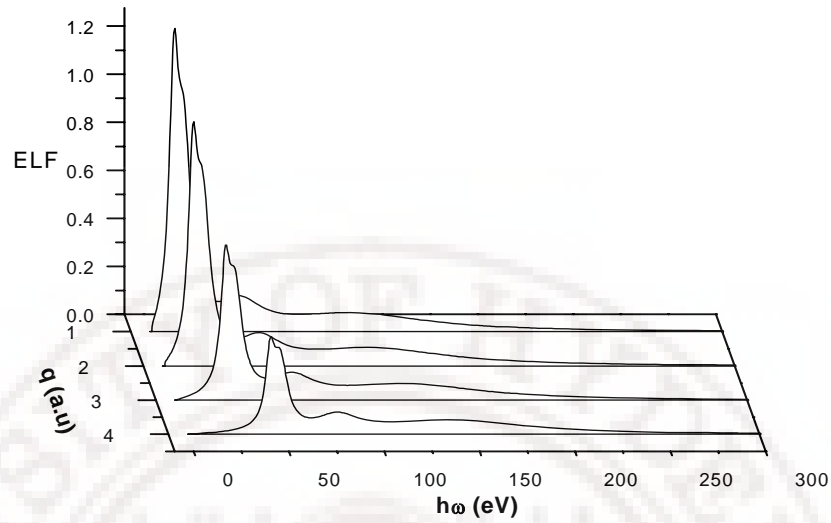


Fig 6.3. Plot of Drude function for different momentum and energy transfer.

### *Stopping of protons*

The SP of GaAs for Proton case is shown in Fig 6.4, where solid line is our calculated value, open circle is experimental data and dotted line is Heredia-Avalos et.al calculations. Our results are matching the experimental data [22] very well above the Bragg maximum in the high energy region. Heredia-Avalos et.al, [21] have used the CasP code to account for the projectile  $Z_1$  charge screening effects. They employed the Generalized Oscillator Strength (GOS) of atoms to calculate the inner shell contributions. At high energies the optical ELF are not available, so we used the Bragg's additive rule to calculate the compound materials ELF. Here we used the X-ray cross section data to account for the inner shell contributions to SP, which accounts for all possible single excitations of the inner shell electrons. Our model provides satisfactory results in Bragg peak tail and higher energies. The exchange effects are expected to dominate the low energy region which is not accounted in the DFT theory. But for proton case most of the contributions to SP come from the plasmon excitations. Even though we could not account for the charge exchange and electron capture processes, our results are in reasonably good agreement in high energy regions with the experimental values and other calculations.

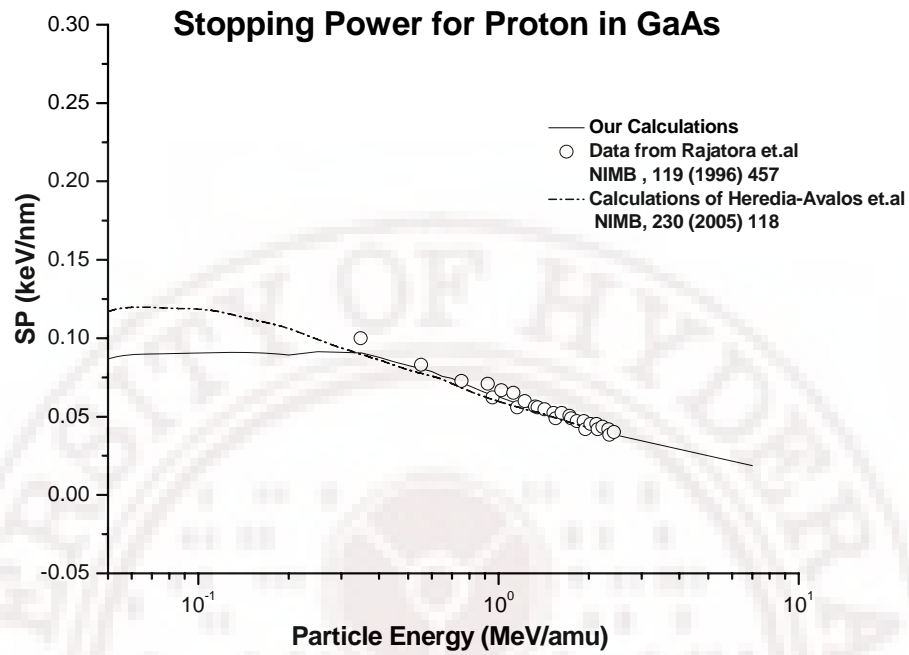


Fig 6.4. Energy loss of protons compared with experimental SP measurements.

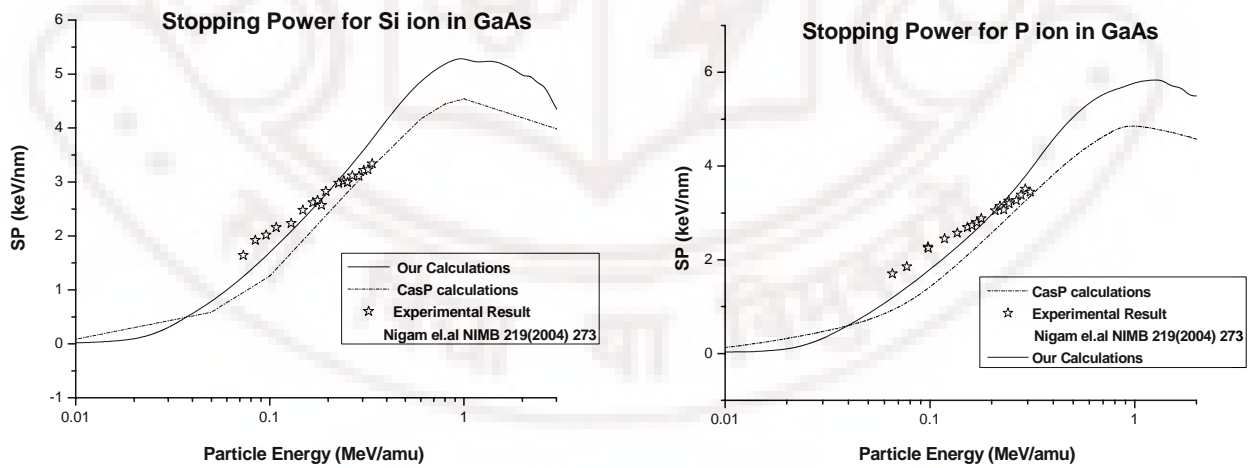


Fig 6.5. SP of GaAs for light ion compared with experimental SP measurements.

## Stopping of light and heavy ions

We have calculated the SP of GaAs for light ions (Si and P ions), for which experimental data are available in the lower energy regions [23]. In Fig 6.5, the calculated and experimental SP are plotted, for light ions. The calculation fits reasonably well with the experimental SP data. In these calculations, we used the mean equilibrium charge  $Z_{\text{eff}}$ , a standard Thomas-Fermi form proposed by Sigmund et.al [24]. This accounts for the projectile screening effects. As the incident particle mass increases the collective excitations of outer shells dominate. The modeled ELF from optical data of compound materials includes all the possible collective excitations. Generally zero momentum transfer inelastic collisions are characterized by the collective excitations and  $q > 0$  collisions are accounted for, by single excitations. We did not include the charge exchange effects,  $Z_1^3$  Barkas effect and Bloch corrections. These higher order correction play role at the Bragg peak and charge exchange effects dominates at low velocity. Because these effects are not included in the standard DFT model, our calculations deviate from the experimental values in the low energy regions and around the Bragg peak. Heavy ion stopping is shown in Fig 6.6. As per our knowledge there are no experimental data available for heavy ions. Our results have been compared with SRIM2003 [25] and CasP [26] code calculations. We note that our values are higher than the other code estimations in the high energy regions, which may be due the target electronic configurations. However the results converge to the other calculated values better in the below and above Bragg peak maximum energy regions.

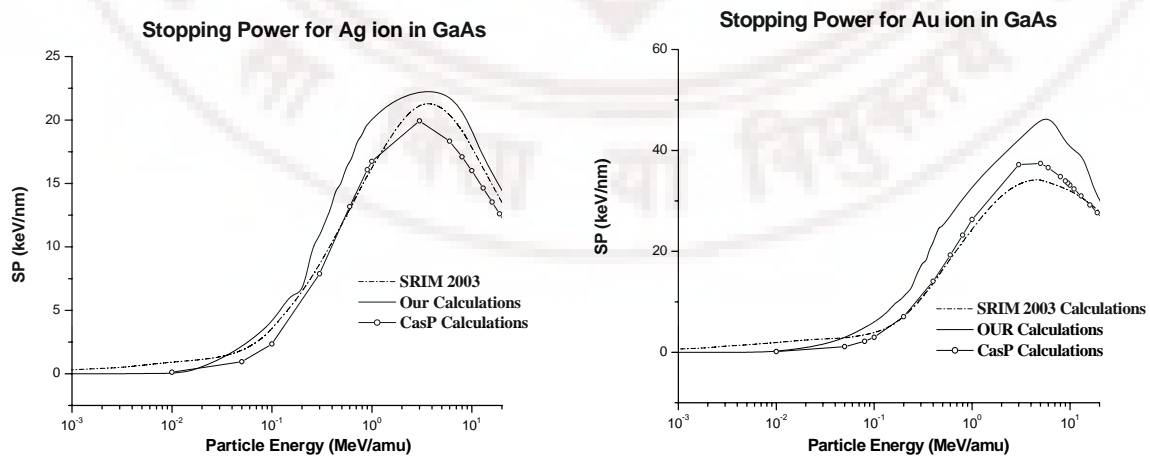


Fig 6.6. SP of GaAs for Heavy ion compared with SRIM 2003 and CasP calculations.

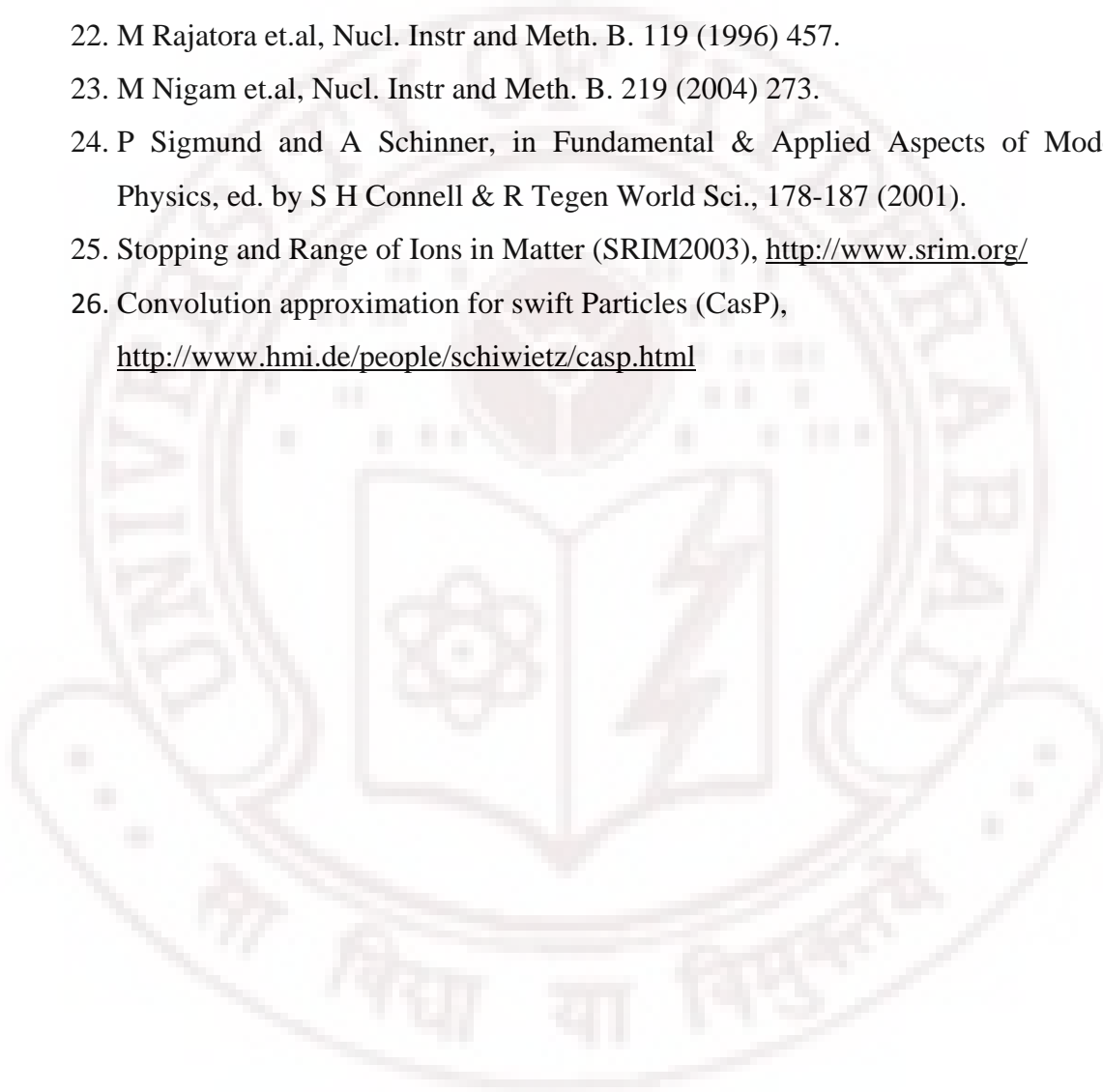
## 6.4. Summary and conclusions

We have presented results for the SP of GaAs for protons, light and heavy ions. These are technologically important materials and are used in high frequency devices and light emitting diodes. So the precise calculations of SP of these materials are important. Here we used extended Drude type function to model the ELF of GaAs within the framework of first order dielectric function theory. The known (experimental) Optical data were used for valence shell contributions and X-Ray photo absorption data were used for inner shell contributions. We have used the quadratic dispersion scheme to extend the ELF into momentum space. Our calculations fit reasonably for wide range of projectiles from protons to heavy ions like gold. It has been observed that, one needs to include the higher order correction for energies near Bragg peak maximum. Also our calculations fit well at high energy regions. Thus we conclude that one can use the extended Drude model and quadratic dispersion scheme with higher order corrections to model the compound semiconductors to calculate the stopping powers with reasonable accuracy.

## References

1. S V S Nageswara Rao et. al., Nucl. Instr. Meth. B 212(2003) 473.
2. Anand P. Pathak et. al., Nucl. Instr. Meth. B. 212 (2003) 442.
3. S V S Nageswar Rao et. al., Physics at Surfaces and Interfaces Ed. B N Dev World Scientific (2003) pp158-170.
4. S Dhamodaran et.al., Rad Effects & Defects in Solids, 162 (2007) 131.
5. N Sathish et.al., Vacuum, 82 (2008) 911.
6. H Bethe, Z. Physik, 76 (1932) 293.
7. U Fano, Ann. Rev. Nucl. Sci, 13 (1963) 1.
8. P Sigmund, Nucl. Instr. and Meth. B 135 (1998) 1.
9. P Sigmund, Nucl. Instr. and Meth. B 85 (1994) 541.
10. P Sigmund, Springer Tracts in Modern physics, 204 (2004).
11. R H Ritchie, Nucl. Instr. and Meth. 198 (1982) 81.
12. E Fermi, Phys. Rev, 57 (1940) 1242.
13. J Lindhard, Mat Fys Medd Dan Vid Selsk, 28 (1954) 1.
14. R H Ritchie and A Howie, Phil. Magz. 36 (1977) 463.
15. D Pines, Elementary excitations in solids, Benjamin Inc, New York, 1963.

16. R H Ritche, Nucl. Instr. And Meth. 198 (1982) 81.
17. A Akkerman et.al, Nucl. Instr and Meth B . 227 ( 2005) 319
18. Properties of GaAs , Ed by M R Brozel and G E Stillman, INSPEC, IEE , London (1996).
19. NIST Data base, <http://physics.nist.gov/PhysRefData/FFast/Text/cover.html>
20. D Emfietzoglou et.al, Nucl. Inst and Meth. B 212 (2003) 101.
21. S Heredia-Avalos et.al, Nucl. Inst and Meth. B 230 (2005) 118.
22. M Rajatora et.al, Nucl. Instr and Meth. B. 119 (1996) 457.
23. M Nigam et.al, Nucl. Instr and Meth. B. 219 (2004) 273.
24. P Sigmund and A Schinner, in Fundamental & Applied Aspects of Modern Physics, ed. by S H Connell & R Tegen World Sci., 178-187 (2001).
25. Stopping and Range of Ions in Matter (SRIM2003), <http://www.srim.org/>
26. Convolution approximation for swift Particles (CasP), <http://www.hmi.de/people/schiwietz/casp.html>



# CHAPTER VII

## Conclusions and outlook

### 7.1 Effects of SHI on GaN and AlGaN/GaN heterostructures

The effects of SHI have been studied on the bulk epitaxial GaN layers and AlGaN/GaN heterostructures. All the samples were irradiated with 150 MeV Ag ions with a fluence of  $5 \times 10^{12}$  ions/cm<sup>2</sup>. RBS/Channeling and HRXRD characterizations are used for the defects studies after irradiation. We have used the incident ion energy dependence studies along  $\langle 0001 \rangle$  and  $\langle 1213 \rangle$  axes. Our calculations show that the common type of dislocations (pure screw and edge threading dislocations) found in GaN would not affect the  $\langle 0001 \rangle$  axis. But the off normal axis  $\langle 1213 \rangle$  will be affected by all kinds of dislocations.

Un-irradiated GaN samples have been characterized by RBS/C, HRXRD and AFM. Energy dependence analysis has been carried out along  $\langle 0001 \rangle$  axis on all the samples (A4, A6, RE48 U ) and defects densities were calculated at a depth of about 100 nm from the surface. The calculated dislocation densities are high as expected in GaN samples, which is evident from the high  $\chi_{\min}$  values. Incident ion energy dependence shows  $E^{0.5}$  which corresponds to dislocations and the calculated dislocation densities are  $2.4 \times 10^8$ ,  $6.2 \times 10^{11}$  &  $4.6 \times 10^{10}$  cm<sup>-2</sup> for A4, A6 & RE48 respectively. AFM surface morphology shows that both screw and edge threading dislocations are present in the samples.

After irradiation, the dislocation densities increase to  $5.2 \times 10^9$  and  $6.1 \times 10^{11}$  on A4I and RE48I samples respectively. In the sample A6I, we did not observe any meaningful energy dependence. This may be due to the random scattering from the dislocation core. In the other irradiated samples A4I and RE48I, there is a large scatter of the data points in DP vs.  $E^{1/2}$  curve. This may be due to the point defects created by the swift heavy ions. AFM surface morphology shows clustering of dislocations at the surface, which is complemented by the increase in lateral correlation length in HRXRD results.

SHI's deposit enough energy for the material to reconstruct at the interface i.e. low temperature buffer layer/Sapphire interface. As a result of this, more strain is induced and



more dislocations are formed in the GaN layer. This increase in dislocation densities after irradiation has been confirmed by the HRXRD results, where strain was found to increase after irradiation. Damage creation in GaN by Swift Heavy Ions (SHI) is very complex process. The high energy deposited by the ion to the lattice, results in two kinds of damage creation in GaN. One is N loss and Ga rich regions, as confirmed by the Gaussian broadening of X-Ray peak widths and small shoulder peaks. Broadening of the optical band-edge absorption also confirms this. AlN cap layer can be used to reduce the N loss due to irradiation. The second damage is nucleation of dislocations due to the reconstruction of LT GaN buffer layer. Also the initial defect configurations in the pristine samples play a major role in the damage creation by swift heavy ion irradiation.

In AlGaIn/GaN heterostructures RBS/Channelling strain measurement shows that unirradiated sample has a small residual tensile strain which increases after irradiation. One would expect that when strain increases defect density should decrease. But here, the defect density in AlGaIn and GaN layers increases after irradiation. AFM surface morphology shows that there is a clustering of defects at the surface due to irradiation. This complements the increase in lateral correlation length from HRXRD measurements. The difference in the calculated defect density by RBS/Channelling and HRXRD was attributed to the fact that HRXRD gives depth averaged information, whereas RBS/C yields depth resolved information.

The high energies deposited by SHI's is normally given to the electronic system of the target materials. These electrons transfer this energy to the lattice system by electron phonon coupling. The energy transferred depends on the material properties. There are two competing processes which decide the material modification. First one is the deposited high energy in small diameter causing the materials to melt *at very small time scale* i.e. in order of pico seconds. Second process is the dynamic self annealing of materials initiated by its bond strength which tries to crystalize the material at the same time. These two processes compete with each other depending on the material properties. In III-Nitrides the process of dynamic annealing is very strong because of its high bond strength. Al-N bond is stronger than Ga-N, so Al-N recombines faster and complete epitaxial reconstruction of AlGaIn layer has been observed. Similarly epitaxial reconstruction has been observed in GaN layers as well which causes the reconstruction of 3D grown GaN buffer layer (existing in the form of islands). This results in release of

the strain to the extent of about ~16 % between GaN/Sapphire. The same has been reported by S. O. Kucheyev et.al, [34] where they observed *peeling off* from the bulk epitaxial GaN layer upon 200 MeV Au ions at fluence of  $1 \times 10^{13}$  ions/cm<sup>2</sup>. In our samples the lower  $S_e$  and lower fluence prevented the peeling of the layer due to irradiation. Consequently, we observed more threading dislocations in both the layers. Swift heavy ion induces additional strain in AlGaIn and GaN layers by the process of dynamic annealing. At the same time, as a result of GaN buffer layer getting reconstructed, more threading dislocations are induced and travel to the surface.

Generally one would expect that ion beams generate defects and common question is that, why to subject GaN to ion beam irradiation, as it is already highly defected? One could avoid the defects creation due to the ion beam by using very thick (~100  $\mu$ m) GaN layers (like HVPE grown GaN templates for AlGaIn layer) and then subjecting these to ion irradiation will result in improving the AlGaIn layer and their interface quality without increasing the dislocation density (which is of importance) . In this situation these ions will not reach the GaN/Sapphire interface, as their range is normally ~ 11 to 13  $\mu$ ms.

## 7.2 Optical properties and Lattice site location of Er implanted GaN

Set of samples cut from same wafer of GaN film on Al<sub>2</sub>O<sub>3</sub> substrate has been implanted with 190 keV Er<sup>3+</sup> ions, followed by post-implantation annealing. Optical absorption (OA) measurements, PL , Time-resolved PL analysis, PL excitation (PLE) measurements and RBS/Channelling have been performed to characterise these samples. No luminescence related to the presence of the rare earth was detected in the as-implanted samples. On the other hand, all the series exhibit a darkened surface, going from dark yellow for *ErGaN1 as-implanted* to a plain metallic colour for *ErGaN10 as-implanted*. This might be due to Ga segregation effect induced by the Er ion implantation. The effects are more on the system with the higher implantation dose of Er, as evidenced by the colour of the sample surface. After annealing, all the samples show activation of Er NIR luminescence. The peak shapes show the typical  $^4I_{13/2} \rightarrow ^4I_{15/2}$  transitions with stark structures. *ErGaN1\_1100°C* and *ErGaN10\_800°C* samples, which are doped with different Er amounts and annealed at different temperatures, have very close excitation cross section ( $\sigma_{eff}$ ). This shows that the excitation cross section is an intrinsic parameter of

the ErGaN system and having weak dependence on the synthesis conditions. The figure of merit depends only on temperature dependence of fraction of Er activated atoms ( $f_{act}$ ), rather than on the effective excitation cross section. Also, we observed that the PL emission in the NIR can be continuously stimulated in the whole excitation range, even by pumping at wavelengths where the Er ions are typically transparent. This clearly indicates that there is an indirect excitation path linked to the interaction with the GaN matrix.

ErGaN10 series shows smaller figure-of-merit values than ErGaN5, which may be due to a higher Er doping level resulting in concentration quenching effects. The percentage of the Er atoms displaced from the symmetrical site is also high for the ErGaN10 series. As the concentration increases, more Er atoms are moving towards the interstitial site and where Er-Er cross relaxation are favourable. Increase in annealing temperature drives higher level of Er to interstitial sites, which results in reduction in the overall figure of merit parameter. The enhanced Er diffusivity at the high temperatures results in the reduction of activation in both the series. The effect of concentration is to increase the percentage of Er atoms going to the low symmetry sites from substitutional sites.

On the other hand *ErGaN1* is having completely different behaviour. The figure of merit increases with increase in the temperature. This may be due to the low Er doping level, where concentration quenching effects can be limited. Also the less GaN damages drive the Er atoms in the perfect symmetrical sites. So, as the temperature is raised, it is possible that the progressive matrix recovery makes it easier for an Er ion to adjust in a local structural site favourable for its optical activation, resulting in an optimization of the  $f_{act}$  parameter.

### 7.3 Stopping power of GaAs

We have presented results for the SP of GaAs for protons, light and heavy ions. These are technologically important materials and are used in high frequency devices and light emitting diodes. So the precise calculations of SP of these materials are important. In the present calculations we used the Dielectric Function Theory (DFT) within the framework of first Born approximation. Here we used the Riche-Howie [14] formalism of the DFT theory of stopping power. We have also used extended Drude type function to model the

ELF of GaAs. Optical data were used for valence shell contributions and X-Ray photo absorption data were used for inner shell contributions. We have used the quadratic dispersion scheme to extend the ELF into momentum space. Sum rule also gives the satisfactory values; with f-sum rule value as 0.9899 which is close to unity. The perfect screening sum rule yields the value of 0.9337. Calculated  $I$  value is 379 eV which is close to 385 eV, Bragg value for GaAs. Our calculations fit reasonably well for wide range of projectiles from protons to heavy ions like gold. It has been realized that, one needs to include the higher order correction for energies near Bragg peak maximum. We did not include the charge exchange effects,  $Z_1^3$  Barkas effect and Bloch corrections. These higher order corrections play role near the Bragg peak and charge exchange effects dominate at low velocity region. Since these effects could not be included in the standard DFT model, our results deviate from the experimental values in the low energy regions and around Bragg peak maximum. Our calculations fit well at high energy regions of proton. Thus, one can use the extended Drude model and quadratic dispersion scheme with higher order corrections to model the compound semiconductors to calculate the stopping powers with reasonable accuracy. As the optical data becomes available for GaN based materials, one can perform similar calculations for these materials also.

#### **7.4 Future prospects**

This thesis presents some results of our initial efforts on the ion beam modification and analysis of GaN based semiconductors. The present study throws light on the understanding of ion induced modification studies of GaN bulk epitaxial layers and AlGaIn/GaN heterostructures. It also highlights the use of RBS/Channeling technique to confirm the observed results. Also the preliminary stopping power calculations of GaAs have been performed. In this direction several issues need further experimental and theoretical work. Some of these are;

- It will be interesting to study the modifications of the very thick GaN layers like HVPE grown or free standing GaN samples (available these days). In these layers we would expect that these ions will not see the GaN/Sapphire interface.

- Also it will be interesting to study the effects of SHI on the AlGa<sub>N</sub>, InGa<sub>N</sub> multilayers grown on such above said substrates. Where one can expect the heterostructures to become fully strained after irradiation.
- Er implantation resulted in damaging of Ga<sub>N</sub> layers, one can use high dose 2 MeV He ions to recover the damaged Ga<sub>N</sub> matrix to improve the Er luminescence. It will be interesting to compare and investigate the difference between the thermal and ion beam annealing.
- Generally, SHI like Gold ions generates ion tracks in Ga<sub>N</sub>s. To incorporate more Rare Earth (RE) or Transient Metal (TM) into Ga<sub>N</sub> site, one can etch these tracks to form nano pipes and incorporate more atomic prevent RE into Ga<sub>N</sub> for better activation and luminescence.
- It will be interesting to study the stopping power of InGaAs and AlGaAs materials by including the higher order corrections, and use these values for Monte Carlo ion track simulations program to understand the observed strain modifications and defect density reduction by ion irradiation.
- At present there are no good optical data for high energy regions available for III-Nitrides. It will be interesting to calculate the stopping powers of III-Nitrides as and when we have such data. Also one can use the available theoretical dielectric function of these materials for calculating SP of Ga<sub>N</sub>s.

# N SATHISH

---

**Contact address:**

Research Scholar,  
School of Physics,  
University of Hyderabad,  
Hyderabad, 500046,  
AP, India

Tel: +91-40-23134385

Fax: +91-40-23010227

Mobile: +91-9949893797 (preferred)

Email: [ph03ph11@uohyd.ernet.in](mailto:ph03ph11@uohyd.ernet.in)

Nationality: Indian

Marital status: Single

**Permanent address:**

41, 6<sup>th</sup> Cross street,  
Gnanaprakasam Nagar,  
Govt. Automobile Workshop Backside,  
Lawspet, 605008,  
Puducherry, India

Tel: +91-413-2243323

Email: [rnsathish@yahoo.com](mailto:rnsathish@yahoo.com) (preferred)

Date of birth: 26<sup>th</sup> April 1977

Place & country of birth: Villupuram, TN

---

**"Seeking career opportunity with an organization of repute in the academic and research for better future prospects"**

## Academics

PhD in Physics, School of Physics, University of Hyderabad, (submitted on June 2009)

M.Phil in Physics, Dept of Physics, Pondicherry University (Dec 2002) (I class)

M.Sc in Physics, Dept of Physics, Pondicherry University (April 2001) (I class)

B.Sc in Physics, University of Madras (April 1998) (I class)

## Fellowships and Position Held:

- ❖ JRF in DRDO, sponsored project titled *"Swift Heavy ion studies semiconductors heterostructures using channelling blocking ERDA"* during 24<sup>th</sup> Aug 2003 - 24<sup>th</sup> Feb 2005
- ❖ JRF in SSPL, New Delhi, sponsored project titled *"Ion Beam modification and Analysis of III-V semiconductor Heterostructures and Multi Quantum Wells"* during 1<sup>st</sup> Feb 2006 - 31<sup>st</sup> Jan 2008
- ❖ SRF in SSPL, New Delhi, sponsored project titled *"Ion Beam modification and Analysis of III-V semiconductor Heterostructures and Multi Quantum Wells"* during 1<sup>st</sup> Feb 2008 - 31<sup>st</sup> Jan 2009
- ❖ UGC Meritorious student fellowship from 7<sup>th</sup> March 2009 to till date.



### **Advanced courses undergone:**

Attended PhD Teaching Program at NSC, New Delhi (From Feb '04 to March '04 and Oct to Dec '04):

- ❖ Accelerators. Detectors and Transducers. Cryogenics Measurement techniques
- ❖ Ion Beams in Materials Science
- ❖ Ion Beams in Semiconductors and Semiconductor Devices

### **Skills and visits**

- ❖ Experimental techniques
  - ❖ Accelerator based characterizations (RBS, Channeling, ERDA)
  - ❖ High resolution XRD
  - ❖ Photoluminescence
  - ❖ Atomic Force Microscopy and sample preparation for XTEM
- ❖ Condensed Matter Physics (Solid State Physics and Material Science)
  - ❖ Material modification using ion beams
  - ❖ GaN and related materials
  - ❖ Ion solid interaction – Dielectric function theory of stopping powers
- ❖ Computational Physics
  - ❖ Monte Carlo and Molecular Dynamics
  - ❖ Monte Carlo analysis of RBS/C spectra
  - ❖ Using Monet Carlo for ion solid interaction

### **Visits**

Visited Dept of Physics, University of Padova, Padova, Italy – during 25<sup>th</sup> March to 8<sup>th</sup> April 2006

### **Teaching Experience:**

Have done Teaching Assistance Ship (TA) for M.Tech (Computational Techniques) course Numerical methods during July – December 2008.

### **Computer Knowledge**

**Languages:** C, C++ and Visual Basic.

**Mathematical Packages:** MatLab, Mathematica

**Parallel programming:** having knowledge on MPI Open MP and P-Threads.

**Operating systems:** Windows platform and linux.

**Course:** Advanced diploma in client server technology (one year course)

Which cover C , C++ with OOPS, unix, Visual Basics, Power Builder for front end programming and Oracle with SQL for backend.

Having small knowledge on system programming using C



## RESEARCH PROJECTS

(i) M.Sc Project : Synthesis and Characterization of BaTiO<sub>3</sub> and Ba<sub>0.9</sub>Sr<sub>0.1</sub>TiO<sub>3</sub> using XRD and DSC.

(ii) M.Phil Project : Study of Ag<sub>2</sub>O-MoO<sub>3</sub> glass structure by Molecular Dynamics simulations.

(iii) Worked as JRF the DRDO sponsored project titled "Swift Heavy ion studies semiconductors heterostructures using channelling blocking ERDA" From 24<sup>th</sup> Aug 2003 to 24<sup>th</sup> Feb 2005

(iv) Worked as SRF and JRF in SSPL, New Delhi, sponsored project titled "Ion Beam modification and Analysis of III-V semiconductor Heterostructures and Multi Quantum Wells" from 1st Feb 2006 to 31st Jan 2008

(v) Ph.D thesis titled "Ion beam modification of GaN based Semiconductor Heterostructures" submitted in June 2009.

## Research Work

The main objective of my research work has been towards the understanding of the interaction of energetic ions with semiconductor materials. The modification of materials due to swift heavy ion (SHI) irradiation has been investigated. Materials studied are GaN semiconductor substrates, AlGa<sub>N</sub>/GaN heterostructures and Er implanted GaNs. High resolution XRD (HRXRD), RBS/Channeling (RBS/C), Atomic Force Microscopy (AFM) and Photo Luminescence (PL) have been used to characterize the samples. The energy loss rates of these energetic particles in these third generation materials plays crucial role in precisely controlling the modification and predicting the radiation damage. Therefore I have carried out calculations of stopping power of GaAs using dielectric function theory and optical data model.

Presently I am working on the preparation of III Nitrides nano-structures by RF sputtering on patterned substrates. In specific, preparation of crystalline Al<sub>x</sub>In<sub>1-x</sub>N where one can tailor the band gap from 0.7 eV to 6.1 eV. Such nano-structures are of interest from the optical applications in future devices. I am also working on Monte Carlo analysis of RBS dechannelling analysis, where I am implementing the dislocations into the existing code McChasy. Also I am working on the stopping power calculations of III-Nitrides using the dielectric function theory and optical data model.

## Training School / Conference / Workshop

- ❖ Participated in workshop on "Material characterization and surface modification in research and industry using Ion Accelerators" held at National Centre for Compositional characterization of Materials, BARC,

Hyderabad. (9<sup>th</sup> to 11<sup>th</sup> Feb, 2005).

- ❖ Participated in “Indo-German Workshop on Synthesis and Modification of Nano-sized Materials Using Energetic Ion Beams” at Nuclear Science Centre, New Delhi, India (20 – 24, Feb 2005).
- ❖ Participated in workshop on “Practical Aspects of Parallel Computing on IBM P690 Cluster” at Centre for Modeling, simulation and Design (CMSD), University of Hyderabad. (21<sup>st</sup> to 24<sup>th</sup> September 2004).
- ❖ Attended School on “Ion Beam Analysis and Accelerator Applications” from 13<sup>th</sup> – 24<sup>th</sup> March 2006 at ICTP, Italy.
- ❖ Participated in international conference on “Ion Beam Analysis 2007”, held in Hyderabad. India, during 23<sup>rd</sup> -28<sup>th</sup> September 2007.
- ❖ Participated in DAE-BRNS Seminar-cum-Workshop on “Material characterization and surface modification in research and industry using ion accelerators”, during 31<sup>st</sup> March – 4<sup>th</sup> April 2008.

### Research Publications

#### Journals:

1. HRXRD, AFM and optical study of damages created by swift heavy ion irradiation in epitaxial GaN, **N Sathish**, S Dhamodaran, A P Pathak, S A Khan, M Ghanashyam Krishna, S A Khan, D K Avasthi, A Pandey, R Muralidharan, G Li and C Jagadish, Nucl. Instr. and Meth. B 256 281 (2007).
2. RBS/Channeling and HRXRD studies on swift heavy ion irradiated AlGaIn/GaN heterostructures, **N Sathish**, S Dhamodaran, A P Pathak, B Sundaravel, K G M Nair, S A Khan and D K Avasthi, M. Bazzan E. Trave, P. Mazzoldi, D. Scott Katzer, ( In preparation)
3. Raman and AFM studies of swift heavy ion irradiated InGaAs/GaAs heterostructures, S Dhamodaran, **N Sathish**, A P Pathak, S A Khan, D K Avasthi, T Srinivasan, R Muralidharan, R Kesavamoorthy and D Emfietzoglou, *J. Phys: Cond. Mat.* 18, 4135 (2006).
4. RBS/Channeling studies of swift heavy ion irradiated InGaAs/GaAs heterostructures, S Dhamodaran, **N Sathish**, A P Pathak, S A Khan, D K Avasthi, T Srinivasan, R Muralidharan, B Sundaravel, K G M Nair, *Nucl. Instr. Meth. B* 244, 174 (2006).
5. Swift heavy ion modification of semiconductor heterostructures, A P Pathak, S Dhamodaran, **N Sathish** and N Srinivasa Rao, *Radiation Effects and Defects in Solids* 162, 131 (2007).
6. Ion beam analysis of defects and strain in heavy ion irradiated InGaAs/GaAs heterostructures, S Dhamodaran, **N Sathish**, A P Pathak, D K Avasthi, R Muralidharan, B Sundaravel, K G M Nair, D V Sridhara Rao, K Muraleedharan and D Emfietzoglou, *Nucl. Instr. Meth. B* 254, 283 (2006).
7. Ion beam irradiation and characterization of GaAs based heterostructures, S Dhamodaran **N Sathish**, A P Pathak, S V S N Rao, A M Siddiqui, S A Khan, D K Avasthi, T Srinivasan, R Muralidharan, C Muntele, D Ila and D Emfietzoglou, *Nucl. Instr. Meth. B* 242, 538 (2006).
8. High resolution XRD analysis of swift heavy ion irradiated InGaAs/GaAs heterostructures, S Dhamodaran, **N Sathish**, A P Pathak, S A Khan, D K Avasthi, T Srinivasan, R Muralidharan and B M Arora, *Nucl. Instr. Meth. B* 256 260 (2007).
9. Dechanneling of electrons by stacking faults – a model quantum mechanical calculations, S Dhamodaran, **N Sathish**, A P Pathak, L N S Prakash Goteti, S V S Nageswara Rao, V Raghav Rao and D Emfietzoglou, *Nucl. Instr. Meth. B* 230, 100 (2005).

10. A study of electronic stopping of protons in soft biological matter, D Emfietzoglou, A P Pathak, G Papamichael, K Kostarelos, S Dhamodaran, **N Sathish** and M Moscovitch, *Nucl Instr. Meth. B* 242, 55 (2006).
11. Study of GaAs and GaN based heterostructure surfaces and interfaces using ion beams and other complementary techniques, A.P. Pathak, **N. Sathish**, S. Dhamodaran, D. Emfietzoglou. *Vacuum* ( Inpress)

#### Conferences/Workshop:

1. Channeling techniques to study strains and defects in heterostructures and multi quantum wells, A P Pathak, S Dhamodaran and **N Sathish**, International Workshop on Channeling (Channeling 2004) Proceedings in SPIE 5974 (2005) 136.
2. Ion beam modifications and characterization of semiconductor heterostructures, A M Siddiqui, S Dhamodaran, S V S N Rao, **N Sathish** and A P Pathak, Invited Talk for and Presented by APP in ASTRA-2004, Proceedings page: 633-641 Edited by T.S. Sudharshan, G. Sundararajan, G. Totten and S.V. Joshi.
3. Ambiguity of mixing at the InGaP/GaAs interface, S Dhamodaran, **N Sathish**, A P Pathak, S A Khan, D K Avasthi and B Sundaravel, DAE-Solid State Physics Symposium, 2006 page-435.
4. Analysis of defects in heterostructures by RBS/Channeling, S Dhamodaran, **N Sathish**, N Srinivasa Rao, A P Pathak, R Muralidharan, B Sundaravel and K G M Nair, DAE-Solid State Physics Symposium, 2006 page-777.
5. HRXRD Characterization of MOCVD grown GaN layer on AlN/GaN heterostructures, M. Wójcik, J. Gaca, A. Turos, A P Pathah and **N.Sathish**.

#### REFERENCES

- |   |   |
|---|---|
| <p>1. Prof. A. P. Pathak,<br/>School of Physics,<br/>Centre,<br/>University of Hyderabad,<br/>Central University P.O.<br/>Hyderabad – 500 046.<br/>e-mail : appsp@uohyd.ernet.in<br/>anandp5@yahoo.com<br/>Phone : +91-40-23010181 / 23134316<br/>236</p> | <p>2. Dr. D. K. Avasthi,<br/>Nuclear Science<br/><br/>P.O Box 10502,<br/>Aruna Asaf Ali Marg,<br/>New Delhi – 110 067.<br/>e-mail : dka@iuac.ernet.in<br/>dka4444@gmail.com<br/>Phone: +91-11-26893955 Extn</p> |
| <p>3. Dr. K. G. M. Nair,<br/>Particle Irradiation Facility,<br/>Materials Science Division,<br/>Indira Gandhi Centre for Atomic Research,<br/>Kalpakkam – 603 102.<br/>e-mail : kgmn@igcar.gov.in<br/>Phone : +91-44-27480085</p>                         |   |